

Microgels at interfaces: from single-particle modeling to collective behavior



Fabrizio Camerin

Department of Basic and Applied Sciences for Engineering

PhD Course in Mathematical Models for
Engineering, Electromagnetics and Nanosciences
Curriculum in Materials Science

Sapienza University of Rome

This dissertation is submitted for the degree of
Doctor of Philosophy

Supervisor:
Dr. Emanuela Zaccarelli

XXXIII cycle
November 2020

To anyone who still believes in wisdom.

Declaration

I hereby declare that except where specific reference is made to the work of others, the contents of this dissertation are original and have not been submitted in whole or in part for consideration for any other degree or qualification in this, or any other University. This dissertation contains my own work and that done in collaboration with others, as specified in the text, or as cited in the Bibliography.

Fabrizio Camerin
XXXIII cycle
November 2020

Acknowledgements

My heartfelt thanks go to Emanuela. I believe it is not easy to meet a competent person, who knows how to convey passion for what she does, who is enthusiastic about discovering and understanding new things - whatever their significance - and who is capable to persevere in front of disappointing results. I have learned a great deal from you doing science in these years and I will always be grateful. So will I to every member of the group, to those who have always supported me and to those who have helped me more closely, each in their own way. I embrace you all, you have been like family to me. José, Giovanni, we know what it means to be loyal friends and colleagues to whom you can ask anything without expecting anything in return or feeling indebted. We also know what it means to take it seriously or lightly at the right time. Thank you, I will always treasure all your advice.

I would like to thank Lucio for giving me the opportunity to spend some time doing research in Zurich. It was exciting to meet the people who worked on the experimental side of the topics discussed in this Thesis, Miguel and Jacopo in particular, whom I sincerely thank. In Ljubljana instead I had the opportunity to meet Primož who besides being a good researcher is a great person. It has been a pleasure to collaborate with all of you.

A special thanks to my parents and all my friends, the closest and the farthest, who are the most precious thing I have. It is always heartening to feel that you can count on these people and you can confide in them. Thank you for sharing with me experiences, travels, stories, discussions. Finally, a thought to all the people I met in hospitals through clown-therapy volunteering. You too have taught me a lot.

Grazie a tutti.

Abstract

Colloids are micro- or nano-sized particles that are increasingly used as model system to address fundamental issues in soft matter science. Microgels in particular are characterized by a crosslinked polymer network which provides them with internal elasticity and deformability. Their colloid-polymer duality clearly emerges when such particles are adsorbed at fluid-fluid interfaces, where microgels retain a so-called fried-egg shape. Despite the great theoretical and applicative interest for this system, there are several aspects that still need to be explored and, among all, the connection between the properties and conformation of a single particle and their collective behavior. In this Thesis, we aim to shed light on this aspect complementing molecular dynamics simulations and experiments. We will move from the single-particle microgel modeling in explicit solvent in the bulk, building on a coarse-grained model for microgels which grants a realistic description of the internal polymeric architecture and swelling behavior. Once this is established, we transfer this knowledge to correctly mimic the effect of the surface tension, in order to reproduce the correct extended conformation of the particle at the interface. Furthermore, by computing their effective interaction potential, we demonstrate that microgels adsorbed at an interface behave like 2D elastic particles, following the two-dimensional Hertzian theory. The analysis of the dynamical properties evidences the presence of multiple reentrant dynamics phenomena where, by continuously increasing the particle density, microgels first arrest and then refluidify due to the high penetrability of their extended coronas. In particular, we prove that this behavior can be found for small and loosely crosslinked microgels in a range of experimentally accessible conditions. A final section is dedicated to the analysis of hollow microgels that, given their topology, adopt a single particle conformation at the interface which is radically different from that of standard microgels.

Table of contents

List of figures	xiii
List of tables	xvi
Introduction	1
1 <i>In silico</i> microgel modeling	23
1.1 Numerical design of coarse-grained microgels	23
1.2 A realistic model for microgel particles	27
1.3 Tuning the crosslinker concentration in the polymer network	32
1.3.1 The choice of the designing force	33
1.3.2 Size effects	36
1.3.3 Comparison with the experiments for different tempera- tures across the Volume Phase Transition	40
1.4 Summary	46
2 Modeling microgels in an explicit solvent	49
2.1 Different models of explicit solvent	50
2.2 Swelling behavior	52
2.3 Structural features in an explicit solvent	56
2.3.1 Results for a loose microgel configuration	56
2.3.2 Results for a more confined microgel	60
2.4 Collapse kinetics	62
2.5 Discussion	64
3 Conformation of a microgel at a liquid-liquid interface	68
3.1 The control on the surface tension	70
3.1.1 The Flory-Huggins interaction parameter χ	70
3.1.2 Mapping onto DPD	73
3.2 Modeling the microgel-solvent interactions	75
3.3 Characterization of the microgel at the liquid-liquid interface	78

3.3.1 Numerical/experimental comparison	81
3.4 Effects of a different surface tension	87
3.5 Summary	89
4 Microgels at interfaces as effective 2D elastic particles	92
4.1 Effective interaction potential	95
4.2 Elasticity theory calculations	102
4.2.1 Assessment of the elastic moduli	102
4.2.2 Interfacial and bulk elastic moduli	105
4.3 Multi-particle dynamical response	108
4.4 Summary	116
5 Hollow microgels	119
5.1 Characterization in bulk	122
5.1.1 Dependence of the shell thickness	122
5.1.2 Temperature effects	129
5.2 Conformation at the interface	132
Conclusions and Perspectives	136
A brief description of parallel work on charged microgels	142
List of publications	148
References	151

List of figures

1	Hard sphere phase diagram	3
2	Soft and hard colloids	4
3	Premelting of a colloidal crystal in bulk	6
4	Microgel phase diagram in bulk	8
5	Microgels at a flat water/oil interface	13
6	Isostructural transition	16
7	Patterns occurring with a two step deposition	17
1.1	General coarse graining procedure	24
1.2	Diamond-lattice-based microgel	26
1.3	Compact or fluffier microgels	31
1.4	Swelling ratio as a function of Z	32
1.5	Forces acting on the crosslinkers and density profiles	33
1.6	Microgel form factors as a function of the size	36
1.7	Density profiles as a function of the size	38
1.8	Simulation snapshots as a function of the microgel size	39
1.9	Form factors as a function of the temperature for big microgels	41
1.10	Mapping between temperature and α	42
1.11	Form factors as a function of the temperature for smaller microgels	42
1.12	Comparison of the standard and extended fuzzy sphere models	44
1.13	Experimental and numerical microgel density profiles as a function of the temperature	45
2.1	Microgel swelling curves	53
2.2	Effect of microgel topology and solvent arrangement	55
2.3	Density profiles for a loose microgel configuration across the VPT	57
2.4	Microgel form factors for a loose microgel across the VPT	58
2.5	Solvent density profiles for a loose microgel configuration across the VPT	59
2.6	Microgel density profiles, solvent density profiles and form factors for a compact microgel across the VPT	60
2.7	Collapse kinetics	62

3.1	Choice of the monomer-solvent interaction parameters	76
3.2	A microgel at a liquid-liquid interface	77
3.3	Density profiles of the microgels at the interface	78
3.4	Diamond based microgel network	80
3.5	AFM height profile	80
3.6	Conformation of microgels at the interface in experiments and simulations by varying c	82
3.7	Comparison simulations/experiments	84
3.8	A large microgel at a liquid-liquid interface	86
3.9	Density profiles of larger microgels	86
3.10	Comparison between a microgel at water/benzene and water/hexane interfaces	88
4.1	Effective interaction in bulk	93
4.2	Multi-Hertzian model	94
4.3	Microgels interacting at the interface	96
4.4	Effective potentials for microgels at the liquid-liquid interface and related 2D Hertzian fit parameters.	97
4.5	Microgels interacting at the interface	98
4.6	Comparison of other fits to the effective potentials	99
4.7	Potential of mean force $W(J)$ and $W(I)$ for a microgel at the interface and in bulk for $c = 10\%$	104
4.8	Elastic moduli at the interface and in the bulk.	106
4.9	Radial distribution function	109
4.10	Multi-particle simulations snapshots	110
4.11	Reentrant behavior	111
4.12	2D Hertzian phase diagram	112
4.13	Dependence of the 2D Hertzian strength A on the crosslinker concentra- tion for microgels of various sizes	114
4.14	Young modulus for different crosslinker concentrations and microgel sizes	115
5.1	Form factors comparison for the thin-shell hollow microgel	123
5.2	Form factors comparison for the thin-shell hollow microgel	124
5.3	Effect of the designing force on crosslinkers for the thin-shell hollow microgel	124
5.4	Form factors of regular and thin-shell hollow microgels	125
5.5	Simulation snapshots for the thin-shell hollow microgel	125
5.6	Effect of the designing force on crosslinkers for the thick-shell hollow microgel	126
5.7	Form factors comparison for the thick-shell hollow microgel	127

5.8	Form factors of thick-shell hollow microgels	128
5.9	Simulation snapshots for the thick-shell hollow microgel	128
5.10	Form factors as a function of effective temperature	129
5.11	Density profiles of hollow microgels as a function of effective temperature	130
5.12	Temperature effects on the form factors	131
5.13	Swelling curves	131
5.14	Density profiles at the interface	132
5.15	Simulation snapshots for hollow microgels at the interface	133
C.1	Swelling curves of charged microgels	143
C.2	Simulation snapshots	144
C.3	Form factors	145

List of tables

3.1	Experimental characterization in bulk and comparison between AFM and FreSCa	83
3.2	Comparison simulations and experiments	84
3.3	Experimental results at the water/benzene interface	88
4.1	Gaussian fit	99
4.2	Comparison of 3D Hertzian fit parameters to theoretical values	100

Introduction

The present Thesis focuses on the numerical modeling of soft microgel colloids and aims to establish a link between single particle properties and their collective behavior, especially when adsorbed at fluid-fluid interfaces.

One of the main goals of soft matter science is to take advantage of the microscopic complexity of single building blocks to design the macroscopic properties of emerging materials with ubiquitous relevance in everyday life. The focus is on a wide range of materials that could be easily deformed by imposing an external stress. Furthermore, their physical behavior occurs mostly at a low energy scale, comparable to that of the thermal motion [1–3]. Colloids, polymers or emulsions are among the most widely investigated objects in the soft matter world to which many biological systems such as proteins or antibodies also belong [1, 4, 5].

Colloidal dispersions, in particular, are characterized by the presence of insoluble micro- or nano-sized particles in a continuous medium and can be viewed as the mesoscale counterpart of solvated atoms and molecules in the microscopic world [6]. The advantages of dealing with colloids are manifold, reason for which large investigations of their phase behavior have been carried out in several studies in condensed matter physics [7, 8]. This has been made possible thanks to the fact that colloids, for their high mass, have time- and length-scales that are order of magnitude higher than the atomic counterparts. In this way, experiments are much more accessible and visible light is already a relevant probing tool [9].

An important aspect of colloidal systems is the possibility to design different building blocks as opposed to atomic and molecular counterparts where they are

well-defined by the inherent chemical interactions. In fact, mesoscopic assemblies of colloids and nanoparticles display features that depend critically on the microscopic details of the constituent units, *e.g.* composition, size and shape, as well as on the specific macroscopic physical conditions such as the thermodynamic control parameters. It is by carefully choosing and tuning all these variables that one can induce the formation of different structures and explore various states, such as liquid-like fluids, glasses or crystals [10]. At the core of this collective behavior is the effective interparticle interaction, which ultimately dictates the static phase behavior and, eventually, the dynamics of the assembly. Such interaction corresponds to an "effective" description and can be regarded, theoretically, as a way to simplify the approach to such complex dispersions. Direct steric interactions between the particles, but also the role of the solvent, the presence of charges and all other ingredients that typically play the role of a background in a colloidal dispersion, are conveyed to a so-called **coarse-grained** representation. In this way, it is easier to achieve information at the multi-particle level and thus to determine the properties of a colloidal ensemble [11, 12].

In case a system is made of rigid (spherical) building blocks it can be approximately mapped to a hard-sphere system and its behavior can be investigated in a coarse-grained fashion through the so-called packing models [13]. The hard sphere can be viewed as the archetype example of colloidal systems, where interactions among different units only occur via excluded volume interactions and overlap is never allowed at any time. In other words, the interaction potential goes to infinity at a distance equal to the diameter of the particle. Noteworthy, is the possibility to retrieve a complete phase diagram whose only state variable, for the athermal nature of hard particles, is the volume fraction ϕ , as schematically drawn in Fig. 1. Each of the hard spheres states is characterized by a very precise value of ϕ , which has been determined both in theory [14, 15] and in pioneering experiments a few decades ago [16, 17]. By increasing ϕ , the system goes from a disordered liquid to a crystal phase, passing through a regime in which the two are in equilibrium. Above $\phi = 0.58$, the system lies in the amorphous glass state, signaled by an increase of the viscosity by several order of magnitudes, and in the so-called jammed state where particles are forced into contact [4]. At $\phi = 0.74$,

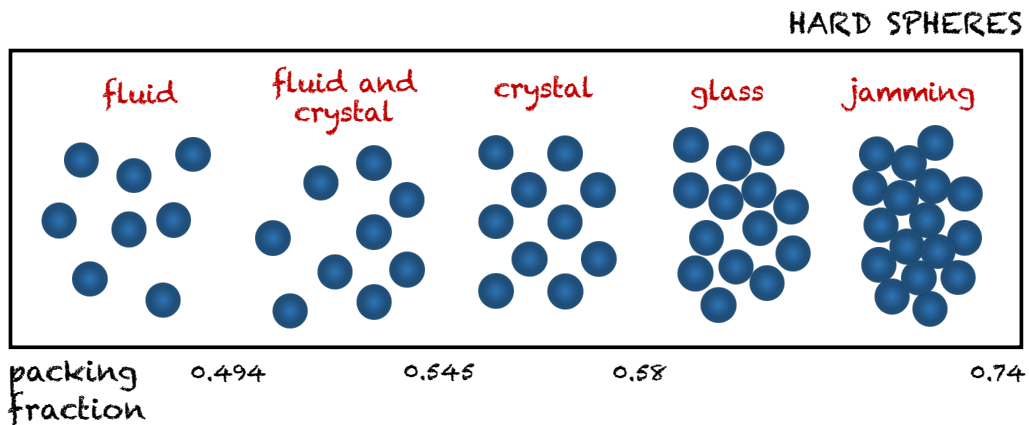


Figure 1: Hard sphere phase diagram. Schematic phase diagram of a hard sphere system by varying the packing fraction ϕ .

hard spheres are found in hexagonal close packing which represent the densest possible packing in three dimensions.

Despite (and thanks to) the disarming simplicity of the model, hard spheres have been used for a long time to successfully answer fundamental questions in several fields, whenever simple constituent units are involved [13]. Besides their usefulness in physics in the study of glass transition and their use to understand the nature of the jammed state [18–21], packing models have been even employed in biology to study the cell behavior to form tissues and molecular crowding within cells [22–24].

The hard sphere model system is complemented by a whole series of other colloids that are characterized by real deformability and elasticity, as displayed in Fig. 2. The softness of the particle is linked to the steepness of the interaction potential which is characterized by a wide ranging and smoother potential at contact with respect to the hard-sphere counterpart [25]. Correspondingly, the magnitude of the interaction energy goes from being of the order of thermal energy (expressed in $k_B T$, with k_B the Boltzmann constant and T the temperature) for ultrasoft polymer chains, to tens and hundreds of times the thermal energy for star polymers and microgels, up to the hard spheres where the potential at contact goes to infinity. The case of star polymers perfectly exemplifies a fundamental feature of soft interactions whereby, acting on the complexity and structural peculiarities of the system, it is possible to obtain a variety of different potentials

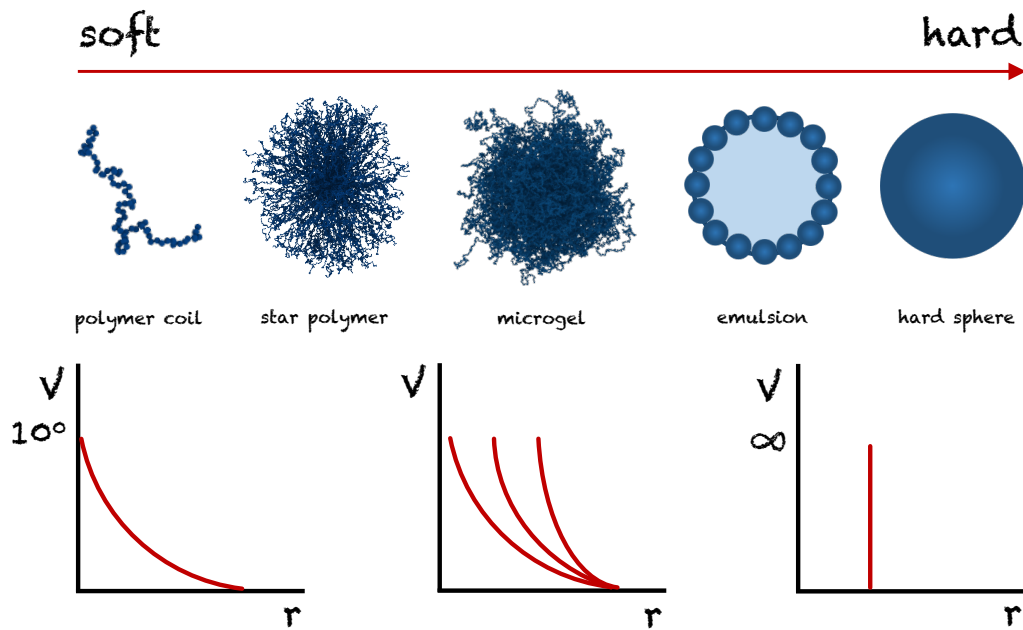


Figure 2: Soft and hard colloids. Re-drawn from Ref. [25]. The cartoons report, from left to right, a polymer coil, a star polymer, a microgel, an emulsion and a hard sphere. It is also schematically shown how the steepness of the interaction potential varies by acting on the softness of the colloid. In particular, the order of magnitude of the effective potential increases from $\approx k_B T$ to infinity, moving from the polymer chains, which are the most deformable objects, to the impenetrable hard spheres.

and thus explore different degrees of softness [25, 26]. Star polymers, in fact, are characterized by a long-ranged repulsion at large distances and a logarithmic repulsion at short separations, which depends on the microscopic interactions when multiple arms come in contact and interpenetrate. Thus, length and number of the arms represent a way to finely control the interaction between these colloids.

Among the available library of soft particles, microgels also represent an intriguing choice. **Microgels are colloidal-sized crosslinked polymer networks** which retain, in a microscopic fashion, the same features of a chemical gel where all its monomers are covalently linked to each other [27–33]. Their structure is determined by the chemical synthesis conditions that, in the common procedure of precipitation polymerization [34, 35] leads to the formation of spherical particles made of a compact core and a fluffy external corona decorated with multiple loops and dangling chains [36]. The precipitation polymerization technique involves

the formation of an initial homogeneous phase in which monomers, initiator and crosslinkers are mixed; subsequently, as the polymer is insoluble, it precipitates as it forms. The core-corona structure is generated by the fact that crosslinkers react faster than monomers [37, 38]. Unless microgels are synthesized with copolymerization methods that would allow to explicitly include charged moieties in the polymer, this type of microgels are referred to as *neutral* microgels. Nevertheless, it is important to keep in mind that even neutral microgels are actually charged, considering that their synthesis typically occurs with initiators or surfactants that carry a small amount of charges [30]. Their role on the structure of the microgels is still largely unexplored and *de facto* it is assumed that these charges play an irrelevant role. The only study performed in this regard seems to actually confirm this hypothesis, at least as long as the microgel concentration remains low [39].

Following different protocols, it is also possible to obtain different topologies or shapes, other than spherical. In particular, an increasing amount of work has been dedicated to the study of hollow microgels, which are made by an external polymeric shell, after the removal of the inner core [40–43]. Different post-fabrication strategies also allows to nanoengineer microgels for instance into ellipsoidal, faceted and bowl-like shapes [44, 45].

A key feature of microgels, as opposed to other colloidal particles, is their **responsivity to external stimuli**, which is linked to the ability of the particle to engulf a large amount of solvent [46, 47]. In this way, it is sufficient to unbalance the inside and outside osmotic pressures to induce a change in the particle size until osmotic equilibrium is reached [5, 28]. The most straightforward way to exploit this responsivity is to act at the level of the polymer network, for instance, by employing a thermoresponsive polymer or by using a charged co-polymer in its synthesis. Hence, a change in the temperature of the microgel dispersion will induce a change in the single-particle size, from the swollen to the collapsed state, across a so-called Volume Phase Transition (VPT) temperature [5, 48]. One of the most studied polymers in microgels is poly-*N*-isopropylacrilamide (PNIPAM) that is known to exhibit a VPT at around 32°C. In this way, the microgel goes from being in an extended conformation, which is a condition that in polymer theory is also called good solvent, as opposed to the bad solvent conditions in

which the polymer collapses on itself [5]. The chemical compound typically used as crosslinker is *N, N'*-methylenebisacrylamide (BIS). Responsivity has allowed to exploit microgels in several applications, from catalysis [49, 50] to drug delivery [51, 52], from the production of lenses [53] to chemical sensing [54].

Actually, responsivity is the first aspect in which the **polymer-colloid duality** of microgels clearly emerges [28], providing an elegant way to control the microgel volume fraction by solely adjusting external parameters, without having to change the particle number density. Diverse fascinating experiments took advantage of this feature. Alsayed et al. [55] for example studied in real-time the premelting of a three dimensional colloidal crystal at a grain boundary. By slightly changing the sample temperature, they varied *in situ* the volume fraction of the particles in the crystal over a significant range, driving the crystal from close packing toward its melting point at a lower volume fraction, as displayed in Fig. 3.

A relevant role has been played by microgels in other fundamental studies, for instance to shed light on glassy and jammed states of thermal soft systems [56–59].

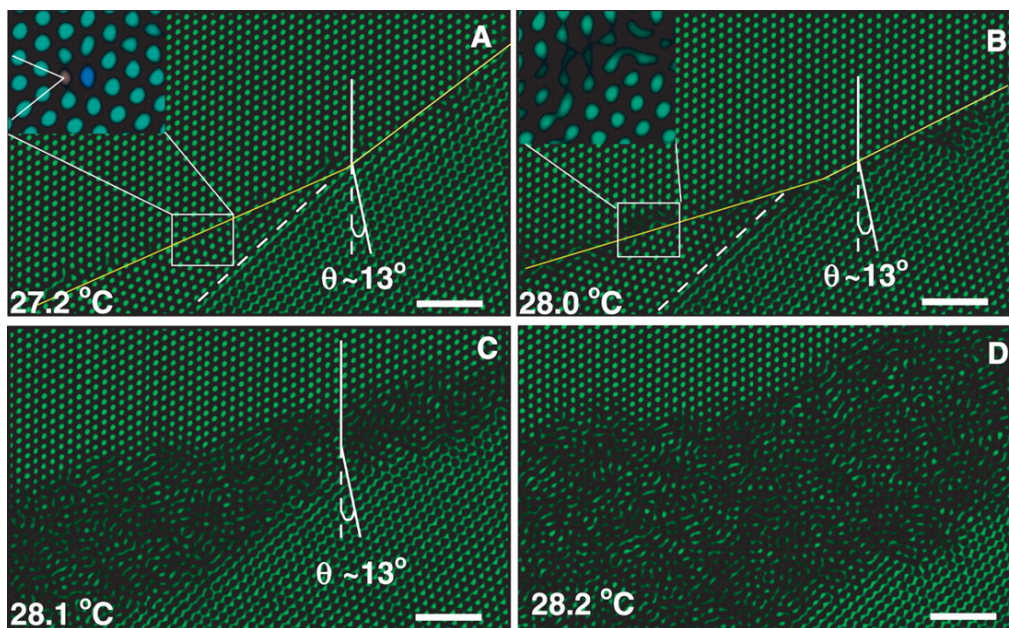


Figure 3: Premelting of a colloidal crystal in bulk. Reproduced from Ref. [55]. The figure shows images at different temperatures, and thus at different particle volume fractions, of two crystals separated by a grain boundary with a tilted angle of 13° . Temperature increases from (a) to (d). In (b) the grain boundary starts to premelt and nearby particles undergo a liquid-like diffusion. The width of the premelt region increases with temperature. Scale bar is $5 \mu\text{m}$.

Emblematic is the case of the fragile-to-strong transition in glass formers according to which, based on the classification proposed by Angell in the nineties [60], it is possible to distinguish a given system on the basis of how steeply the viscosity of a liquid increases as the glass transition is approached. Hard spheres, for example, have a very steep behavior, described by a Vogel-Fulcher-Tammann law, and they thus form a "fragile" glass; on the contrary, a so-called Arrhenius behavior defines a "strong" glass. For the first time in 2009, through a much debated article [61], it was proposed that it was possible to move from a fragile behavior to a strong one by adjusting the softness of the particle. This relationship was demonstrated through the use of interpenetrated microgels (IPN), in which a first neutral polymeric lattice is crossed by a second charged one. This work has generated a series of subsequent studies, also recently. For example, it has been shown that a systematic increase in the amount of the charged polymer induces a change in the glassy behavior leading to a strong glass [62]. Another group instead has proposed a model that is able to explain microscopically the fragility for a series of soft colloids, from microgels to star polymers or proteins [63].

Responsivity, softness and deformability undoubtedly enrich the behavior of any dispersion composed of microgels. In addition, we should consider the possibility of further tuning the softness of the network through the concentration of crosslinkers, or possibly by changing the topology. Therefore, **a complex phase diagram has to be expected**, whose dependence on temperature and packing fraction is not trivial at all. Over the years, various contributions have attempted to determine the phase behavior of microgel particles both by means of experiments or computer simulations. In general, such studies evidenced how microgels suspensions undergo the same sequence of transitions as the hard sphere reference system with increasing volume fraction, despite several quantitative differences arise [25, 28]. In particular, below the VPT temperature, the phase behavior is reminiscent of that of hard spheres. Being in the swollen state, in fact, (eventual) charges in the outer polymer chains unlikely contribute to the microgel interactions and the presence of a large amount of solvent in the particle makes van der Waals interactions between them also negligible [64, 65]. Indeed, as reported in earlier contributions, in this regime microgels are known to crystallize from

the fluid state into the face centered cubic structure expected for hard-sphere suspensions [66]. Independently, Senff, Richtering and co-workers [67, 68] also determined that, approaching the VPT from lower temperatures, microgels behave as hard spheres up to $\phi \sim 0.5$ while a softer interaction potential is needed to describe their behavior at higher packing fractions. In the same work, they also reported a shift in the fluid-solid boundary and a narrower phase coexistence region compared to the hard sphere case. In this regard, there seems to be no univocal agreement [69] because, depending on the peculiarities of the chemical synthesis, regions of coexistence similar [70, 71] or greater [72, 73] than that typical of hard spheres have also been found. More recently, it has been shown that modeling interactions via the elastic Hertzian model [74] or via a harmonic potential allows to reproduce in a more accurate fashion the fluid region of the phase diagram [56, 71, 75–77].

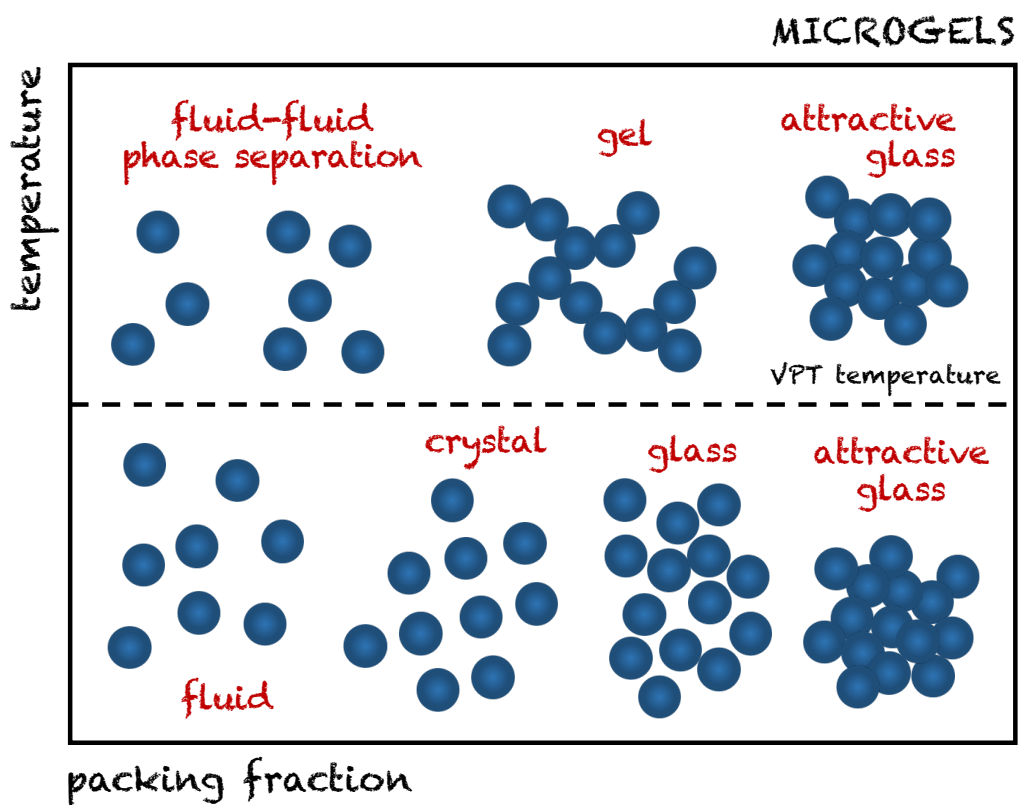


Figure 4: Microgel phase diagram in bulk. Sketchy state diagram showing temperature and packing fraction dependence for microgels in bulk. The VPT temperature is also reported as a dashed line.

A different situation, as is to be expected, emerges for temperatures in which microgels are found in the collapsed state. There, specifically, intermolecular van der Waals interactions becomes too strong and the microgel behavior could result in fluid-fluid phase separations or in arrested phases as in gels, depending on the volume fraction [78, 79]. The soft nature of microgels is fully revealed at considerably high packing fractions, which could be reached thanks to the constituting polymer network. This allows particle to be compressed well above the hard sphere jamming transition by strong interpenetration of the polymer chains and by adjusting volume and shape of the particle [80–85]. In this regime, predictions of the presence of an attractive glass have been put forward by means of mechanical spectroscopy measurements [79]. A tentative phase diagram showing the intricate behavior of bulk microgels, as compared to the hard sphere behavior, is reported as a function of temperature and packing fraction in Fig. 4.

From this overview, it clearly emerges how a unified description of the phase behavior of microgels is still far from being achieved. From a theoretical perspective, in particular, there has been **no consensus in the years on a functional form of the effective interaction potential** that could describe the microgel behavior under different experimental conditions. This kind of research has been very limited, both because of the complexity of the problem itself and also for a purely technical aspect – not easy to overcome in the short term – which concerns the computing power available to the scientific community. For these reasons, there are many experimental studies that are not adequately supported by a theoretical and computational counterpart, of which the microgel phase behavior is a striking example. The few theoretical studies have (rightly) focused on the soft and elastic nature of the particle, thus elaborating potentials focused on this specific aspect, such as the Hertzian one. However, a fundamental aspect that has been overlooked, which could be instead very promising, lies in the fact that microgels are, after all, polymeric networks with an internal structure defined by crosslinked polymer chains. As the inner structure determines the single particle properties and, in turn, the bulk behavior of the system, a realistic description of such particles should take into account these aspects in order to capture the way they interact among themselves.

This approach was hinted in two different contributions where, provided the core-shell structure of standard microgels, the authors employed two-component brush-like models where either a compressible or incompressible core were surrounded by soft polymer brushes [77, 86]. Despite this, the theoretical predictions could not match other experiments performed at low temperature in a wide range of volume fractions [71]. The latest attempt to account for the internal polymer structure of microgels led to the so-called multi-Hertzian model, which relies on numerical calculations of the effective interaction potential of a realistic model for microgels [75]. At the basis of this phenomenological approach is the idea to ascribe a different elasticity to corona-corona, core-corona and core-core interactions, according to the different crosslinker concentrations in the different shells of the particle. The multi-Hertzian model turned out to correctly reproduce the experimental behavior of a binary mixture of microgels at different concentrations and temperatures. The latter, at the moment, thus appears as the most promising approach to exploit microgel phase behavior and allow for the widespread use of these colloids in several fundamental studies and for applicative purposes.

The potentialities of microgels are not limited to bulk suspensions, and appealing research lines are opening up to exploit these particles at interfaces. In fact, the intrinsic softness of microgels and, in general, of soft deformable objects, is fully revealed, and can be taken advantage of, at interfaces, which can be used to fulfill different purposes.

An interface is created whenever two immiscible phases come into contact, whether solid, liquid or gaseous. These are characterized by a surface tension which can be explained by the fact that a certain phase will attempt to reduce its surface to volume ratio as a consequence of the unfavorable contacts with the other phase and the reduced cohesion forces among similar molecules. Thus, the higher the cohesive forces between the molecules, the higher the energy to increase the surface area, and so will be the surface tension [87].

Of particular interest are fluid-fluid interfaces that are ubiquitous in nature and central to various industrial applications, from the production of chemicals

and pharmaceuticals [88–90] to the food industry [91, 92]. Fluid interfaces are especially encountered in emulsions which are droplets of one liquid phase dispersed in a second immiscible liquid. These mesoscopic structures are typically unstable from a thermodynamical point of view and, given the excess interfacial area, will tend to demix through droplet coalescence. However, if the interfacial tension is large enough, it is possible to coat an interface with nano- or microsized particles which then remains adsorbed, making the emulsion kinetically stable. In this respect, solid particles have been known to stabilize emulsions since the beginning of the twentieth century. The so-created Pickering emulsions involve rigid particles that are partially wettable in both phases and most of the time take advantage of electrostatic interactions between particles and interface or surface-engineered particles [93, 94]. Other well-established mechanisms for stabilization include the use of amphiphilic surfactants or proteins [95, 96].

Recently, **microgels have been experimentally explored when adsorbed at interfaces**, where the colloid-polymer duality, especially in terms of particle deformability strongly manifests [97–103]. Indeed, their internal polymeric structure allows them to spread and flatten at the interface to maximize their area, reduce nonfavorable contacts between the two liquids, and thus lower their surface tension. This phenomenology is always dictated by the **elasticity of the single objects**, in contrast with hard particles, in which the latter does not play a role.

In emulsions, the deformability of the particles allows to achieve larger interfacial tension loadings which is particularly convenient in the fabrication of capsules with controlled porosity [104, 105]. Also, microgels' deformability may be exploited for nanostructuring elements or for other high-end applications such as sensing, interferometry and biocatalysis [101, 106–109]. On the other hand, it allows to reach more densely packed regimes as compared to hard particles thanks to the compliance of the outer shells. In this way, for instance, it is possible to avoid coalescence upon severe droplet deformation [110].

Microgel responsiveness to external stimuli could trigger novel research on the so-called smart emulsions [106, 111]: by changing *in situ* the single-particle properties and the local environment, it is possible to finely control the stability and the structure of the whole monolayer or emulsion. A similar idea has been

exploited for the adsorption of thermosensitive microgels at the surface of giant unilamellar vesicles for which the authors found that, at low temperatures, microgels could adsorb at the interface according to an hexagonal packing while, at higher temperatures, the particles lost the crystalline order previously gained desorbing from the interface. From this experiment, it would be pretty clear that the swollen-to-collapsed transition is the key factor also to destabilize adsorbed microgels, although the underlying mechanism for this behavior is not yet fully clarified [112, 113]. At the same time, even the role of microgels in soft Pickering emulsions still awaits to be fully understood. In fact, while some researchers claim that the softness of a particle increases the stability of the emulsion [114–117], others reported that softness does not play a major role [118], or even that soft particles do not show appreciable advantages to stabilize fluid interfaces when compared to rigid particles, according to recent numerical simulations [112]. It should be also taken into account that some studies report the adsorbed particles as irreversibly attached to the interface, with an energy of the order of millions of times the thermal energy [115, 119], also provided the extended size of the particle with respect to the bulk. Active research in the field still needs to be carried out.

It is on **flat interfaces**, however, that more information on microgels could be gained. On one side, these are simpler systems, as any effects due to the curvature of the interface are avoided. On the other side, it is still an experimentally relevant condition that constitutes the precursor of a liquid-liquid emulsion and also captures some of the salient features of processes that exploit self-assembly and deposition from macroscopically flat fluid interfaces, the so-called Langmuir-Blodgett processes [120]. In these conditions, less than ten years ago, Geisel et al. [113] obtained the first characterization of microgel colloids deposited at a flat water/oil interface by means of freeze-fracture shadow-casting (FreSCa) cryo-Scanning Electron Microscopy (cryo-SEM) [121], as reported in Fig. 5. In a nutshell, this technique involves the freezing of a millimeter-size sample that is subsequently exposed upon fracture and imaged with cryo-SEM. The protruding part of the image is obtained by coating the fractured interface with a thin tungsten layer at a 30° angle relative to the interface, so that all the features protruding from the plane leave a shadow behind them. Besides confirming the enhanced

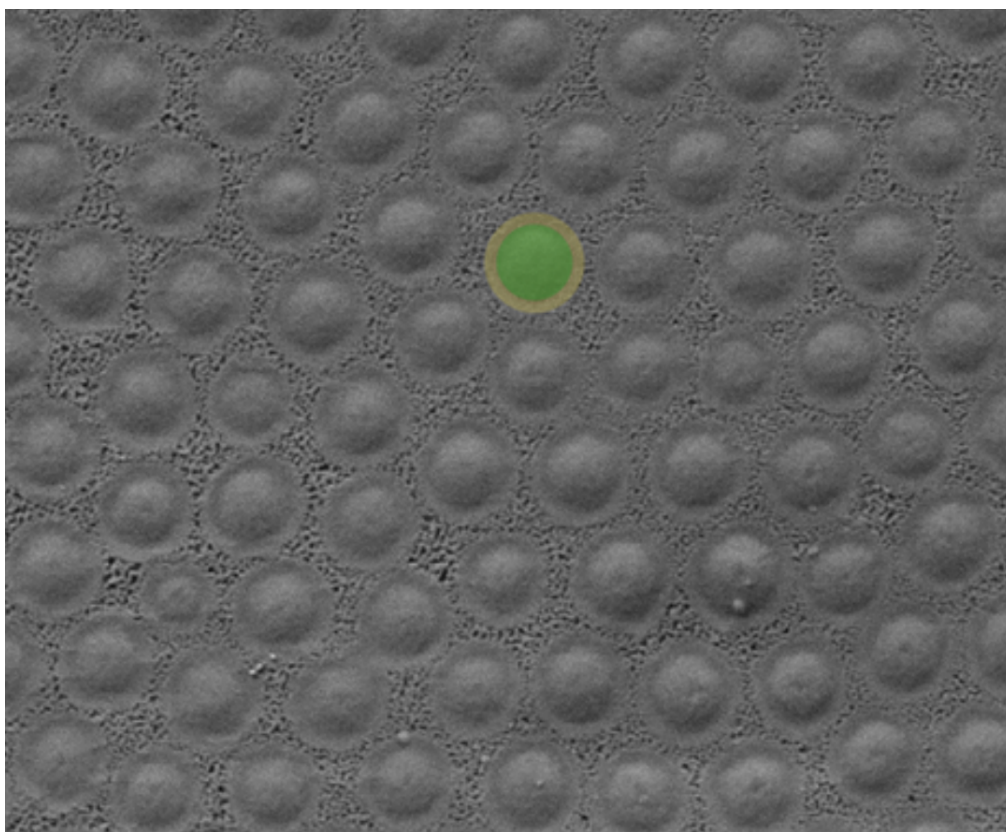


Figure 5: Microgels at a flat water/oil interface. Adapted from Ref. [113]. FreSCa cryo-SEM images of microgels at water/n-heptane interface. The colors highlight the core-corona nature of adsorbed microgels.

stretching on the plane of the interface as compared to the bulk, these experimental images of microgels at water/oil interfaces have evidenced a preferential protrusion of the microgel centers on the water side. This feature is the result of two main contributions: first of all, the higher solubility of PNIPAM chains in water induces the microgels to maximize the surface exposed to water; second, the fact that the crosslinking density of the microgels is usually not homogeneous and decreases toward the periphery of the particle implies that the inner core mostly retains its spherical shape also at the interface. As a result, the peculiar conformation of microgels at the liquid-liquid interface is usually referred to as a "fried-egg" shape [113, 114, 122–126]. An exception is constituted by the ultralow-crosslinked microgels, recently investigated by Scotti et al. [127], which were found to uniformly cover the interface like disks, thus behaving as a flexible polymer system, at low compression regimes.

It is now commonly agreed that there is a quite enhanced dependence of this typical shape on the microgel crosslinking density, according to which stiffer microgels undergo a smaller deformation at the interface [126]. On the contrary, interfacial activity seems to prevail over other parameters, such as the use of charged co-polymerized microgels and the tuning of temperature. In the former case, microgels were studied at acidic and basic pH, corresponding to neutral protonated state and negatively charged state, respectively [113]. While at basic pH the bulk diameter is increased with respect to that at low pH, the effect on the interfacial conformation of a single particle is minimal, with only a little increase in the protrusion toward the water phase and no appreciable difference in the extension on the plane of the interface. Similar outcomes have been obtained very recently for single-microgel as a function of temperature, whereby going to temperatures above that of the VPT affects at most the height of the particle across the interface [128]. These results, in particular, further highlight how the role of temperature for microgels adsorbed at the interface requires further systematic studies also in light of the potential use of microgels in the stabilization of emulsions.

The peculiar conformation and the confinement at the interface suggest that the collective behavior of these particles is very different from the bulk collective behavior. Moreover, it is influenced by a number of factors that have to do with the presence of the interface itself. This is the case, for example, of capillary interactions that are long-range attractions induced by the local deformation of the interface plane, as a result of effects due to gravity [129], usually leading to the formation of clusters and aggregates. Capillary forces are very often found for different types of particles but are supposed to be much weaker if the adsorbed colloids are small enough and at most in the order of a few hundred nanometers [130]. Other attractive forces might be present at contact at the microscopic level, such as van der Waals forces, although their magnitude is supposed to be not particularly relevant as a result of the enhanced stretched state in which microgels are found [131, 132]. The role of charges at the interface is instead indicative of how complex the interactions can be. In fact, experiments precisely performed on microgels, led contradictory results until now: while in one case a dependence

on the charge density of the microgel was made explicit [133], in another, the presence or absence of the charge was claimed to have no effect [134]. Lately, it has been observed that a relevant role is played by the size of the absorbed particles and even the hypothesis of a long range ordering as a result of electrostatic effects has been advanced [135].

The study of the collective behavior for microgels at interfaces have been limited in these years **mostly to the assessment of the experimental equation of state**, that is the variation of the surface pressure for changing area fraction [100, 128, 130, 136, 137]. Similar studies have been performed also at the air-water interface [119, 134]. In this way, for example, it is possible to study the emerging self-assembly patterns *ex post*, as a function of the concentration of the particles at the interface, or explore the variations in the equation of state by changing the properties of the adsorbed polymer. This is typically obtained by means of a Langmuir trough in which a microgel-laden fluid interface is continuously compressed. Unfortunately, a simple assessment of the experimental equation of state does not provide additional information, except for confirming the increase in surface pressure for increasing concentration of adsorbed polymers. Furthermore, it is not always straightforward to couple the microscopic behavior to the macroscopic equation of state, especially at high packing fractions where issues related to the detection limit of the pressure tensor could arise [119]. For these reasons, such studies are usually coupled to other investigations. Particles in fact are eventually transferred onto a solid substrate where it is possible to image the sample via Atomic Force Microscopy measurements, extract the pair correlation function or the bond order parameter, and gain information on the microgels structural arrangement. Thin microgel layers have been also researched by means of rheological measurements [138].

Investigations on the collective behavior has brought for example to the discovery of an isostructural solid-solid transition (see Fig. 6) between two crystalline phases with the same hexagonal symmetry but different lattice constants [100, 128]. This behavior emerges after low compression regimes in which, at first, particles form clusters driven by the attractive capillary interactions and, subsequently, reach the close packed state at higher pressures. These features observed macro-

scopically are intimately related to the properties of single microgel particles. In fact, it has been observed that stiffness and thickness of the outer shells allow to modulate the extent of this region and tune the increase in surface pressure [139]. If afterwards the interface is compressed further, some of the shell-shell contacts fail and clusters of particles in core-core contact start to appear. The solid-solid transition is also dependent on the size of single particles and it has been demonstrated that smaller microgels, whose distinction between core and corona is less evident, do not undergo this kind of transition thus simply compressing smoothly and monotonically [130]. Also in this case, information on the underlying structural features came mostly from the analysis of the interparticle distance

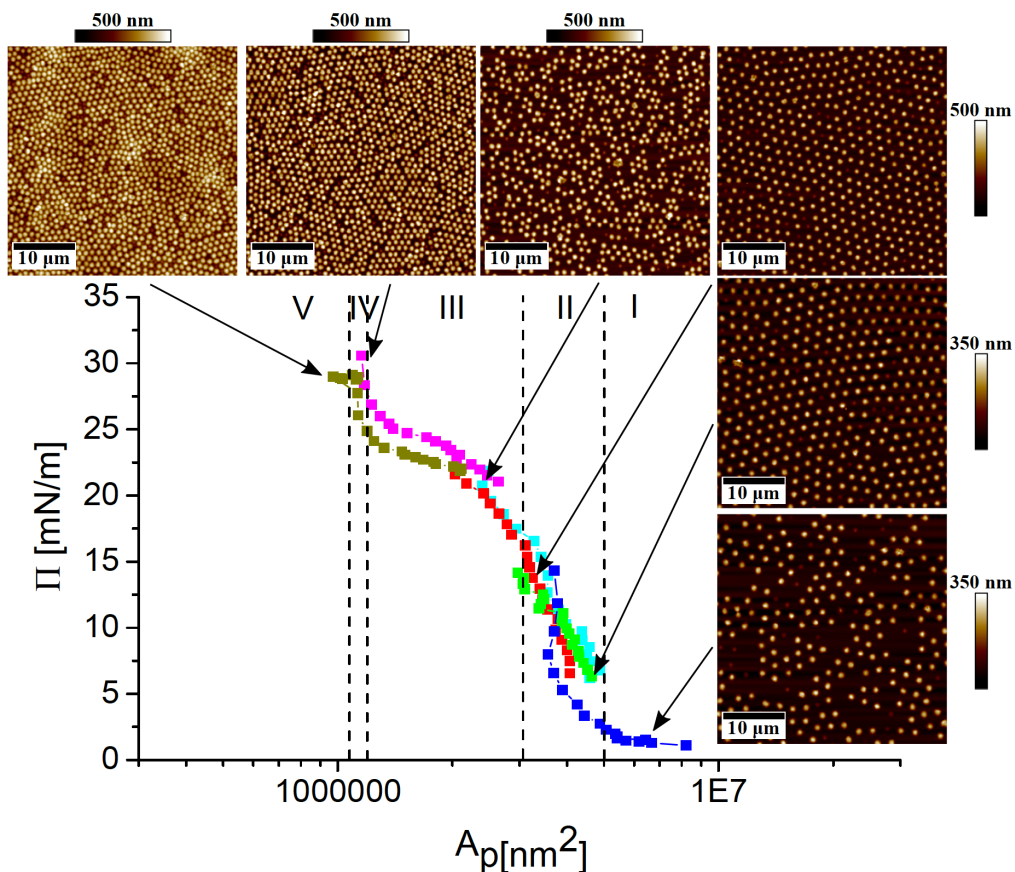


Figure 6: Isostructural transition. Reproduced from Ref. [130]. Experimental equation of state reporting the surface pressure Π versus the area per particle A_p . Regions I-V evidence the formation of different patterns, shown in the corresponding AFM images, from the formation of clusters and islands at low compression regimes, the hexagonal ordering, the isostructural transition and the buckling of the microgel layer at high compressions (low area per particle). Scale bar is 10 μ m and maximum 500 nm in height.

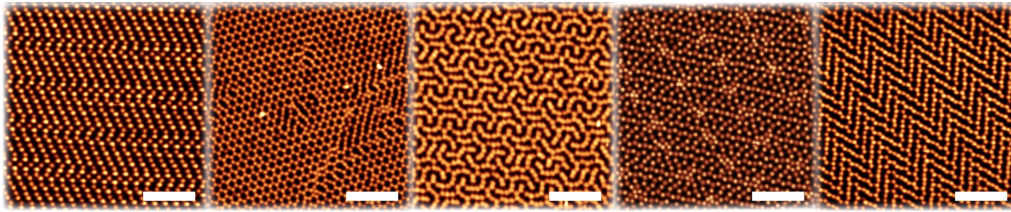


Figure 7: Patterns occurring with a two step deposition. Adapted from Ref. [142]. From left to right: rectangular lattices, honeycombs, interlocking-S structures, hexagonal and herringbone superlattices. Each panel represents an AFM image taken at different concentrations of the microgels deposited in the first and second steps. Scale bar is 5 μm .

extracted from AFM images. A strategy to account for the isostructural transition in numerical simulations of hard core-shell microgels is based on an augmented potential [140].

Except for this peculiarity, the typical arrangement of microgels at intermediate or high concentrations is that of a hexagonal ordering. Exceptions are found for small microgel particles, whose polydispersity is such to induce a glass-like disordered phase [130], although the specific conditions under which this behavior occurs are not known and yet remain unresearched. Different patterns have been observed through the realization of more complex systems. For example, Rey et al. [136] employed a mixture of rigid microspheres and microgels at the air/water interface. For different surface pressures, besides the typical hexagonal packing, they could observe other exotic phases such the square pattern and the chain phase. In this case, they argued that this behavior was mediated by the microgel disposition around the microspheres. In fact, they have been able to reproduce the experiments by means of numerical simulations of a hard core-soft shoulder potential, where the soft shoulder indeed represented the microgel particles [141]. Two sequential microgel depositions on a liquid interface allow also to obtain a plethora of different crystalline structures [142]. By simply varying the packing fractions of the two it is possible to obtain not only low coordinated phases but also rhomboidal or herringbone superlattices encoding non-regular tessellations. Some of them are shown in Fig. 7.

Besides all this, interfaces and surfaces represent a convenient tool where to perform research on new physical phenomena. The absorption at the interface, the formation of single (or multiple) layers, and the variation in packing fraction

make it possible to create new conditions which are useful both in basic and applied science. In the case of colloidal particles, softness and deformability enrich their behavior and microgels are one of the finest illustrations of this concept. Nonetheless, different phenomena still require major investigations, both at a single particle level and on the collective scale. For the specific case of microgels at the interface, the polymer-colloid duality still remains non-investigated, along the line of what was previously discussed for the bulk case. From previous evidences, it was not possible to gain clear information on the role of the surface tension and on the interface confinement on the polymer network and determine, for example, whether this could or not have consequences on the elastic properties of the microgel.

Despite the large amount of experiments performed, **theoretical investigations still lag behind**, being limited by subpar techniques and models. For instance, at the collective scale, it is not known yet how two standard microgels interact at the interface because a functional form of the effective interaction potential has never been extracted. To this aim, an accurate modeling of the single particle is a necessary condition and only in this way predictions on the collective behavior can be adequately obtained. Also, it remains to be clarified how the coarse-grained behavior at the interface is linked to that in the bulk and whether a parallelism can be drawn or if they actually behave as completely different systems. Clearly, a simple and blind transfer of results from bulk to interface would be highly inappropriate, due to the dramatic change of conditions between the two cases.

This lack of understanding hampers the progress toward further applications, since an established fundamental knowledge of the basic constituents would make it possible to a priori design and guide the assembly of innovative materials and nanostructures. From a theoretical standpoint, it also prevents the adoption of microgels at interfaces as model systems for the study of open questions in fundamental science. In this regard, despite the difficulties associated with a particularly complex system, much more progress has been made in bulk rather than at the interface. In fact, as discussed earlier, several studies in bulk have highlighted how microgels can be a valuable tool for studying, for example, the glass

transition or the fragile/strong classification of glasses, which are long-standing issues in soft matter physics. At the interface, this level of understanding has not been reached yet, perhaps because a systematic study of such system has been lacking in the past years.

It is therefore compelling to build a new approach that move from the components of the system – microgel, solvent, interface – in order to disentangle the different contributions of the single physical ingredients to achieve a satisfactory description of the overall collective behavior of microgels at the interface. This is the ultimate goal of this Thesis, that will be pursued mainly by means of Molecular Dynamics simulations validating numerical results with experiments whenever this is possible.

A recurrent aspect in the development of the Thesis is the approach to the study of microgels from the perspective of a polymer, since the colloid-polymer duality is the characteristic that mainly influences the properties of microgels. A second important aspect has to do with the so-called coarse-graining: the large amount of atoms that compose a complex polymeric network such as a microgel only allow for a mesoscopic treatment of the particle. All these aspects will be the basis of Chapter 1 of this Thesis. After reviewing the main mesoscopic models that have been developed in recent years by the scientific community, we will present the single-particle microgel model used for the proceeding of the work. In particular, building on the work proposed by Gnan et al. [143], we will describe how to computationally model a microgel that takes into account, for example, an irregular distribution of crosslinkers between the core and the outer shells, as typically result from the chemical synthesis.

The second step in the single-particle assessment is represented by the modeling of the solvent. Microgel colloids are able to retain a large amount of solvent in the swollen state and the thermodynamic parameters of the dispersion affects their responsiveness. Numerically, solvent effects can be taken into account in an implicit or an explicit way, that is either by considering a potential acting within the microgel model or by adding (coarse-grained) solvent particles in the

simulation box. Chapter 2 will be thus be devoted to determine which kind of solvent is the most suitable to describe microgel particles in such a way that no artifacts appear in the modeling. In this way, we will be also able to provide information on the solvent uptake in the polymer network and on its role on the collapse kinetics on changing the surroundings conditions. On the other hand, the inclusion of explicit solvent in the modeling is fundamental for the creation of a liquid-liquid interface in numerical simulations.

Along these lines, we build the numerical model to describe microgels at a fluid interface, which will be discussed in Chapter 3. In particular, we will take advantage of the experimental assessment of single microgels at a water/oil interface, studied by means of the AFM and FreSCa techniques, to build a sound model that reproduces the main features of such particles when adsorbed at an interface, for increasing concentration of crosslinker in the polymer. This will also make it possible to perform a first study on the effects that the interface has on the polymer network. In particular, we investigate the case of modifying the surface tension by changing the combination of fluids constituting the interface.

In Chapter 4 we thus determine the two-body interaction potential moving from the model previously built for one microgel at the interface. This amounts to extract the probability for two microgels to remain at a certain distance under the influence of a bias harmonic potential. While previous experiments were based on the study of the structures generated for different packing fractions, with this approach we determine a functional form of the inter-particle potential *a priori* and thus use this information to foresee the microgel phase behavior for different physical conditions. In fact, by studying the dynamical behavior, we predict the presence of multiple reentrant phenomena where, by increasing the particle density, microgels first arrest and then refluidify due to the high penetrability of their extended coronas. Furthermore, by fitting the numerical interaction potential we determine the microgels' Young's modulus and relate it to the crosslinking density of the polymer network, once again demonstrating the importance of considering the polymeric nature of these soft colloids. In addition, building on a numerical method developed for soft particles in bulk conditions, we estimate the

other elastic moduli (bulk and shear moduli and Poisson ratio), and demonstrate a significant stiffening of the microgels polymer chains with respect to the bulk.

Chapter 5, finally, is devoted to the analysis of a different microgel topology, that of hollow particles. Building on the numerical method for the *in silico* synthesis of standard core-corona microgels, we elaborate a synthesis procedure for such particles. More specifically, we compare numerical and experimental single hollow particles as a function of the shell thickness, unveiling interesting structural features upon varying the temperature.

The remaining sections of this Thesis include a summary of the main outcomes with a discussion on the future perspectives, and a brief description of parallel work on charged microgels.

Chapter 1

In silico microgel modeling

This Chapter presents the microgel model that will be employed in the proceeding of the Thesis. Particular attention will be devoted to introducing a realistic crosslinker distribution within the microgel particle, according to experimental evidences reported for the precipitation polymerization synthesis protocol.

1.1 Numerical design of coarse-grained microgels

Microgel colloids, being complex macromolecules whose diameter can range between tens of nanometers to one micrometer, intrinsically involve the presence of many atoms constituting their polymeric backbone. The numerical treatment of full microgel particles in an all-atom fashion, also called the atomistic approach, is still out of reach for the lack of computational power to treat such enormous amount of atoms. Still, it is possible to focus on parts of the network such as single chains or at most small lattice meshes. These kind of models allow to study processes that occur at the atomic or the molecular length- and time-scales, but whose microscopic effects have repercussions at the higher scales. In the context of microgels, high-resolution atomistic models allow, for example, to understand the molecular mechanism that drives the cooperative coil-to-globule transition of PNIPAM chains in water, which is linked to a breaking of the hydrogen bonding network formed by water molecules in the proximity of the hydrophobic groups of PNIPAM [144, 145].

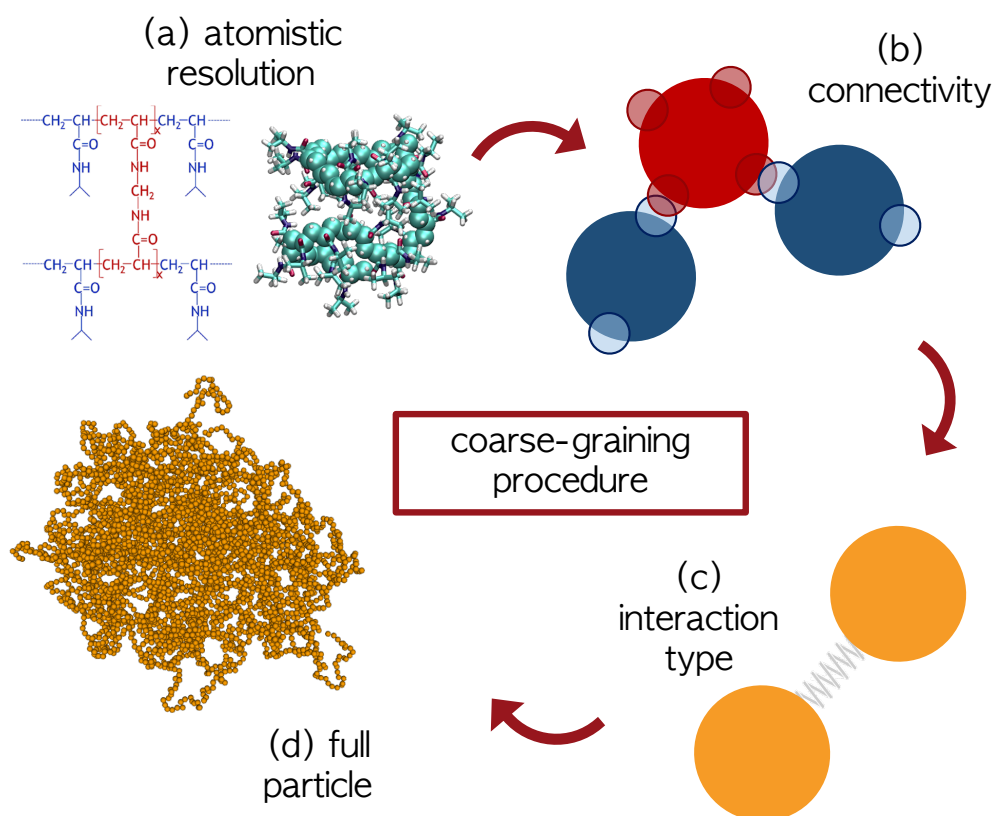


Figure 1.1: General coarse graining procedure. Sketch of the coarse-graining procedure for the design of microgels, from the chemical composition to the full assembled particle. (a) A BIS crosslinker connect four other monomers of NIPAM; chemical representation of a PNIPAM chain; (b) beads connectivity of monomers and crosslinkers; (c) the interaction among the beads is defined; (d) final coarse-grained polymer network.

In this Thesis, however, the final goal is to study the collective behavior of microgel particles. Hence, in order to reach this kind of description, an approach based on the atomic detail does not bring any advantage. A useful representation is that of a monomer-resolved polymer, in which the smaller degrees of freedom are discarded in favor of a mesoscopic study of single microgels, where groups of atoms or molecules are mapped onto specific interaction sites [11, 12]. To this aim, the chemistry of the polymer network can still help in finding an appropriate coarse-graining protocol. Fig. 1.1(a) reports, as an example, the detail of a PNIPAM chain, in which a central crosslinker links four other NIPAM monomers. This picture makes particularly evident the *general* coarse-graining protocol that is typically performed to build a polymeric structure, according to which monomers and crosslinkers are associated to a single bead. Instead, the chemical details emerge

1.1 Numerical design of coarse-grained microgels

in the connectivity of the two species involved: the monomers are connected two by two forming the polymer chains while the crosslinkers bind different chains and therefore have a four-folded connectivity [143]. In the comparison to real polymers, the size of the beads is typically linked to the so-called Kuhn length b , that is related to the representation of a polymer chain as a N step random walk of Kuhn segments each of length b [5, 146]. The proper choice of b ensures that the model reproduces the end-to-end distance at full extension and the mean squared end-to-end distance for targeted polymers. In most cases, the Kuhn length is of the order of the nanometer and usually increases with the molecular weight of the polymer units [147]. As shown in Fig. 1.1, once the connectivity of the polymer is defined, one has to consider how different beads interact among themselves in the overall mesoscopic model, as will be later clarified.

The numerical investigation of coarse-grained microgel particles that could take into account the polymeric nature of the microgel in a mesoscopic fashion started about ten years ago. Since that time, different models and approaches have been proposed, some that simply aim to build a generic network, others inspired by laboratory chemical synthesis procedures [31, 148].

The simplest microgel is that built on a regular diamond lattice, the so-called diamond-lattice-based model [128, 149–152], which consists of placing the crosslinkers on a crystalline structure and connect them with equal-size chains, as shown in the simulation snapshot in Fig. 1.2. Despite representing a polymer network, the description provided by the lattice model is too much simplified, and should thus be employed only in specific cases with caution. The main limiting factor is the regular size and distribution of the polymer chains and crosslinkers, which has no counterpart in any microgel particle. In fact, just considering the standard experimental protocol of precipitation polymerization, crosslinkers are known to react faster than monomers thereby concentrating in the core of the particle. Besides, the diamond lattice structure does not permit to control the structure of the corona, deprived of loops or dangling-ends, contrary to what is typically found in laboratory microgels [36, 153].

Nikolov et al. [154] generated disordered networks by randomly distributing the crosslinkers in a simulation box and by connecting them with polymer chains

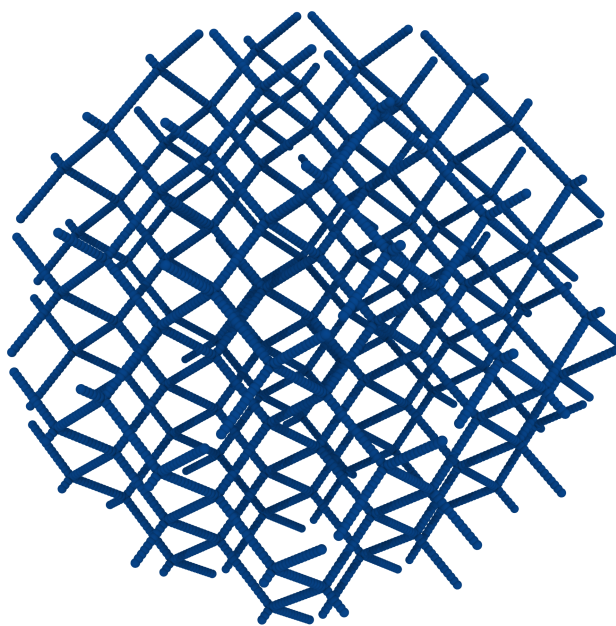


Figure 1.2: Diamond-lattice-based microgel. A polymeric network is built on a regular diamond lattice: crosslinkers have regular sites and are connected by equal-size chains. The snapshot does not report an equilibrated configuration.

within a certain cut-off distance. In principle, it is possible to obtain non-regular crosslinker distributions displacing them initially in a non-regular way.

Other methods developed by different research groups are inspired by the experiential synthesis procedures, either the precipitation polymerization or the microfluidics fabrication method. In the former case, Rudyak et al. [155, 156] consider in the simulation box an initial "solution" of particles with valence one, two and four representing initiator, monomers and crosslinkers. Next, a series of events, mimicking the chemical reactions shall happen according to pre-defined probabilities. These are the initialization reaction, between monomers and initiators, the monomer-monomer addition, among monomers, and the monomer-crosslinker addition reaction: at each step the monomers initially activated by the initiator pass the active center to the other species. This very recent protocol was reported to have realistic density profiles and a loose corona, with the portion of dangling ends representing half of the total mass of the microgel. On the other hand, the microfluidic fabrication of microgels is a procedure that relies on the existence of macromolecular precursors. In particular, microgels are obtained by crosslinking pre-existing polymer chains which are functionalized by reactive

groups, typically by light-induced chemical reactions [157, 158]. Numerically, this protocol is replied by assigning a certain fraction of active sites on fully assembled polymer chains which will form, during the simulation, permanent bonds. In this way, it is possible to obtain disordered networks in which the number of initial chains is independent on the number of crosslinkers, allowing to prepare microgels with different densities at a fixed concentration of crosslinkers [159].

1.2 A realistic model for microgel particles

The *in silico* microgels used in this Thesis are based on the assembly protocol originally proposed by Gnan et al. in Ref. [143]. The polymeric network is obtained by exploiting the self-assembly of patchy particles which are soft particles decorated on their surface with a certain number of attractive "patches". The reason for employing such particles resides in the fact that they are known to generate gels and other complex networks upon variation of their valence, in specific conditions of temperature and density [160]. In the specific case of microgels, the valence of the patchy particle is chosen according to the connectivity of monomers and crosslinkers. Thus, two and four folded patchy particles are assembled in a spherical cavity, to grant the formation of a spherical colloidal network, in a disordered fashion.

The interaction potentials involved in this process are a short-range repulsion between beads and a short-range attraction between patches of different particles. The former is encoded in the so-called Weeks-Chandler-Anderson potential V_{WCA} , that is a common Lennard-Jones potential just shifted in order to retain the repulsive part only [161]:

$$V_{\text{WCA}}(r) = \begin{cases} 4\epsilon \left[\left(\frac{\sigma}{r}\right)^{12} - \left(\frac{\sigma}{r}\right)^6 \right] + \epsilon & \text{if } r \leq 2^{\frac{1}{6}}\sigma \\ 0 & \text{otherwise} \end{cases}. \quad (1.1)$$

In Eq. 1.1 (and throughout the text), ϵ sets the energy scale, σ is the diameter of a single bead, which in coarse-grained simulations also defines the unit of length, and r is the distance between two particles. The interaction between a patch μ on particle i and a patch ν on particle j reads as [143, 162]

1.2 A realistic model for microgel particles

$$V_{\text{patch}}(r_{\mu\nu}) = \begin{cases} 2\epsilon_{\mu\nu} \left(\frac{\sigma_p^4}{2r_{\mu\nu}^4} - 1 \right) e^{\frac{\sigma_p}{r_{\mu\nu}-r_c} + 2} & \text{if } r_{\mu\nu} \leq r_c \\ 0 & \text{otherwise} \end{cases} \quad (1.2)$$

where $\sigma_p = 0.4$ sets the position of the attractive well of depth $\epsilon_{\mu\nu}$, r_c is set by imposing $V_{\text{patch}}(r_c) = 0$, with $r_c = 1.5\sigma_p$. Interactions are selectively switched on and off setting $\epsilon_{\mu\nu} = \epsilon$ for monomer-crosslinker and monomer-monomer interactions, while $\epsilon_{\mu\nu} = 0$ for interactions among crosslinker provided they do not react among themselves. In this way, the total interaction potential for the patchy particles in the assembly process is given by $V(r, r_{\mu\nu}) = V_{\text{WCA}}(r) + \sum_{\mu} \sum_{\nu} V_{\text{patch}}(r_{\mu\nu})$.

The assembly protocol proceeds until most of the beads have assembled into a single network, ensuring that a minimum energy configuration is reached. Hence, the topology thus obtained is preserved by replacing the non-permanent interactions with a set of interactions typical of a polymeric structure and in particular with those of the Kremer-Grest bead-spring model [163, 164]. This renowned model became the gold standard for modeling polymers since the end of the eighties and was introduced with the main goal of accounting for excluded volume interactions between particles and for the non-crossability of the chains. In this way, numerical simulations could play a role in understanding the behavior of polymeric systems in comparison to experiments, provided that detailed analytical theories could only be worked out for ideal systems [5, 165]. For this purpose, the interaction potential is chosen as the V_{WCA} for the bead-bead potential, which allows a quasi-hard sphere behavior at short separations despite being a soft potential at larger distances. Neighboring particles interact also via the Finite Extensible Nonlinear Elastic (FENE) potential

$$V_{\text{FENE}}(r) = -\epsilon k_F R_0^2 \ln \left[1 - \left(\frac{r}{R_0 \sigma} \right)^2 \right] \text{ if } r < R_0 \sigma \quad (1.3)$$

where $k_F = 15$ quantifies the strength of the spring and $R_0 = 1.5$ represents the maximum extension of the bond. The use of the FENE potential, together with an appropriate choice of the parameters, allows to trap the beads in an infinitely large

1.2 A realistic model for microgel particles

potential well which cannot be overcome, effectively preventing polymer chains to pass through each other. On the contrary, the use of a simpler harmonic potential would allow for the distance between the two bonded particles to be much more extended, not necessarily solving the problem of chain-crossing [165–167]. The Kremer-Grest model we employ is also widely used for the investigations of other issues in polymer theory such as branching or chain polydispersity; current research is aimed at improving the model by adjusting the chain stiffness in order to tune the original model to specific real polymeric systems [146, 168].

Simulations of such polymeric systems or, in general, of colloidal dispersions, are typically performed in the NVT canonical ensemble, fixing the reduced temperature of the system $T^* = \frac{k_B T}{\epsilon} = 1$. For the purposes of this Thesis, we either employ the Langevin or the Nosé-Hoover thermostats [169]. The former describes the brownian motion of the colloids in a fluid due to the collision of the smaller solvent particles via the well known Langevin equations [4]; in the latter case an additional degrees of freedom is added to the Hamiltonian of the system to represent the coupling to the heat bath. In both case, the equations of motions are integrated via the velocity-Verlet algorithm [169].

We signal that other techniques are also employed in modeling microgels [170]. In particular, dissipative particle dynamics (DPD) is a particle-based method in which each bead represent mesoscale molecular clusters and fluid volume, thereby mimicking a polymer immersed in a viscous solvent. One of the main advantages of DPD is that beads interact via a soft bounded potential (at zero distance the potential has a finite value) allowing for the investigation of extended time scales, which would be unfeasible with common hard-core-like potentials. The drawback of using DPD in modeling polymer systems is precisely chain-crossing, as the energetic barrier between beads is easily overcome. It is therefore necessary to employ corrections, such as the so-called soft segmented repulsive potential [171], to the standard DPD model for preventing the violation of the topological polymer constraints [159].

The microgel model thus obtained retains most of the features of microgels synthesized via the precipitation polymerization protocol, such as the core-corona

1.2 A realistic model for microgel particles

structure. However, we stress that this feature does not arise from an inhomogeneous distribution of crosslinker given that, before the beginning of the self-assembly, all the patchy particles, both with valence two and four, are randomly distributed in the spherical cavity: the corona spontaneously arises from the interfacial region formed by the system due to the presence of the confining field. We remark that in the experimental synthesis the formation of the outer region is subsequent to a different reactivity of monomers and crosslinkers, which bring the latter in a higher amount in the central core region. Both for this reason and for the dynamical process that lead to the formation of polymer network, this assembly protocol does not reproduce the experimental non-equilibrium processes occurring in formation of laboratory microgels. Instead, the goal is to obtain a microgel whose main structural features resemble the experimental ones. In this respect, this assembly protocol allows to obtain a fully-bonded disordered network in which number of monomers, crosslinkers and density are fully tunable parameters. In such a way, it is possible to obtain microgels with a more compact and uniform structure or fluffier microgels with more dangling ends in the periphery of the particle. This is shown in Fig. 1.3 where we report simulation snapshots as a function of both crosslinker concentration c and confinement assembly radius Z .

The Kremer-Grest bead-spring model reproduces the microgel behavior in swollen conditions, that is at low temperatures, below the VPT. Here, we will introduce a way to mimic the typical thermoresponsivity of PNIPAM as a function of temperature in an implicit way, that is by adding an attractive potential between monomers. The potential reads as:

$$V_\alpha(r) = \begin{cases} -\epsilon\alpha & \text{if } r \leq 2^{1/6}\sigma \\ \frac{1}{2}\alpha\epsilon \left\{ \cos \left[\gamma \left(\frac{r}{\sigma} \right)^2 + \beta \right] - 1 \right\} & \text{if } 2^{1/6}\sigma < r \leq R_0\sigma \\ 0 & \text{if } r > R_0\sigma \end{cases} \quad (1.4)$$

with $\gamma = \pi \left(\frac{9}{4} - 2^{1/3} \right)^{-1}$ and $\beta = 2\pi - \frac{9}{4}\gamma$ [172]. The depth of the attractive well can be easily tuned via the α parameter, allowing to cover the entire range of temperatures usually exploited experimentally. In the $\alpha = 0$ limit, low temperatures

1.2 A realistic model for microgel particles

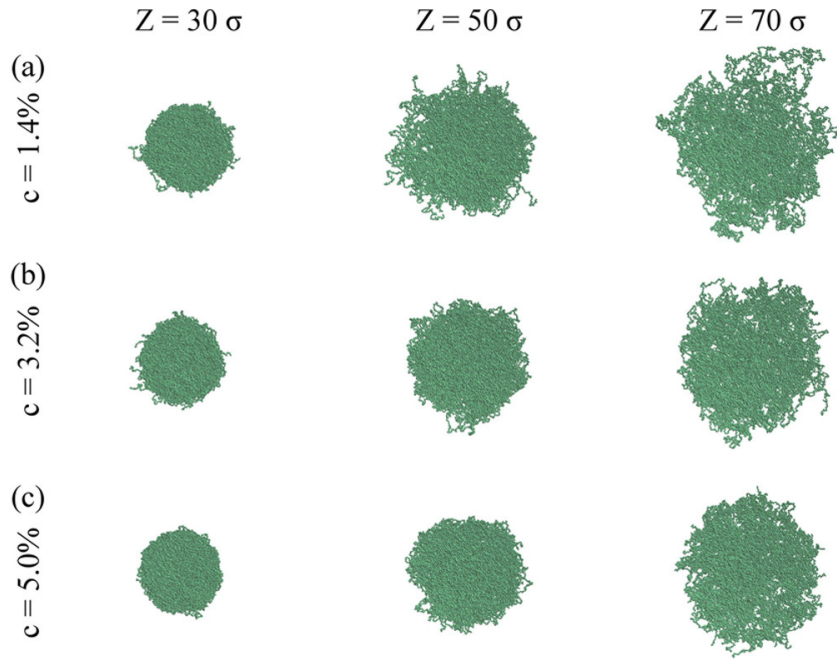


Figure 1.3: Compact or fluffier microgels. Adapted from Ref. [143]. Simulation snapshots of microgels with (a) $c = 1.4\%$, (b) $c = 3.2\%$, (c) $c = 5.0\%$ and confinement radius $Z = 30, 50, 70\sigma$ (from left to right).

are reproduced, so that the standard Kremer-Grest model is recovered. In the next Chapters, we will describe a valid and efficient way for reproducing this effect having explicit solvent particles in numerical simulations. In particular, we will discuss the DPD framework in relation to the Flory-Huggins theory.

Having defined a way to reproduce the polymer responsiveness, it is interesting to study how the swelling behavior is influenced by the assembly parameters, such as the confining radius Z . This is reported in Fig. 1.4 for a crosslinker concentration of 3.2% and microgels assembled with $N \approx 42000$ monomers. In the y-axis, we report the swelling ratio, defined as the normalized radius of gyration $R_g/R_{g,max}$ with

$$R_g = \left[\frac{1}{N} \sum_{i=1}^N (\vec{r}_i - \vec{r}_{CM})^2 \right]^{\frac{1}{2}} \quad (1.5)$$

where r_i is the position of i -th monomer and r_{CM} is the position of the center of mass of the microgel; $R_{g,max}$ is the maximum R_g obtained in swollen conditions ($\alpha = 0$). Swelling curves are shown as a function of the swelling parameter α .

1.3 Tuning the crosslinker concentration in the polymer network

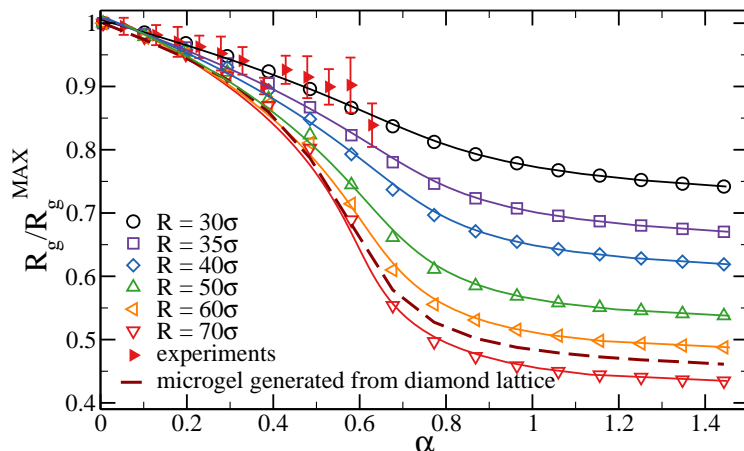


Figure 1.4: Swelling ratio as a function of Z . Adapted from Ref. [143]. Normalized radius of gyration $R_g/R_{g,MAX}$ as a function of α . Open symbols are simulation outcomes obtained for a microgel with $N \approx 41000$ monomers, $c = 3.2\%$ and various confining radii from 30 to 70σ . The dashed line is the numerical swelling curve obtained with a diamond-lattice based model. Filled symbols are results from DLS experiments.

It is evident how a larger confining radius allows for larger swelling ratios as a result of the lower density with which the particle is assembled. On the contrary, the size of the most compact microgel is only reduced by a quarter of its size at low temperatures. This particular microgel can be compared to the experimental swelling curve obtained from Dynamic Light Scattering experiments of microgels with small dimensions, having diameter in the swollen state of around 50 nm, also reported in the Figure: the tunability of the monomer density and size is therefore confirmed as a relevant aspect of the microgel modeling.

1.3 Tuning the crosslinker concentration in the polymer network

The major drawback in this modeling procedure is related to the internal distribution of the monomers. Crosslinkers in particular do not present a inhomogeneous distribution, so that the core-corona ratio is not realistic especially for big microgel particles. In order to overcome this issue, we put forward a novel numerical methodology based on that discussed in the previous section where microgels with desired internal density profiles are generated. In particular, we

1.3 Tuning the crosslinker concentration in the polymer network

introduce a designing force on the crosslinkers that is able to tune the core-corona architecture independently of the system size. By carefully adjusting the force field and intensity, we obtain individual microgel particles that quantitatively reproduce the experimentally measured form factors and density profiles across the VPT. It is also interesting to quantify the effect of coarse-graining on the structure of the *in silico* microgels by performing investigation as a function of simulated system size.

1.3.1 The choice of the designing force

Here, we specifically target the reproduction of the topology of PNIPAM microgels synthesized using free radical precipitation polymerization [37]. As already mentioned, for these particles, the core slowly rarefies from the center towards the corona, resulting in linearly decreasing density profiles, as observed through super-resolution microscopy [173]. Also the corona should be reproduced with the correct width and shape. To obtain such an inhomogeneous crosslinker distribution within the microgel, we apply a force acting on crosslinkers only. Indeed, if the force is applied on all the monomers, the resulting density profiles is much more homogeneous than in experiments.

However, the exact shape that the force should assume is not *a priori* obvious. In order to obtain the desired density profile, we have tested different functional forms of the force and compared the results with the unperturbed case, *i.e.* the

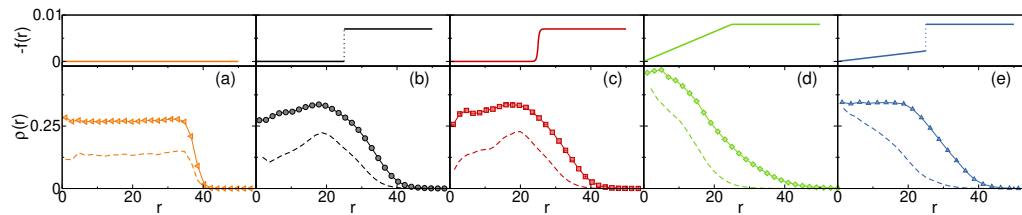


Figure 1.5: Forces acting on the crosslinkers and density profiles. Different types of forces acting on crosslinkers (top panel) and corresponding density profiles for all particles (symbols) and for crosslinkers only (dashed lines). In the five panels different inward forces, acting only on crosslinkers, are considered: (a) No force, (b) a force as in Eq. 1.6 with $g = 8 \times 10^{-3}$ and $k = 0$; (c) a force as in Eq. (1.7) with $m = 7 \times 10^{-3}$ and $t = 0.3$; (d) a force as in Eq. 1.6 with $g = 8 \times 10^{-3}$ and $k = \frac{2g_1}{Z} = 3.2 \times 10^{-4}$; (e) a force as in Eq. 1.6 with $g = 8 \times 10^{-3}$ and $k = 4.5 \times 10^{-5}$. In all cases, the integral of $\rho(r)$ is normalized to a constant value $\int \rho(r) dr = c$ with $c = 10, 5$ for all particles and crosslinkers, respectively, to improve visualisation. Data are averaged over four independent realizations. Case (e) is the one finally adopted to compare with experiments in the following Sections.

1.3 Tuning the crosslinker concentration in the polymer network

assembly in the absence of a force that was adopted in Ref. [143]. In all cases, the assembly is carried out by fixing the total number of particles to $N = 42000$ with a fraction of crosslinkers equal to 5%. We confine the system in a spherical cavity of radius Z , which determines the number density and the size of the final microgel. Using too small or too large values of Z gives rise to microgels that are either too compact or too fluffy, very far from the core-corona structure. We thus select the intermediate value of $Z = 50\sigma$, which correspond to a number density $\rho \sim 0.08$, that provides the best conditions to reproduce experiments with the additional force on the crosslinkers. All the configurations are realized using the protocol previously described in Section 1.2.

In Fig. 1.5 we report an illustration of different choices of the designing force as a function of the distance from the center (top panels) and the associated density profiles (bottom panels) for all the monomers (symbols) and for crosslinkers only (dashed lines). In the absence of a designing force, shown in Fig 1.5(a), we find that the microgel is made of a homogeneous core and of a rapidly decaying corona. This is reflected by the flat density profile of the crosslinkers. The situation gets worse when we increase the microgel size: since the decay of the corona happens only at the microgel surface, the increase of the volume/surface contribution gives rise to an unrealistically thin corona (see also below).

Ideally, instead, we would like to be able to maintain the same ratio of the extent of the corona with respect to the extent of the core (corona-core ratio) when we vary the microgel size, in order to have a valid protocol that is applicable to any N . Thus, we need to control the width the corona and to this aim, we apply an inward force with spherical symmetry inside the cavity.

We have considered two types of forces. The first type is described by the following expression:

$$\vec{f}_1 = \begin{cases} -kr\hat{r} & \text{if } 0 < r \leq C \\ -g\hat{r} & \text{if } C < r < Z, \end{cases} \quad (1.6)$$

where \hat{r} is a versor pointing outward. Here an elastic force with a coefficient k acts from the center up to the half radius of the cavity and a force of constant g is present for larger distances. We choose $C = \frac{Z}{2}$ as the point where the force

1.3 Tuning the crosslinker concentration in the polymer network

changes type in order to reproduce a core corona structure for the microgel. We verified that the shape of the resulting microgel is nearly the same for values of this point up to $3Z/5$. The second type of force smooths out the discontinuity at $Z/2$, increasing continuously from the center to the cavity boundary:

$$\vec{f}_2 = \begin{cases} - \left[\frac{m}{2} \exp\left(\frac{r-C}{t}\right) \right] \hat{r} & \text{if } 0 < r \leq C \\ - \left[m - \frac{m}{2} \exp\left(-\frac{r-C}{t}\right) \right] \hat{r} & \text{if } C < r < Z. \end{cases} \quad (1.7)$$

Here m, t determine the strength and the smoothness of the force, respectively. We use again $C = \frac{Z}{2}$.

Initially, we consider a force f of type f_1 with constant $g = 8 \times 10^{-3}$ and $k = 0$, shown in Fig. 1.5(b). One can observe that, although the corona becomes larger, the core is sparser for small r and denser close to the corona. This entails the emergence of a peak at $r \lesssim Z/2$ showing that crosslinkers tend to accumulate around this particular distance and their number decreases towards the center of core, which is not compatible with experimental findings for the class of microgels used in this study. Since the presence of a peak could be due to the discontinuity of f at $Z/2$, we have also employed a smooth force of type f_2 by Eq. (1.7). However, in this case, independently of the choice of the force parameters, the peak is not removed. The choice $m = 7 \times 10^{-3}$ and $t = 0.3$ provides a density profile very similar to the previous one (see Fig. 1.5(c)) for both monomers and crosslinkers. One can then conclude that the additional peak is not given by the discontinuity itself but it is a consequence of the weakness or absence of the force in the region $0 < r < Z/2$. Therefore, our next attempt is to maintain the corona shape of the previous examples and get rid of the peak. To this aim, we again employ a force of type f_1 with $g = 8 \times 10^{-3}$ and $k = \frac{2g_1}{Z} = 3.2 \times 10^{-4}$. The use of $k \neq 0$ corresponds to the application of an elastic force in the inner half region, Eq. (1.6) which is continuous at $Z/2$. Furthermore, we employ the same value of g as before in order to keep unchanged the shape of the corona. The resulting density profile is reported in Fig. 1.5(d). In this case, we notice that the density distribution inside the microgel is strongly altered, with a continuously decreasing density from the center to the cavity boundary. The absence of a core is totally different from experimental observations.

1.3 Tuning the crosslinker concentration in the polymer network

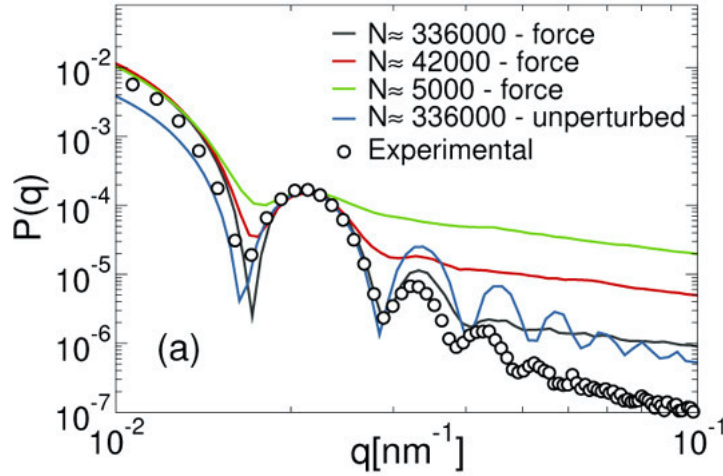


Figure 1.6: Microgel form factors as a function of the size. Size effects on the form factors of microgels for three system sizes obtained with the same designing force and in the unperturbed case in the swollen state ($\alpha = 0$). The data are compared with experimental measurements for $T = 15.6$ C (black circles) through the rescaling factors $\gamma_{336000} = 0.233$, $\gamma_{42000} = 0.124$, $\gamma_{5000} = 0.0580$ and $\gamma_{5000}^{unperturbed} = 0.274$.

We infer that this effect is a consequence of the intensity of the force for $r < Z/2$, and therefore we decide to decrease the spring constant of the force as sketched in Fig. 1.5(e), resulting in a discontinuity at $Z/2$. Using the value $k = 4.5 \times 10^{-5}$, we find a density distribution in the core in agreement with the experiments, while preserving the right shape of the corona. Interestingly, in this case, the crosslinker profile is continuously decreasing from the center of the microgel and does not reflect the total profile of all the monomers. This is the choice that we adopt in the following to reproduce the experimental results for all studied system sizes.

1.3.2 Size effects

The effect of the microgel size is evident in the behavior of the form factors $P(q)$ defined as

$$P(q) = \frac{1}{N} \sum_{ij} \langle \exp(-i\vec{q} \cdot \vec{r}_{ij}) \rangle, \quad (1.8)$$

where the angular brackets indicate an average over different equilibrium configurations of the same microgel and over different orientations of the wavevector q ,

1.3 Tuning the crosslinker concentration in the polymer network

and r_{ij} is the distance between monomers i and j . This quantity represents the low density limit of the static structure factor $S(q)$ and can be easily obtained in scattering experiments of dilute microgel suspensions [4, 5]. In this sense, they constitute the basis for a direct comparison between experiments and simulations, in terms of the shape and internal structure of the microgel particles.

The form factors are reported in Fig. 1.6, for the swollen state ($\alpha = 0$). The numerical data for different N are compared to the experimental form factor acquired via X-ray scattering experiments of microgels synthesized via the precipitation polymerization procedure; further experimental details can be found in Ref. [174]. The maximally swollen state in our model is set to be at the lowest measured temperature that is $T = 15.6^\circ\text{C}$. In order to perform the comparison, we match the position of the first peak q_{sim}^* of the numerical $P(q)$ onto that of the experiments q_{exp}^* . This procedure defines the scaling factor $\gamma = q_{\text{exp}}^*/q_{\text{sim}}^*$ that allows to convert numerical units into real ones. We observe that the first peak of $P(q)$ for the smallest system ($N \approx 5000$) is just barely visible, whereas it becomes better defined by increasing the microgel radius by a factor of ~ 2 ($N \approx 42000$), with the simultaneous appearance of a second peak. Finally, the largest system tested ($N \approx 336000$), corresponding to a further increase by a factor of ~ 2 in radius, reproduces quite well three out of the four peaks observed in the experimental curve. For all sizes, the relative distance between the peaks is maintained, but upon increasing N the high- q decay of $P(q)$ shifts further and further down, approaching the experimental curve. It is important to point out that the observed dependence on size for $P(q)$ is also present in real microgels of different sizes, with the peaks becoming shallower for small microgels. From the estimated values of γ for each simulated size, we get an effective size of the monomer bead, amounting to ≈ 4 nm for the largest microgel. We stress that in order to reach a realistic value of the PNIPAM monomer size $\sigma \sim 1$ nm [147], we should increase the number of monomers up to $N \approx 2 \times 10^7$, which is unfeasible with present day computational techniques. Such a discrepancy in size between simulated and experimental microgels thus explains the high- q deviations of the numerical form factors observed in Fig. 1.6. In addition, the numerical form factors at large wave-vectors can be well-described by an inverse power law, $P(q) \approx q^{-n}$, with

1.3 Tuning the crosslinker concentration in the polymer network

$n \sim 1$ for all investigated cases. The fact that n does not vary with system size suggests that microgels with different N possess the same topological structure,

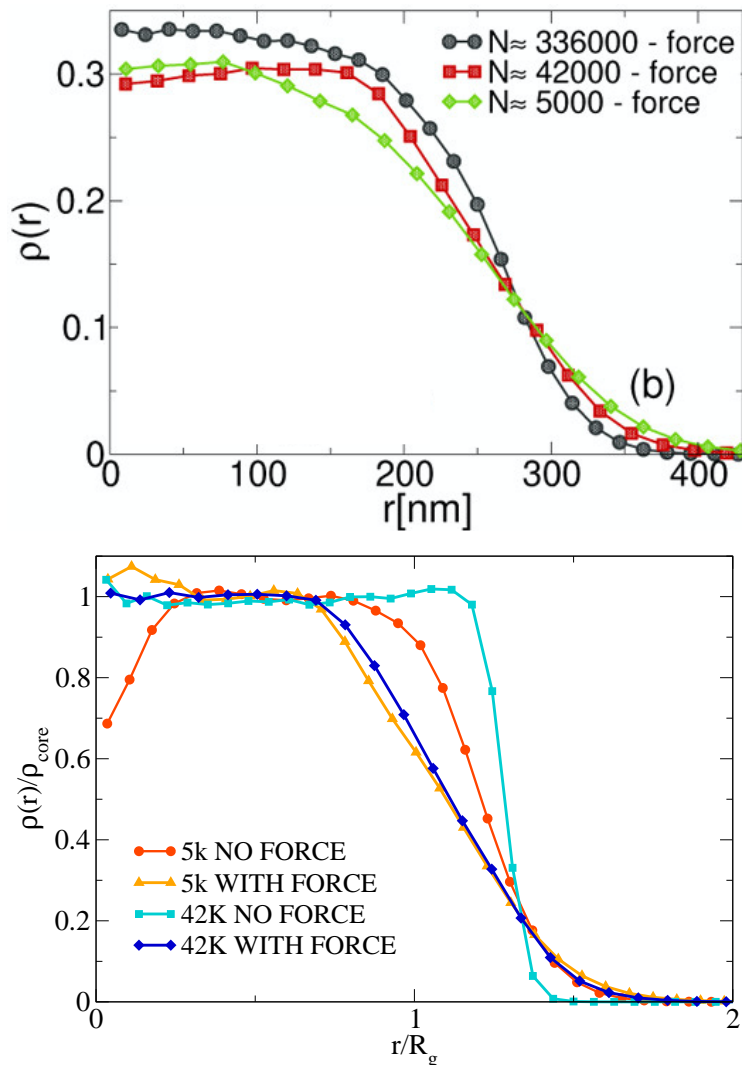


Figure 1.7: Density profiles as a function of the size. Top: Size effects on the density profiles of microgels for three system sizes obtained with the same designing force in the swollen state ($\alpha = 0$). Data are scaled on the x -axis by $1/\gamma$ for the corresponding size. Bottom: radial density profiles $\rho(r)$, normalized on the Y -axis by the core average density ρ_{core} and on the x -axis by the radius of gyration R_g , for four different microgels: (red circles) microgel with ≈ 5000 monomers prepared without additional designing force (averaged over 3 different topologies); (orange triangles) microgel with ≈ 5000 monomers prepared with additional designing force (averaged over 3 different topologies); (turquoise squares) a large microgel with ≈ 42000 monomers prepared without additional designing force (averaged over 10 different topologies); (blue diamonds) a large microgel with ≈ 42000 monomers prepared with the additional designing force (averaged over 10 different topologies). Deviations from a flat profile in the core region are due to the limited number of independent topologies employed for this analysis.

1.3 Tuning the crosslinker concentration in the polymer network

at least on a mesoscopic scale. Finally, we notice that $P(q)$ of the unperturbed microgel also shown in Fig. 1.6 presents numerous peaks in agreement with a homogenous dense spherical system, deviating from the experimental findings for both the relative position of the peaks and for the shape of the curve at small q .

To better visualize and quantify the differences between the various system sizes, we report in Fig. 1.7 the density profiles of the three different systems as well as the corresponding snapshots in Fig. 1.8. The radial density profiles are numerically defined as

$$\rho(r) = \left\langle \frac{1}{N} \sum_{i=1}^N \delta(|\vec{r}_i - \vec{r}_{CM}| - r) \right\rangle. \quad (1.9)$$

As expected, the surface contributions are found to dominate for small-sized microgels of a few thousands monomers, while they become less and less relevant when increasing N . In all cases, the corona behavior is rather similar, while the core becomes more and more structured only for larger microgels. This result is the counterpart in real space of the stronger pronunciation of the peaks of $P(q)$ with increasing microgel size.

Finally, it is interesting to compare the density profiles obtained by adding the force on the crosslinkers and in the unperturbed case by changing microgel size. This comparison is shown in Fig. 1.7 at the bottom, which reports a normalized

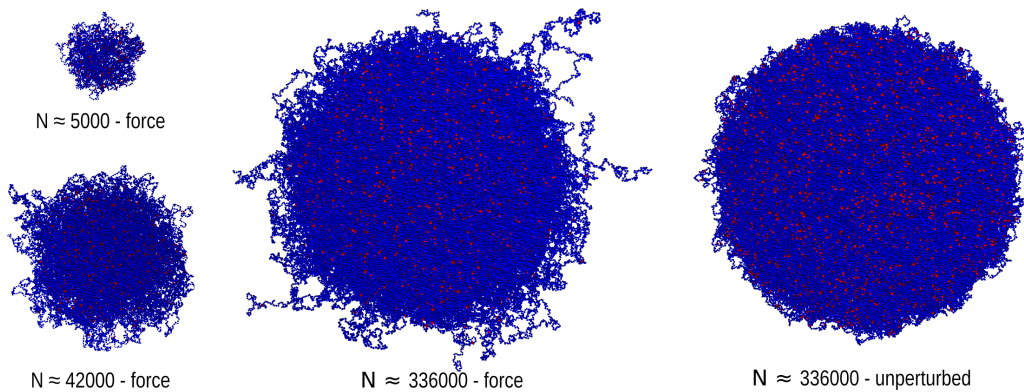


Figure 1.8: Simulation snapshots as a function of the microgel size. Simulation snapshots are reported for the three sizes investigated here with the designing force and in the unperturbed case. Blue particles represent monomers while red particle represent the crosslinkers.

1.3 Tuning the crosslinker concentration in the polymer network

density profile as a function of the distance from the microgel center of mass, rescaled by the characteristic size of the particle. It is evident how by increasing the microgel size from $N \approx 5000$ to $N \approx 42000$ the density profile tends towards a step-like shape. However, by adding the same designing force on the crosslinkers, the profiles are essentially superimposed one each other with a homogeneous core smoothly decaying towards the corona.

Overall, changing system size, we observe small differences in the density profiles (also due to statistics) and more pronounced ones in the form factors. These are the consequences of the fact that the surface-to-volume contributions play a different role on the final assembled structures. Notwithstanding this, our protocol is now able to generate microgels with a similar topology and core-corona ratio independently of size and we will further show below that, thanks to this, the comparison with experiments does not depend quantitatively, but only qualitatively, on N . Consequently, the system size becomes a parameter that can be optimised in order to reproduce the properties of interest while, at the same time, reducing the computational effort.

1.3.3 Comparison with the experiments for different temperatures across the Volume Phase Transition

In the previous Section, numerical and experimental form factors have been compared in swollen conditions. In this Section, we start by comparing the form factors for the largest studied microgels with $N \approx 336000$ for different temperatures across the VPT. Numerically, we make use of V_α (Eq. 1.4) to mimic the effect of temperature.

As shown in Fig. 1.9, the agreement between experiments and simulations is remarkably good at all T , up to the second peak. The fact that the numerical data present peaks that are sharper and deeper could be explained by the presence of a weak polydispersity in the experimental data, that is not considered in the simulations. Most importantly, the positions of all the visible peaks in the simulations are found to coincide with those in experiments. At high T , where the microgel collapses and becomes more homogeneous, the agreement improves even further, with the numerical data being able to capture the positions and

1.3 Tuning the crosslinker concentration in the polymer network

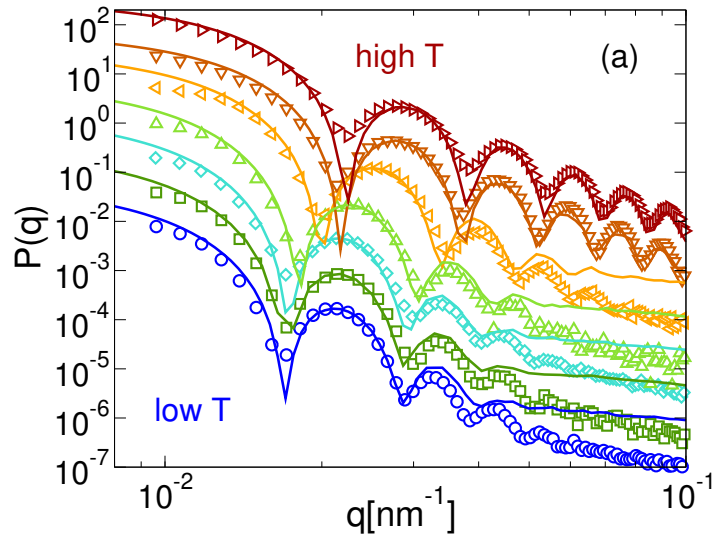


Figure 1.9: Form factors as a function of the temperature for big microgels. Comparison between experimental (empty symbols) and numerical (Eq. (1.8), full lines) form factors for $N \approx 336000$. The x -axis is rescaled by $\gamma = q_{\text{exp}}^*/q_{\text{sim}}^* = 0.2326$, where q^* is the position of the first peak of $P(q)$. Different colors correspond to different temperatures T and solvophobic parameters α , increasing from bottom to top: $T = 15.6, 20.1, 21.6, 25.4, 31.0, 35.4, 40.4\text{C}$ in experiments and $\alpha = 0.00, 0.05, 0.10, 0.30, 0.56, 0.74, 0.80$ in simulations. Data at different T, α are rescaled on the y -axis with respect to the lowest temperature in order to help visualization.

heights of all measured peaks. We notice that the deviations occurring at large q are entirely attributable to the smaller size of the numerical microgels as compared to the laboratory ones, as discussed in the previous section, leading to a different structure at very short length-scales.

We stress that the comparison in Fig. 1.9 is obtained with the same value of the scaling factor γ obtained for $\alpha = 0$, that is maintained for all temperatures. However, we adjust the value of the solvophobic interaction strength α in order to capture the T -variation of $P(q)$. The resulting relationship between α and T is illustrated in Fig. 1.10. We find that an approximately linear dependence holds at intermediate temperatures, showing some deviations at low and high T . While the former may be due to the arbitrary choice of the $\alpha = 0$ value with the lowest available T , the latter is more likely related to the implicit nature of the solvent employed in the simulations. These results also confirm the appropriateness of the V_α potential, here tested for the first time against experiments across the VPT.

To validate the size independence of our model and the robustness of the (T, α) mapping to describe the deswelling transition of the microgels, we further

1.3 Tuning the crosslinker concentration in the polymer network

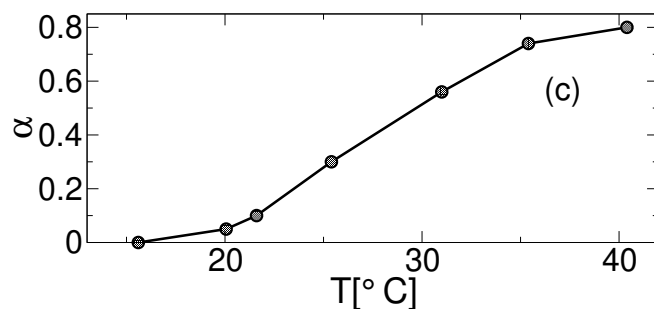


Figure 1.10: Mapping between temperature and α .

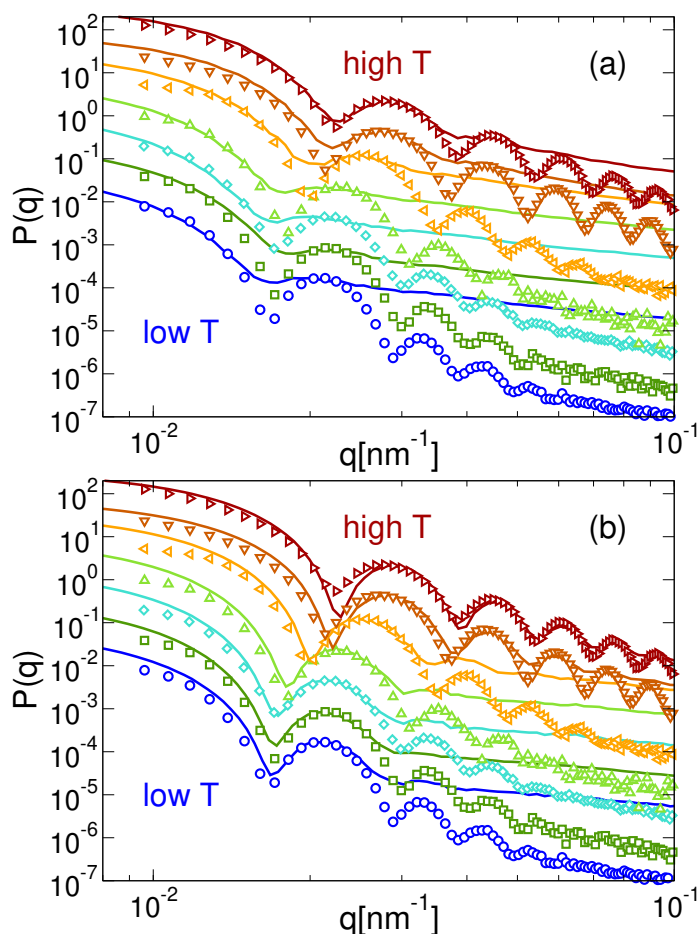


Figure 1.11: Form factors as a function of the temperature for smaller microgels. Comparison between experimental (empty symbols) and numerical (Eq. (1.8), full lines) form factors for (a) $N \approx 5000$ and (b) $N \approx 42000$. The x -axis is rescaled by $\gamma_{5000} = 0.0580$ and $\gamma_{42000} = 0.124$, respectively. Different colors correspond to different temperatures T and solvophobic parameters α , increasing from bottom to top: $T = 15.6, 20.1, 21.6, 25.4, 31.0, 35.4, 40.4^\circ\text{C}$ in experiments and $\alpha = 0.00, 0.05, 0.10, 0.30, 0.56, 0.74, 0.80$ in simulations. These are the same values used for the case $N \approx 336000$. Data at different (T, α) are rescaled on the y -axis to help visualization.

1.3 Tuning the crosslinker concentration in the polymer network

compare the experimental form factors with those calculated from simulations of different system sizes using the same α values for all N . Again, we keep constant the scaling factors γ , that we determined for $\alpha = 0$. The comparisons are shown in Fig. 1.11 for the small and intermediate size systems. We employ as well the same procedure to rescale the numerical data on the experimental ones: we define a conversion factor $\gamma_{5000} = 0.05798$ and $\gamma_{42000} = 0.1245$ to superimpose the experimental and numerical first peak of $P(q)$ respectively for the small and the medium size systems. These two values are used to rescale the q -axis of numerical form factors for all of α s investigated. Strikingly, we find that the swelling behavior is well captured using each system size. The peaks are indeed found in the position corresponding to those of the experimental curves, even though they are barely visible, especially for the smallest studied system. The high- q deviations between experiments and simulations become more evident as N decreases, but the agreement improves at high T . From these results, we can conclude that the relationship between T and α , shown in Fig. 1.10 is unaffected by size effects. Thus, even though smaller systems give rise to a worse q -space resolution, a size-independent swelling behavior is found for all studied N , confirming the reliability of our procedure in reproducing experimental results.

In order to directly visualize the internal structure of the microgel, we move to real space. To obtain the experimental radial density distributions from the scattering data, we need to fit the measured form factors. This is usually done by means of the fuzzy sphere model, which consider the microgel as a homogeneous sphere with a smeared particle surface to account for the "fuzziness" of the outer shell in the polymer network. However, building on the evidence from recent super-resolution microscopy experiments [173], we employ an extended fuzzy sphere model that is represented by an error function multiplied by a linear term

$$\rho(r) \propto \text{Erfc} \left[\frac{r - R'}{\sqrt{2}\sigma_{\text{surf}}} \right] (1 - sr), \quad (1.10)$$

where R' corresponds to the radius at which the profile has decreased to half the core density, σ_{surf} quantifies the width of the corona and s is the slope of the linear decay. As compared to the standard fuzzy sphere model, which is recovered for

1.3 Tuning the crosslinker concentration in the polymer network

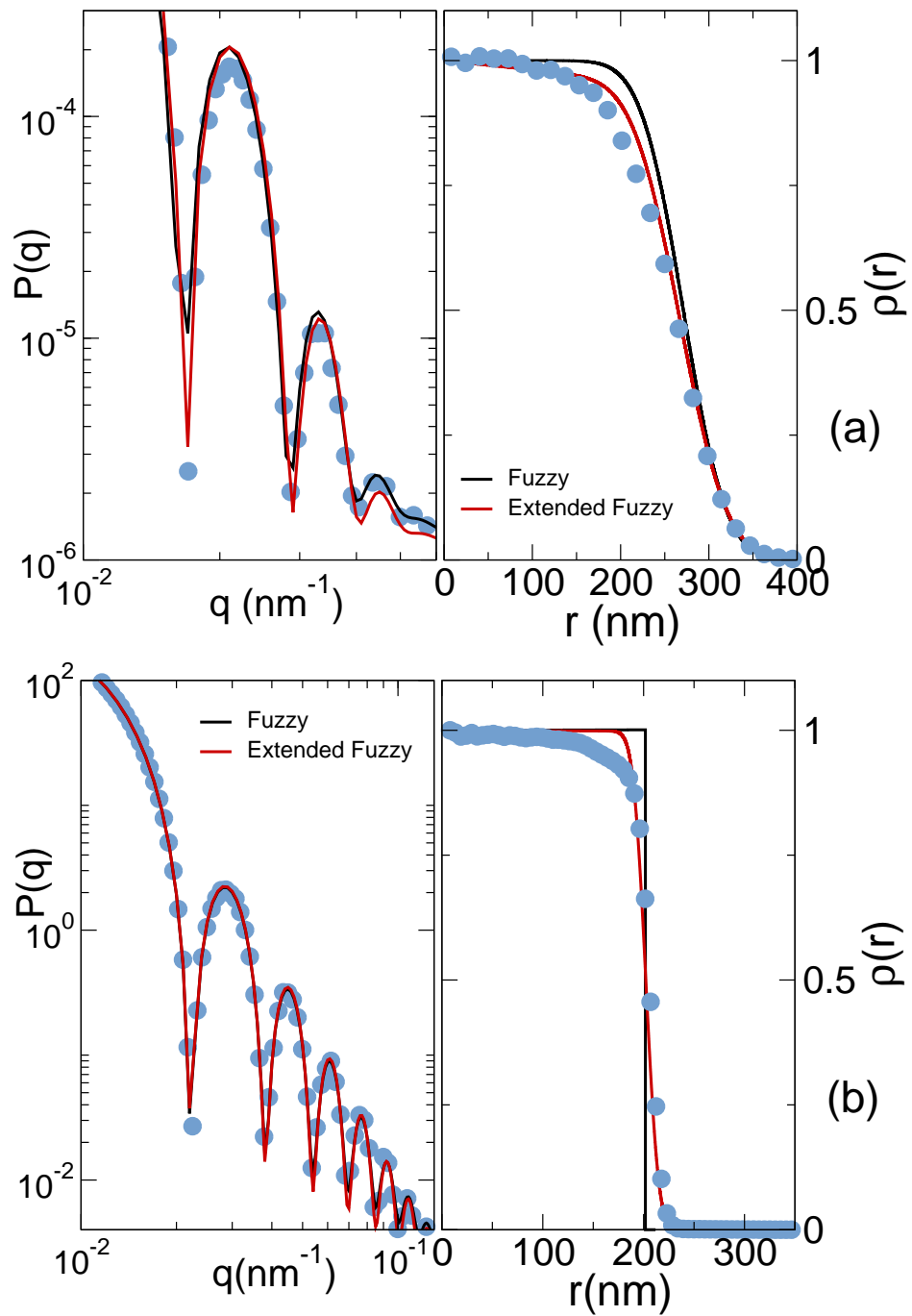


Figure 1.12: Comparison of the standard and extended fuzzy sphere models. Form factors and density profiles for the standard (black) and generalized (red) fuzzy sphere models with the numerical results (blue symbols) for (a) $T = 15.4^\circ\text{C}$ and (b) $T = 40.4^\circ\text{C}$. The density profiles are rescaled to 1 at $x = 0$ for clarity.

$s = 0$, it includes a linear growth of the monomer density inside the core of the microgel. In this way, the expression in Fourier space for the form factor reads

1.3 Tuning the crosslinker concentration in the polymer network

$$P(q) \propto \left\{ \left[\frac{3(\sin(qR) - qR \cos(qR))}{(qR)^3} + s \left(\frac{\cos(qR)}{q^2 R} - \frac{2 \sin(qR)}{q^3 R^2} - \frac{\cos(qR) - 1}{q^4 R^3} \right) \right] \times \exp \left[-\frac{(\sigma q)^2}{2} \right] \right\}^2. \quad (1.11)$$

We also calculate $\rho(r)$ directly from simulations and then convert them to real units by consistently rescaling the x -axis by $1/\gamma$.

We show the comparison between numerical data and the corresponding ones extracted from the fits in Fig. 1.12 for two representative temperatures, respectively in the swollen (a) and collapsed (b) regimes. We stress that the use of the standard fuzzy sphere model with a homogeneous core to fit the experimental $P(q)$ not only is at odds with super-resolution data [173], but also yields density profiles that are in worse agreement with numerical data, as shown in Fig. 1.12. Indeed, the generalized fuzzy sphere model agrees very well with the numerical data both in the inner part of the core and in the corona. For intermediate values of r there are some small deviations, mainly due to the non-linear decrease of the density profile. On the other hand, the standard fuzzy sphere model shows

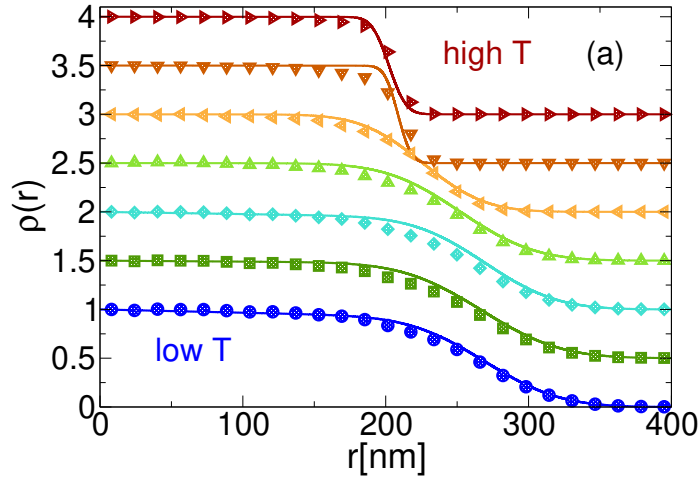


Figure 1.13: Microgel density profiles as a function of the temperature. Numerical (full symbols) and experimental (full lines) density profiles $\rho(r)$, where the latter are obtained by fitting the form factors to the generalized fuzzy sphere model (Eq. (1.10)). The numerical x -axis is rescaled by γ^{-1} , while data are normalized to 1 at the center of the microgel and shifted vertically by 0.5 at different T to improve readability.

a weaker agreement with the calculated profile, especially due to the presence of the completely homogeneous core. The disagreement becomes more evident at high T where the standard fuzzy sphere results show a step-like behavior. Instead, a continuously decreasing profile is still observed in simulations and for the generalized fuzzy sphere model, again in close agreement to each other. The quality of the extended fuzzy sphere fits to $P(q)$ is rather good. From the fits, we estimate the linear correction s to be always quite small, $s < 5 \times 10^{-4} \text{nm}^{-1}$. Most importantly, we find small but finite values of σ_{surf} also above the VPT, which is consistent with the fact that, even in the collapsed state, the microgels still contain a large amount of water [46].

A summarizing comparison between numerical and experimental density profiles is reported in Fig. 1.13 for all studied temperatures. The agreement is again found to be very good throughout the whole T range for both the core and the corona regions.

1.4 Summary

In this Chapter, we have shown how computer simulations can realistically model thermoresponsive microgels. In particular, we adopt a designing force during the network assembly which can be tuned to quantitatively reproduce experimental form factors for a wide range of temperatures across the VPT. Even if the protocol itself is not meant to reproduce the experimental conditions of the synthesis, it is nevertheless able to generate networks with topologies that can closely match experimental data.

We have shown that our method is robust to system size for swelling properties and it reproduces very well the experimental form factors, with the agreement improving with the size of the microgels. It is worthwhile to note that the comparison is good even for microgels composed of only a few thousands monomers, which can be routinely studied in simulations. This allows us to establish a relationship between the solvophobic strength α used in simulations and the experimental temperature T , finding that they are linearly related across the VPT, as expected. Such a relation is found to hold for all studied system sizes.

The main References for this Chapter are:

- N. Gnan, L. Rovigatti, M. Bergman, E. Zaccarelli, *In silico* synthesis of microgel colloids, *Macromolecules* **50**, 8777-8786 (2017)
- A. Ninarello, J. J. Crassous, D. Paloli, F. Camerin, N. Gnan, L. Rovigatti, P. Schurtenberger, E. Zaccarelli, Modeling microgels with a controlled structure across the volume phase transition, *Macromolecules* **52**, 7584-7592 (2019)

Chapter 2

Modeling microgels in an explicit solvent

In order to reproduce the swelling behavior, it is possible to incorporate in the model an attractive potential that has been shown to capture the variation in polymer-solvent interactions upon changing temperature. With this approach, the solvent is implicit and the solvophobic potential V_α accounts for it within the thermodynamic properties of the system in an effective way. As reported in the previous Chapter, this implicit solvent model was shown to be able to faithfully reproduce the structural features of individual laboratory microgels [174]. On the other hand, it is also possible to perform simulations with an explicit solvent which implies, in the context of coarse-grained simulations, the explicit insertion of coarse-grained solvent particles in the simulation box. Even though the use of an explicit versus an implicit solvent model [175, 176] should give identical results in terms of equilibrium properties, there are a number of features that cannot be correctly captured and/or described by an implicit model. In particular, the kinetics of swelling and deswelling could depend on the presence of the solvent and on how it is modelled. Besides that, there are situations of fundamental and practical interest in which an explicit solvent will dramatically affect the picture. Among all, the modeling of a system at a liquid-liquid interface, which is central to this Thesis, necessarily requires to take into account the presence of the two different media in order to capture effects related to the surface tension [151, 177].

In order to be able to handle these situations, in this Chapter we develop an explicit solvent description that accurately predicts the properties of microgel particles across the Volume Phase Transition. After having analyzed different models of explicit solvent, we compare the swelling ratio as a function of temperature and the microgel density profile and form factor with and without solvent and we are able to discriminate and choose the explicit description that works best. In particular, we intend to model a generic solvent that ensures that the key properties of microgel colloids are accurately reproduced rather than to provide a systematic and exhaustive study on the influence of the system parameters on the properties of the particle. We further test the robustness of our approach by repeating the analysis for microgels generated with a different topology and confinement radius. Once the explicit model is established, we first analyze the arrangement of the solvent inside the microgel at different effective temperatures, and then study the kinetics of deswelling.

2.1 Different models of explicit solvent

In this Chapter, the explicit inclusion of the solvent in the simulations is studied following two approaches: either through soft particles with an excluded volume or through particles whose interaction potential goes to zero for small distances, also called bounded potential. Both of them have been used in simulations of polymeric systems in explicit solvent [149, 178, 179].

The typical *solvent-solvent* interaction that is employed in the former case is that of the standard Lennard-Jones (LJ) potential

$$V_{LJ}(r) = 4\epsilon \left[\left(\frac{\sigma}{r} \right)^{12} - \left(\frac{\sigma}{r} \right)^6 \right] \quad (2.1)$$

with the notation being the same as for the WCA potential employed in the monomer-monomer interactions in Eq. 1.1. Here, this is used for solvent densities $0.729 \leq \rho_s \leq 0.845$ for which the LJ solvent is in the fluid regime [180]. The choice of the solvent density also allows to tune the pressure exerted by the solvent on

2.1 Different models of explicit solvent

the polymer network thus determining the swelling range of the microgel particle, as discussed below.

The choice of the *monomer-solvent* (ms) interactions, instead, is crucial in order to implement the solvophobic effect, giving rise to the VPT of the microgel. These interactions control in fact the contraction or extension of the polymers chains in the solvent environment. In this respect, we test different approaches. Our first choice is to employ again the LJ potential in which its depth $\epsilon_{\text{ms}} (\equiv \epsilon)$ is varied, so that the attractive contribution can be tuned. A weaker attraction would give rise to a more repulsive monomer-solvent interaction that should cause the shrinking of the microgel.

We also consider a λ -dependent Lennard-Jones potential [181], $V_\lambda(r)$, defined as:

$$V_\lambda(r) = \begin{cases} V_{WCA} - \epsilon\lambda & \text{if } r \leq 2^{\frac{1}{6}}\sigma \\ 4\epsilon\lambda \left[\left(\frac{\sigma}{r}\right)^{12} - \left(\frac{\sigma}{r}\right)^6 \right] & \text{otherwise} \end{cases} \quad (2.2)$$

λ plays the role of an inverse temperature (analogue to the inverse of α in the implicit solvent potential V_α). For large values of λ there is an attractive contribution between a monomer and a solvent particle, mimicking good solvent conditions, while for $\lambda = 0$, the WCA potential is recovered and monomer-solvent interactions are purely repulsive. The potential is truncated and shifted at 2.5σ . Remarkably, the advantage of using such a potential with respect to the simple LJ interactions is that it allows to alter the monomer-solvent interactions, and thus the “quality” of the solvent, without affecting the excluded-volume part; this remains encoded in the V_{WCA} term and it does not depend on λ .

Finally, soft bounded potentials for an explicit solvent treatment are mainly represented by DPD, which is a mesoscale simulation technique [182, 183] that treats solvent particles as coarse-grained beads and is able to describe hydrodynamic interactions through a momentum-conserving thermostat. In DPD simulations, particles i and j interact by three pairwise additive forces: a conservative force \vec{F}_{ij}^C , a dissipative force \vec{F}_{ij}^D and a random force \vec{F}_{ij}^R where

$$\vec{F}_{ij}^C = \begin{cases} a_{ij}(1 - r_{ij}/r_c)\hat{r}_{ij} & \text{if } r_{ij} < r_c, \\ 0 & \text{otherwise} \end{cases}; \quad (2.3)$$

$$\vec{F}_{ij}^D = -\gamma w^D(r_{ij})(\hat{r}_{ij} \cdot \vec{v}_{ij})\hat{r}_{ij}; \quad (2.4)$$

$$\vec{F}_{ij}^R = \sigma_R w^R(r_{ij})\theta(\Delta t)^{-1/2}\hat{r}_{ij}. \quad (2.5)$$

Here $\vec{r}_{ij} = \vec{r}_i - \vec{r}_j$ with \vec{r}_i the position of particle i , $r_{ij} = |\vec{r}_{ij}|$, $\hat{r}_{ij} = \vec{r}_{ij}/r_{ij}$, $\vec{v}_{ij} = \vec{v}_i - \vec{v}_j$ with \vec{v}_i the velocity of particle i , $w^D(r_{ij})$ and $w^R(r_{ij})$ are weight functions, θ is a Gaussian random number with zero mean and unit variance and γ is the friction coefficient (here $\gamma = 4.0$); to ensure that the correct Boltzmann distribution is achieved at equilibrium, $w^D(r_{ij}) = [w^R(r_{ij})]^2$ and $\sigma_R^2 = 2\gamma k_B T$ [184]. The interaction region for the dissipative force is defined in the same way as for the conservative force, *i.e.* $w^D(r_{ij}) = 1 - r_{ij}/r_c$. R_c is the DPD cut-off radius and effectively determine the size of the DPD beads. A specific choice of the cut-off radius and of the interaction parameters allows to establish a mapping to real molecular systems (see Chapter 3).

Here, we fix the solvent number density at $\rho = 0.73$ and we tune the interaction parameters and the radius of the solvent beads until the swelling curve of the implicit solvent model is reproduced, in this case at $r_c = 1.75\sigma$. The same curve may be found by using different combination of these parameters in the limit in which the size of the solvent bead is comparable with that of the microgel monomer. The monomer-solvent interaction parameters a_{ij}^{ms} , that for simplicity we call a_{ms} , plays the role of an effective temperature and, depending on its value, controls the volume phase transition of the polymer network. The repulsion coefficient for solvent-solvent interactions is fixed at $a_{ij}^{\text{ss}}\sigma = a_{\text{ss}}\sigma = 25\epsilon$.

2.2 Swelling behavior

We start by discussing the swelling behavior of microgels in the presence of an explicit solvent as compared to the reference case of the implicit model V_α , Fig. 2.1(a), discussed in Ref. [143] and in the previous Chapter. To this aim, we

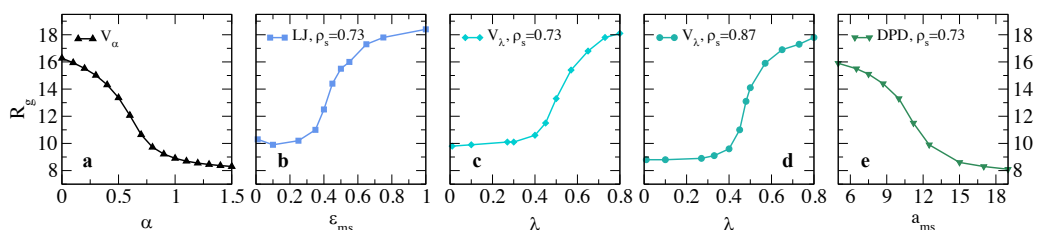


Figure 2.1: Microgel swelling curves. Radius of gyration R_g across the VPT transition for (a) the implicit model, V_α ; (b) the explicit LJ solvent with LJ monomer-solvent interactions at a solvent density $\rho_s = 0.729$; (c,d) explicit solvent with V_λ monomer-solvent interactions at $\rho_s = 0.729$ and $\rho_s = 0.875$, respectively; (e) DPD simulations where the microgel is modeled as a bead-spring polymer network. All curves report the gyration radius R_g as a function of the parameter controlling the solvophobic interactions in each model: (a) α , (b) ϵ_{ms} , (c-d) λ and (e) a_{ms} .

perform simulations of an individual microgel assembled with a rather loose topology (using a confining radius $Z = 25\sigma$) in different solvents.

Similarly to solvent-solvent interactions, a straightforward choice for the monomer-solvent ones is the LJ potential [179] where, by varying the energy minimum ϵ_{ms} , we control the polymer-solvent affinity. In this way, we obtain the swelling curve reported in Figure 2.1(b), where the radius of gyration of the microgel R_g is shown as a function of ϵ_{ms} : by decreasing this parameter (with respect to solvent-solvent interaction, which sets the energy scale), the polymer-solvent interactions are less favoured than solvent-solvent ones, giving rise to a reduction of the microgel size. However, an unphysical increase of R_g is observed for $\epsilon_{ms} \rightarrow 0$: under this condition, both terms in the LJ potential go to zero, *i.e.* the microgel feels neither attraction nor repulsion with the solvent. Consequently, the network relaxes as the external pressure on the polymer network vanishes, and the microgel swells again, maximizing its configurational entropy.

Such behaviour clearly indicates the unsuitability of the LJ potential to mimic the solvent-monomer interactions. Consequently, the next step is to use a potential in which the attractive term can be tuned arbitrarily without affecting the short-range repulsion. To this aim, we adopt the V_λ model, defined in Eq. (2.2), where the repulsion remains unchanged while the attractive contribution, controlled by the parameter λ , is varied. The swelling behavior of the microgel obtained with this model is reported in Fig. 2.1(c,d) for two representative solvent densities. The swollen-to-collapsed transition is well reproduced in both cases.

So far, we have assessed the hard-core-like solvents. We further examine the possibility to use a coarse-grained solvent by means of DPD simulations. In order to establish a meaningful comparison with the implicit solvent case and avoid unphysical crossing of the chains, we retain the bead-spring model for monomer-monomer interactions and we apply the DPD treatment only to monomer-solvent and solvent-solvent interactions.

The results of DPD simulations, for the parameters specified in Section 2.1, are reported in Fig. 2.1(e). In this case, the VPT transition is modulated by the monomer-solvent repulsion quantified by the parameter a_{ms} in Eq. (2.3): for small values of a_{ms} the microgel is swollen, while it contracts when a_{ms} increases. We notice that R_g is systematically larger at comparable swelling for MD-solvents than for DPD results, which, on the other hand, quantitatively reproduce the values obtained in the implicit solvent description. This is due to the softness of the DPD interactions which, contrarily to the MD treatment, do not introduce significant solvent-monomer excluded volume effects, thereby not affecting the microgel size.

In order to establish a correspondence between different models, we rescale the explicit solvent data onto the implicit one, V_α . For those explicit solvent models where a small value of the swelling parameter corresponds to a collapsed state of the microgel, *i.e.* V_{LJ} and V_λ , the scale has to be inverted. In order to properly rescale the x axes onto each other for two curves A and B , we consider two points on the first (x_1^A and x_2^A) and on the second curve (x_1^B and x_2^B), respectively. The rescaled x -coordinate is calculated using the following relationship: $x_{\text{new}} = (x - \langle x^A \rangle) \Delta x^B / \Delta x^A + \langle x^B \rangle$, where $\langle x^i \rangle = 0.5(x_1^i + x_2^i)$ and $\Delta x^i = x_1^i - x_2^i$ with $i = A, B$. Figure 2.2(a) shows the normalized R_g/R_g^{max} , where R_g^{max} is the value of the gyration radius at maximum swelling, as a function of the effective swelling parameter χ_{eff} , which effectively corresponds to the solvophobic parameter α of the implicit solvent simulations.

We report the comparison for the two cases where the agreement is found to be fully satisfactory for all χ_{eff} , namely the DPD and MD V_λ models. Of the latter, we consider only the case with the highest solvent density, $\rho = 0.87$, since deviations with respect to the implicit solvent case are observed with lower densities: the

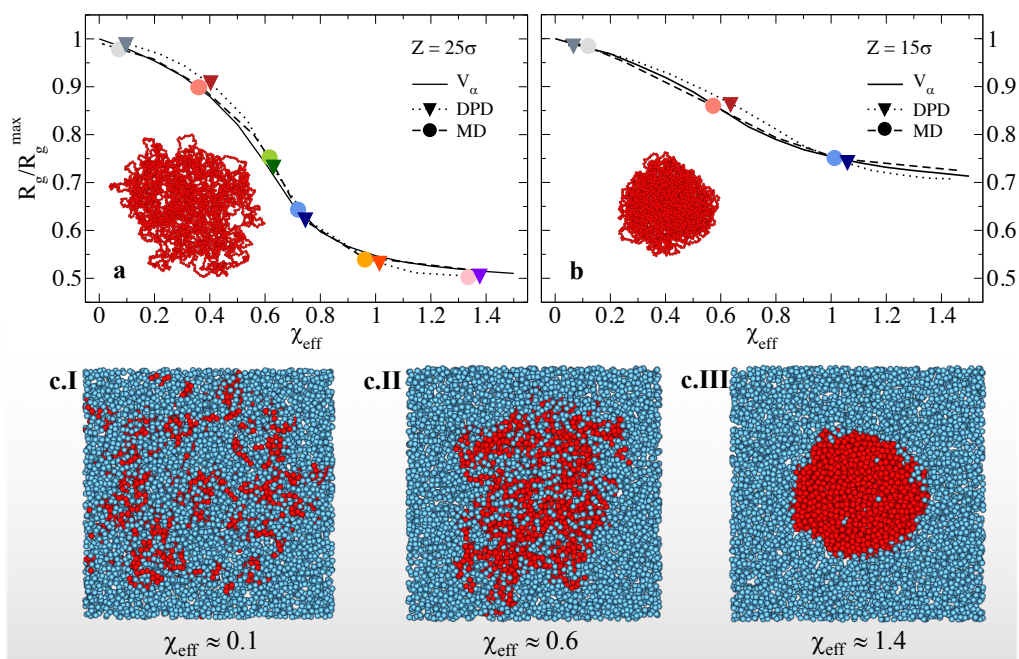


Figure 2.2: Effect of microgel topology and solvent arrangement. Swelling curves for the implicit- (full line) and explicit-solvent models that best reproduce the swelling behavior, namely MD simulations with V_λ at $\rho = 0.87$ (dashed lines) and DPD simulations (dotted lines) for (a) a loose microgel ($Z = 25\sigma$) and (b) a more compact microgel ($Z = 15\sigma$). Corresponding microgel snapshots are also shown. Symbols refer to state points in explicit solvent simulations (MD: circles, DPD: triangles) for which further analysis is provided in the next sections, whereas similar colors/shapes refer to similar swelling degrees between the two explicit solvent models. Panels (c.I-c.III) display a central slab of the simulation box for three different values of χ_{eff} , respectively corresponding to the swollen state (c.I), a state very close to the VPT (c.II) and the collapsed state (c.III). The arrangement of solvent (blue spheres) within/around the polymer network (red spheres) depends on χ_{eff} . For visual clarity, only half of the solvent particles are shown.

swelling range of the microgel would be shortened, as can be observed in Figure 2.1(c). Thus, it appears that, while V_λ is definitely superior to the simple LJ potential to model the VPT of the microgel, the density of the solvent particles is a key parameter in tuning the details of the transition: a lower density will have a smaller effect on the microgel, resulting in a more limited contraction with respect to the implicit solvent model. From now on we will discard the LJ potential and we will refer to MD simulations as those performed with the V_λ interaction. A similar effect can be obtained in DPD simulations by changing the cutoff radius and the interaction parameters of the conservative force, which represents the length scale in DPD and the size of the solvent beads.

To verify the robustness of our protocol, we now repeat the above analysis on a microgel configuration assembled with a smaller confinement radius, $Z = 15\sigma$. Fig. 2.2(b) reports the swelling behaviour of the more compact microgel for the DPD and MD models at the optimal solvent density identified above. Together with the data, we also report snapshots of the two microgels (insets) in their maximally swollen state, showcasing the very different topology of the networks. The good agreement between the rescaled swelling curves for both studied microgel configurations allows us to conclude that the developed models are robust and both can faithfully reproduce the swelling behavior observed with the implicit model [143]. Fig. 2.2(c.I-c.III) further highlights the arrangement of solvent particles inside the microgel for MD simulations at different values of χ_{eff} across the VPT. The microgel remains very permeable to the solvent even close to the transition temperature, finally expelling it only in the fully compact state.

In the next Sections, we focus on MD and DPD to study the effects of the solvent on the microgel structural features and on the kinetics of the volume phase transition.

2.3 Structural features in an explicit solvent

2.3.1 Results for a loose microgel configuration

We now discuss the structural features of the microgel at relatively large confinement, corresponding to the swelling curve in Fig. 2.2(a). First, we show results for the density profile of the microgel in Fig. 2.3, for several values of the swelling parameter across the VPT for both MD and DPD simulations. We find that, in general, both solvent models yield density profiles that are very similar to the implicit solvent case. This is particularly true for the swollen states, where the typical core-corona structure of the microgels is clearly distinguishable. Under these conditions, DPD simulations are even more accurate than MD ones in reproducing the results of the implicit model. When χ_{eff} increases and the microgel becomes more compact, the difference between the three models becomes more evident. Specifically, as the microgel collapses MD simulations produces lower

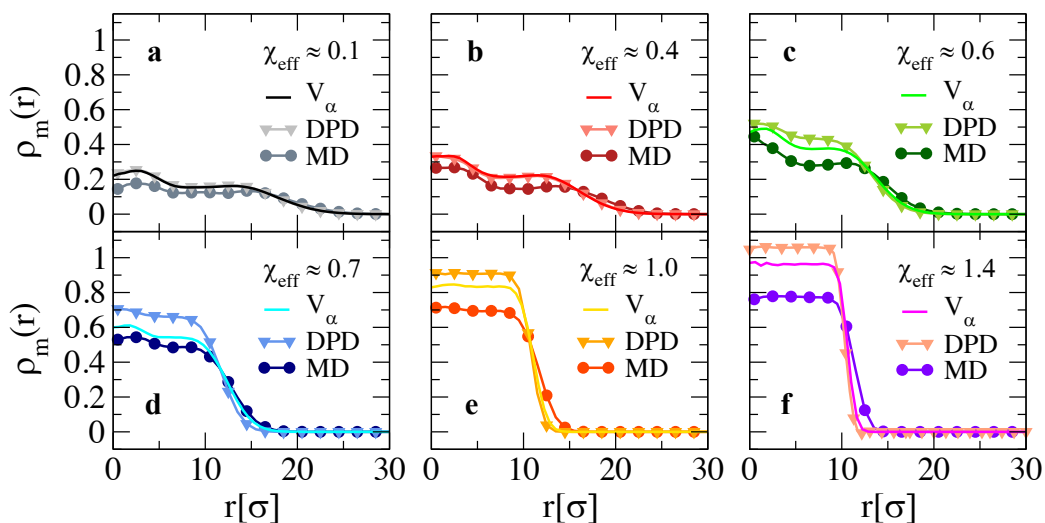


Figure 2.3: Density profiles for a loose microgel configuration across the VPT. Monomer radial density profile $\rho_m(r)$ for a $Z = 25\sigma$ microgel as a function of the distance r from its center of mass. Full lines refer to the implicit-solvent model, while symbols are used for MD (circles) and DPD (triangles) simulations. Each sub-panel refers to a different swelling state as in Fig. 2.2(a).

density profiles in the core region with respect to the implicit-solvent case at the same χ_{eff} , while the DPD model generates more compact structures.

We notice that low density profiles exhibit a non-flat behavior in the inner core region of the microgel. These inhomogeneities, that are stronger for smaller microgels, can be removed out by averaging over independent topologies [143]. Here we do not perform such an average because we aim to compare the behavior of a given microgel configuration with and without solvent. Beyond the VPT the oscillations are suppressed by the higher density, and hence the profiles are much flatter within the core.

While density profiles provide real-space information on the microgel structure, they are not easily accessible in experiments, except for very recent super-resolution microscopy investigations [153, 173]. Thus, in contrast to density profiles, numerical $P(q)$ can be used to make a direct comparison with experiments, without having to rely on fits to specific models. We thus directly evaluate the form factors of the microgel across the VPT calculated via Eq. 1.8. These are presented in Fig. 2.4 as a function of wavevector q for the same values of swelling parameters used in Fig. 2.3. We find that the use of an explicit solvent does not considerably alter the form factors with respect to the implicit solvent case for

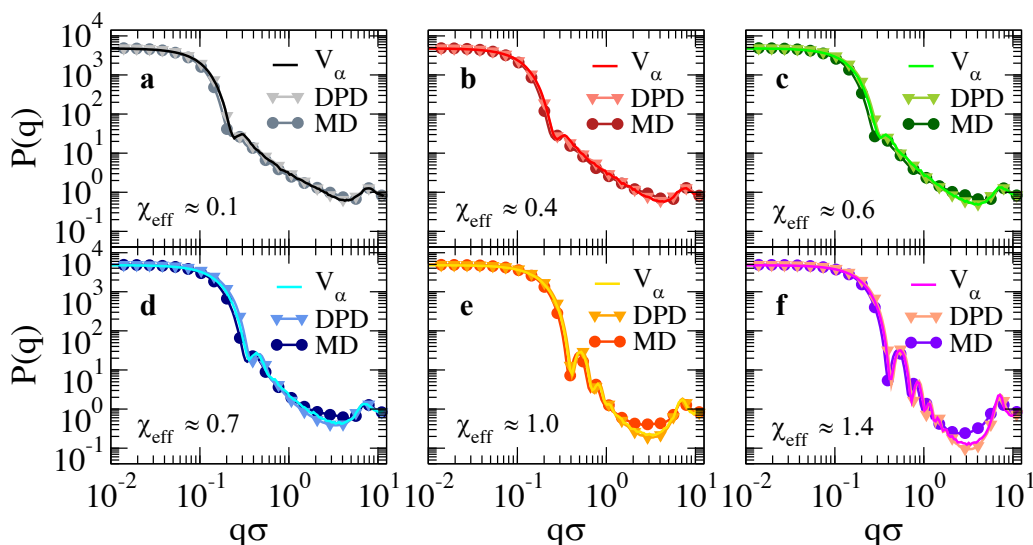


Figure 2.4: Microgel form factors for a loose microgel across the VPT. $P(q)$ as a function of $q\sigma$. Full lines refer to the implicit-solvent model, while symbols are used for MD (circles) and DPD (triangles). Each sub-panel refers to a different swelling state according to Fig. 2.2(a).

all values of the swelling parameters. As χ_{eff} increases and the solvent quality decreases, $P(q)$ shows an increasing number of oscillations which become more and more pronounced. Furthermore, the position of the first peak, which is related to the microgel overall size, shifts to larger and larger wavevectors, indicating the shrinking of the microgel. However, a subtle difference is present between the two types of employed models: while DPD results are perfectly superimposed to the implicit solvent case for all χ_{eff} , the MD results are found to be always shifted to a slightly smaller q -value with respect to them. This is a reflection of the overall microgel size, which is a bit larger for MD explicit-solvent simulations with respect to DPD and implicit solvent, due to stronger excluded volume effects, as evident from Fig. 2.1. We further notice that at relatively large wavevectors ($q\sigma \gtrsim 1$) the MD form factor systematically overestimates the DPD and implicit-solvent ones for intermediate and large values of χ_{eff} . However, all curves superimpose again at $q\sigma \sim 7$, where a small peak is found, independently of the swelling parameter value. The latter corresponds to the monomer-monomer nearest-neighbour peak and is a feature associated to the excluded-volume interactions included in the bead-spring model for polymers and to the finite size of the simulated microgel. Indeed, for larger and larger microgel size, this peak would become more and

2.3 Structural features in an explicit solvent

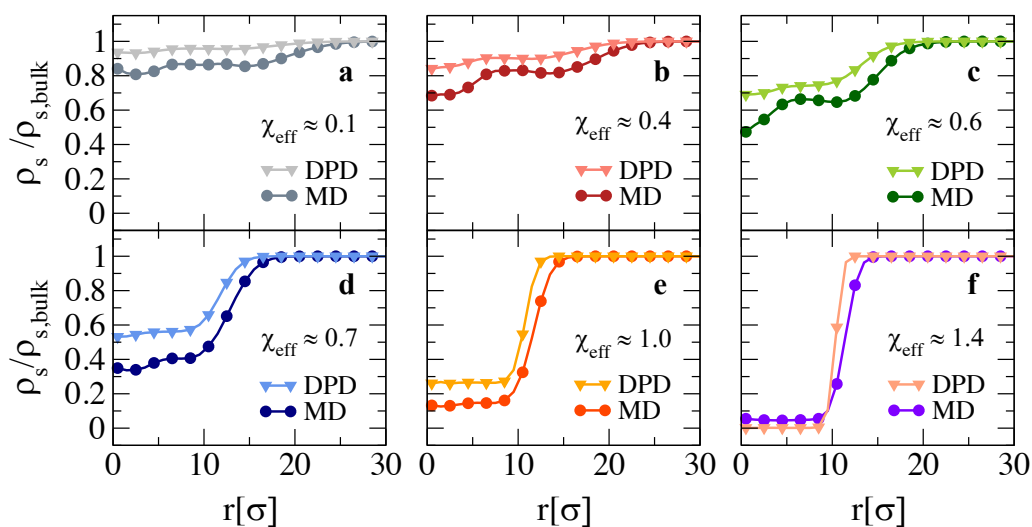


Figure 2.5: Solvent density profiles for a loose microgel configuration across the VPT. We show the solvent density profile ρ_s normalized with respect to the bulk solvent density $\rho_{s,bulk}$, as a function of the distance r from the center of mass of the microgel. Circles and triangles refer to MD and DPD solvent, respectively. Each sub-panel refers to a different swelling state according to Fig. 2.2(a).

more separated from the first one, allowing for a larger number of oscillations. In experiments, such a peak is not generally noticeable because of the soft intrinsic nature of the monomers. Thus, it is a limitation of the present modelling, which on very small length scales becomes inaccurate.

We now turn to analyze the solvent density profile ρ_s inside the microgel. The normalized profile $\rho_s/\rho_{s,bulk}$, where $\rho_{s,bulk}$ is the bulk solvent density, is shown in Fig. 2.5 as a function of the distance from the center of mass of the microgel. Clearly, the distribution reflects, as a mirrored image, the one of the microgel monomers. Indeed, when the core of the microgels becomes denser and denser, more and more solvent gets expelled. It is interesting to note that, beyond the VPT and except for the very collapsed states, a significant fraction of solvent is retained within the polymer network, even well inside the core region. At the VPT, which takes place at $\chi_{eff} \sim 0.6$, the density of the solvent inside the core is larger than 50% of the bulk value. Finally, we notice that there seems to be a consistent trend of the MD solvent to be more excluded from the network region with respect to the DPD results, again a feature associated to the larger excluded volume of the MD model. However, the two models yield qualitatively very similar results and reinforce the common view that microgels, despite their inhomogeneous structure

and dense core region, retain $\gtrsim 90\%$ of water in their swollen configuration and still contain a large amount of water well beyond VPT, in qualitative agreement with the experimental results of Ref. [46].

2.3.2 Results for a more confined microgel

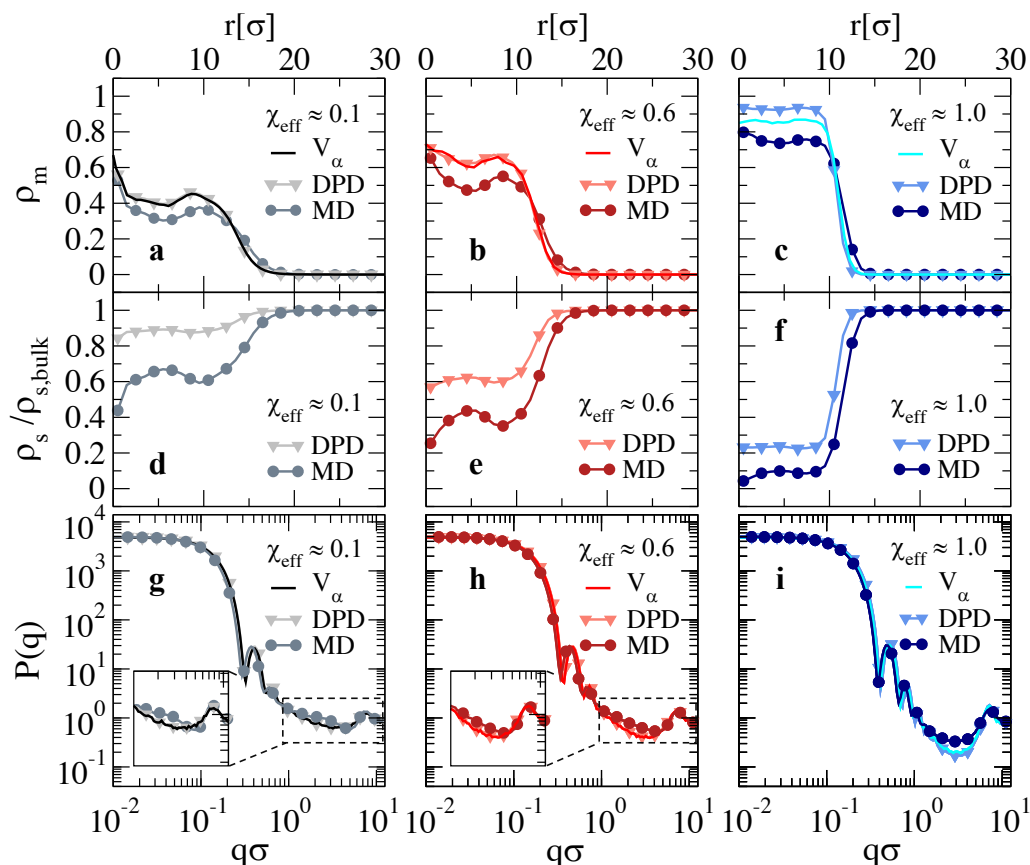


Figure 2.6: Microgel density profiles, solvent density profiles and form factors for a compact microgel across the VPT. (a-c) microgel density profiles ρ_m as a function of the distance r from the center of mass of the microgel; (d-f) solvent density profiles ρ_s normalized with respect to the solvent bulk density $\rho_{s,\text{bulk}}$ as a function of r ; (g-i) microgel form factors as a function of the wavenumber. Data are reported for a swollen state ($\chi_{\text{eff}} = 0.1$), a state close to the VPT ($\chi_{\text{eff}} = 0.6$) and a compact state ($\chi_{\text{eff}} = 1.0$). Full lines refer to the implicit solvent (V_α), while symbols are used for DPD (triangles) and MD (circles). The insets in panels g and h show an enlargement of the high wavevector region where solvent-monomer excluded volume interactions induce an excess of signal for the MD data.

We now repeat the above structural analysis for a more compact microgel topology obtained with a smaller confining radius ($Z = 15\sigma$), whose swelling curve was reported in Fig.2.2(b).

2.3 Structural features in an explicit solvent

The density profiles of the microgel are reported in Fig. 2.6(a-c) for a few selected values of the swelling parameter and again for both MD and DPD explicit solvents. We find that the DPD model reproduces very well the implicit-solvent data, particularly for the more swollen conditions. When χ_{eff} increases, the DPD monomer density in the core is slightly larger than for the implicit case. However, the corona profiles of the two microgel representations are identical. On the other hand, the MD solvent results underestimate the microgel density profile in the core and also display a different corona profile for all χ_{eff} . If compared to the findings for the looser microgel configuration (Figure 2.3), the DPD solvent model behaves similarly for both types of networks and well reproduces the implicit model data in all cases. By contrast, the MD results present systematic differences with respect to the other two sets of data making the agreement not completely satisfactory. This is a consequence of the excluded volume interactions of the solvent with the polymer. Especially for compact microgels, when excluded volume becomes more and more relevant, these assumptions in the model may become unrealistic. Thus, while for looser networks both MD and DPD explicit solvents provide a good description of the microgel, for more compact microgels the DPD model has definitely the upper hand. This is also shown in the behavior of the solvent density profiles reported in Fig. 2.6(d-f). Again we find that the MD solvent is much more excluded from the interior of the microgels at all χ_{eff} . On the other hand, we see that, notwithstanding the relative higher compactness of this microgel, a significant amount of solvent remains inside the core in the swollen states, being roughly 60% of its bulk value close to the VPT, in agreement with what found for the less confined microgel configuration and with experimental estimates [46].

The form factors, shown in Fig. 2.6(g-i), further confirm that DPD results are in good agreement with the implicit model ones. However, the MD outcomes display a clear shift in the peak position which is much more evident than for the looser configuration (see Fig. 2.4). In addition, we observe an excess of signal, highlighted in the insets of Fig. 2.6(g,h), at $q\sigma \sim 3.0$ in swollen conditions, which is absent in the DPD and implicit solvent simulations. This difference occurs at a length that is roughly twice that of the monomer-monomer peak, thus being

associated to monomers that are $\sim 2\sigma$ apart, *i.e.* with a solvent particle in between them. Such a feature is smeared out at increasing χ_{eff} , when the microgel collapses and monomer-monomer interactions become dominant. We notice that the excess signal is not observed for the looser microgel as, at the same χ_{eff} value, excluded volume interactions are far less important. Overall, this further shows that the MD model, while still acceptable for not too dense and open microgels, becomes more inaccurate for rather compact ones.

2.4 Collapse kinetics

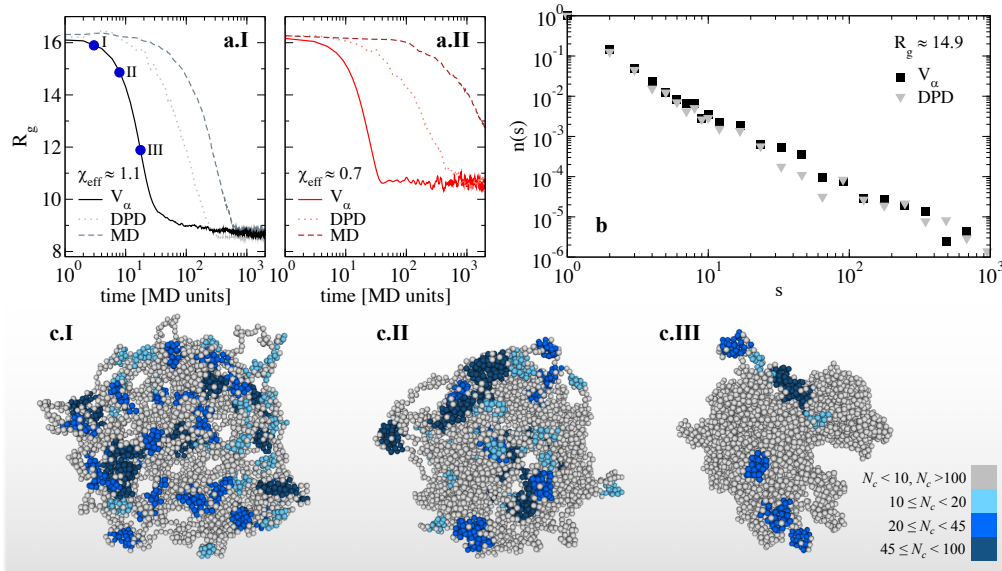


Figure 2.7: Collapse kinetics. Radius of gyration R_g as a function of time for a loose microgel ($Z = 25\sigma$) for $\chi_{\text{eff}} = 1.1$ (a.I) and 0.7 (a.II) for implicit (V_α , full line), MD (dashed and dotted lines) and DPD solvents (dashed lines); (b) cluster size distribution $n(s)$ for $R_g = 14.9$ (indicated as III in a.I) for implicit and DPD solvents. In order to improve statistics data are averaged over six different microgels configurations; (c.I-III) simulation snapshots for state points I-III (circles in a.I). Clusters are highlighted by different colors according to their size N_c (as indicated in the color bar). Light grey monomers are either found in small clusters ($N_c < 10$) or belong to the main network ($N_c > 100$).

After having established the explicit solvent models and having analyzed the properties of microgel and solvent particles in equilibrium for different values of the swelling parameters, we now turn our attention to the kinetics of collapse of the microgel in the presence of the solvent. Employing the same approach adopted in Refs. [154, 185–187] for linear polymers, we start from a swollen

microgel in a loose configuration and perform a sudden quench to a different state. In particular, we examine two final states whose value of χ_{eff} correspond to an almost fully collapsed state ($\chi_{\text{eff}} \sim 1.1$) and to a state close to the VPT ($\chi_{\text{eff}} \sim 0.7$). We then assess whether the collapse transition is affected by the presence of the solvent by comparing the kinetics of the implicit-solvent model with that obtained using MD and DPD ones. Figure 2.7(a.I-II) shows the time evolution of the radius of gyration of the microgel for the three different types of simulations at two different χ_{eff} . In all cases the curves reach at long time the same value of R_g but, in these simulation conditions, the time taken to equilibrate is different, being faster in implicit solvent simulations compared to those of DPD and MD (the slowest). All curves display a sharp one-step collapse with no trapping phenomena in metastable states. This is qualitatively in agreement with experiments in which microgels with a similar core-corona structure to ours are subjected to an abrupt temperature jump from low (swollen state) to high temperature (globular state) [188].

In order to highlight the role of the solvent, we perform a cluster analysis to identify how the microgel structure evolves during the collapse. To this aim, we detect clusters of non-bonded monomers only: two such monomers belong to the same cluster when their distance is smaller than 1.2σ , which roughly corresponds to the first peak of the radial distribution function. Afterwards, we calculate their size distribution $n(s)$ of clusters of size s for state points having the same R_g but simulated with different models.

Remarkably, we find the same cluster distribution for both implicit and DPD solvent, indicating that the solvent plays no significant role on the folding dynamics of the microgel, as shown in Fig. 2.7(b). To visualize the restructuring of the microgel following the instantaneous decrease in the solvent quality, snapshots of the microgel are reported in Fig. 2.7(c.I-III) for three different times. The microgel, while shrinking, first reorganizes by grouping monomers into small clusters (panel c.I). Each cluster is connected to the others via single or multiple links so that the structure, at an intermediate shrinking stage, displays a large number of holes and becomes increasingly inhomogeneous. As the shrinking proceeds, the clusters start to merge, becoming larger and larger in size and joining the main

network (panels c.II-III). Finally, at long times, all non-bonded monomers are connected and only a single cluster is left. We stress that this pattern is also found for the implicit model simulations and for the more confined microgel (not shown). These results strongly indicate that the solvent plays a minor influence on the structure of the microgel during the collapse transition. Indeed, at each swelling stage, the microgel has a similar structure regardless of the solvent employed, suggesting that deswelling occurs via the same sequence of transient states.

2.5 Discussion

The tunable swelling of the microgel particles has been, since their discovery, one of the most relevant features of these colloids. Indeed, the opportunity to tune the particle volume fraction without changing their number density, but only the temperature, is a formidable advantage for experimental investigations. However, this poses a computational challenge in choosing a suitable model that best describes their swelling-deswelling transition. The assembly of realistic microgel networks, here employed, correctly reproduces experimental density profiles and form factors through an implicit solvent treatment. However, the inclusion of the solvent grants additional information, such as the uptake of solvent within the polymer network or surface tension effects. For these reasons, in this Chapter, we have compared the implicit solvent results to explicit solvent ones by employing two common approaches to simulations, namely MD and DPD. We found that we can reproduce the implicit solvent swelling behavior by tuning the monomer-solvent interaction potentials after having adjusted the solvent density. This stems from the fact that, when the solvent is treated explicitly, the external pressure exerted by the solvent needs to be adjusted. In DPD simulations, the same effect can be obtained by regulating the cut-off radius.

We considered two microgels differing in the degree of compactness, which can be obtained by different synthesis protocol [189] and/or by varying the number of crosslinkers. We found that, particularly when the network is denser, excluded volume interactions play a relevant role in the description of the microgel. Indeed, in the full MD simulations, an additional peak in the structure appears at small length scales. At the same time, the internal density profile of the

microgel is also affected, resulting in a less dense core and a modified corona behavior, which is more significant in the collapsed state. Despite reducing the size of the solvent may solve excluded volume issues, doing so would dramatically increase the number of particles required to observe the same swelling behavior, as the box size is fixed by the dimensions of the microgel particle.

By contrast, DPD results better describe the implicit model ones for both microgel density profiles and form factors, at all swelling conditions. Furthermore, the DPD model reproduces the behaviour of the radius of gyration of the implicit model at different swelling conditions in an almost quantitative fashion. We have also investigated to what extent the solvent penetrates into the microgel, and we found that in the MD simulations much less solvent is present in the interior of the network, whereas DPD results seem more realistic in comparison to experimental estimates. Indeed, we find that, in the swollen state, the network is completely hydrated, retaining more than 90% of the solvent (with respect to the bulk density) in the core of the microgel. Even above the VPT the microgel contains a large fraction of solvent, which is finally excluded only at very large $\chi_{\text{eff}} \gtrsim 1.4$, amounting to temperatures $\gtrsim 60^\circ\text{C}$ according to the mapping established in Ref. [143] for PNIPAM microgels.

We also examined the collapse kinetics and assessed how the presence of the solvent affects it. We observed that, in the conditions we performed simulations, a slowing down of the collapse dynamics occurring for the more structured solvent (MD simulations) and to a smaller extent for the coarse-grained solvent (DPD simulations) with respect to the implicit simulations. However, we also found that the system, when compared at the same swelling degree (quantified by the radius of gyration of the microgel), always presents a similar structure, regardless of the model. In particular, at first the network becomes rather inhomogeneous, with regions where monomers have clustered together and empty regions. Later on, the clusters merge together and become larger and larger, until the collapse is complete and the microgel is essentially a fully folded network. Such transient behavior, featured by the appearing of crumples, has also been observed previously in simulations [170, 186, 187]. The similarity between these results with those found for an implicit solvent treatment suggests that hydrodynamic interactions

do not play a major role in the swelling-deswelling transition, which is instead mainly controlled by the quality of polymer-solvent interactions.

In summary, we have established that DPD simulations with a coarse-grained solvent constitute the most suitable method to include explicitly a generic solvent in the simulation of a microgel colloid. Even though a partially satisfactory description can be also obtained with the use of an MD solvent, this description allows for the presence of significant excluded volume interactions that brings unphysical features in the model. On the other hand, DPD simulations do show a full agreement with the implicit model and provides a realistic description of the solvent arrangement within the network. Thus, our model of realistically assembled microgels in DPD explicit solvent opens up the possibility to tackle those phenomena where the physical presence of the solvent is crucial. In particular, this model serve as a starting point to numerically investigate the so-called "Mickering" emulsions [190] and the fascinating case of microgels at fluid-fluid interfaces [113, 130, 137, 151, 191].

The main Reference for this Chapter is:

- F. Camerin, N. Gnan, L. Rovigatti, E. Zaccarelli, Modelling realistic microgels in an explicit solvent, *Scientific Reports* **8**, 14426 (2018)

Chapter 3

Conformation of a microgel at a liquid-liquid interface

While extensive experimental research has confirmed the typical fried-egg shape of the adsorbed microgels [113, 114, 122, 123, 125], numerical investigations of microgel particles adsorbed at fluid interfaces have been limited in the past years by the large amount of computational resources needed to reproduce such system. In fact, there is no computational technique other than an explicit solvent treatment to reproduce the effects of the surface tension between a chosen combination of fluids.

The first attempts in this direction were made in 2015 where, however, microgels with a regular diamond network were employed [192], and others followed in the next years [135, 149, 151]. Despite it was possible to show a flattening of the polymer with respect to the bulk, there was no direct link between internal microgel structure and conformation retained at the interface, being diamond-lattice-based microgels deprived of a more compact inner core. In this way, only loosely qualitative information could be gained. For instance, it was shown that moderately immiscible liquids could form a stable homogeneous mixture within the adsorbed microgel, with the enhanced compatibility of the two liquids related to the screening of the unfavorable contacts by the monomers of the microgel [149]. Incidentally, the fluid distribution within the polymer network has been the main focus of the recent study by Arismendi-Arrieta and Moreno [178] who made use of the microfluidic-inspired microgel model previously developed in bulk

conditions and also discussed in Section 1.1. In this case, the authors found that the uptake of solvent particles was significantly bigger in ideal networks as compared to disordered networks for their better packing efficiency; at the same time, the authors did not find fully mixed states for the solvent inside the microgel. Numerical studies of single microgels at interfaces, mostly with regular networks, were also performed to study amphiphilic systems [193, 194] or core-shell [192] and hollow microgels [192].

Instead, Harrer et al. [195] investigated the temperature dependence of single confined microgels modeled with a disordered network. By changing the temperature above and below the VPT, the authors found no dependence on the adsorbed part of the network and slight variations for the protruded part. While numerical simulations confirmed this behavior, these were performed without adding any solvent particle in the simulation box, making it difficult to build an appropriate comparison to experimental results. Independently, Bochenek et al. obtained very similar outcomes [128].

Despite all this, a detailed microscopic description and modeling of the conformation of microgels at fluid interfaces is still missing and coarse-grained numerical simulations based on a realistic microgel model could shed light on several issues. Building on the model presented for the bulk in the previous Chapters, here we provide a comprehensive modeling of a single PNIPAM particle at a flat water-oil interface. The model explicitly includes the two solvents and quantitatively accounts for the surface tension between them. The numerical results are directly compared to experiments, where the microgels are imaged *in-situ* at the water-oil interface using a cryo-SEM or are inspected after deposition from the interface onto a silicon wafer by means of Atomic Force Microscopy (AFM).¹ A good agreement between experiments and simulations is found for different crosslinker concentrations, which makes it possible to carefully assess the role played by the stiffness on the microgel structure at the interface. We thus show results for the water/hexane interface, demonstrating that the explicit-solvent microgel model developed is able to capture the physical details of single soft particles adsorbed

¹Experiments were performed by the group of Lucio Isa, based at the Department of Materials of ETH Zurich. The collaboration with the experimental group in Zurich continued in two different secondments carried out between June and November 2019.

at a flat interface, contrarily to what found for diamond-lattice-based microgel. To provide robustness to our approach, we also perform additional simulations and experiments at the water/benzene interface, which has a significantly lower surface tension, again finding good agreement between the two. Interestingly, we find that the spreading of the microgel remains mostly unaltered for both conditions, a result which provides further physical insights about the adsorption mechanism of polymer-based objects.

3.1 The control on the surface tension

Single particle modeling in bulk has allowed to establish DPD as an appropriate method to treat microgel particles in explicit solvent without the emergence of artifacts in the polymer network (Chapter 2) [196]. Further exploiting the potentialities of DPD in treating mesoscopic systems, we refine this approach to mimic the experimental interfacial tension between the two solvents, that is at the basis for the modeling of a microgel at the liquid-liquid interface. To this aim, we adapt the work of Rezaei and Modarress [197], that focuses on finding the most suitable “beading” procedure for the two solvents as well as on correctly choosing the DPD parameters based on the Flory-Huggins mixing parameter χ [5]. A brief introduction on χ based on the thermodynamics of mixing is provided in the following while an in depth discussion can be found in Ref. [5].

3.1.1 The Flory-Huggins interaction parameter χ

Despite constituting a simplified model, the Flory-Huggins (FH) theory allows to study the energy of interaction between the components of a binary mixture and thus determine the change in free energy of mixing. This is estimated by placing the two species randomly in a lattice, where each site could be thought of representing a monomer size, not necessarily linked to the chemical monomer or to the Kuhn monomer length. The results in fact are suitable not only for regular solutions, but also for polymer solutions or polymer blends. Nonetheless, correlations among sites are disregarded and thus the FH theory represents a mean-field approach to the problem.

3.1 The control on the surface tension

The energy of mixing can be written in terms of three pairwise interaction energies between adjacent interaction sites involving the species A and B of the binary mixture, *i.e.* u_{AA} , u_{BB} and u_{AB} . In this way, the average pairwise interaction of an A -monomer with one of its neighboring monomers is a volume fraction weighted sum of interaction energies

$$U_A = u_{AA}\phi_A + u_{AB}\phi_B \quad (3.1)$$

where ϕ_A and ϕ_B are the volume fractions of species A and B . Similarly, $U_B = u_{BB}\phi_B + u_{AB}\phi_A$. If each lattice site of a regular lattice has z nearest neighbors, the average energy per site occupied by species A or B is $zU_A/2$ or $zU_B/2$. To obtain the total interaction energy of the mixture U it is therefore necessary to sum all the interactions, considering that the number of sites occupied by a species is proportional to the volume fraction via the total number of sites n . In this way,

$$U = \frac{zn}{2} (U_A\phi_A + U_B\phi_B) \quad (3.2)$$

which can be rewritten, using Eq. 3.1 and $\phi = \phi_A = 1 - \phi_B$, as

$$U = \frac{zn}{2} (u_{AA}\phi^2 + 2u_{AB}\phi(1 - \phi) + u_{BB}(1 - \phi)^2). \quad (3.3)$$

Instead, the total interaction energy of both species before mixing is the sum of the energies of the two pure components weighted by their respective volume fraction

$$U_0 = \frac{zn}{2} (u_{AA}\phi + u_{BB}(1 - \phi)). \quad (3.4)$$

The energy change on mixing is

$$\Delta U_{mix} = U - U_0 = \frac{zn}{2} \phi(1 - \phi)(2u_{AB} - u_{AA} - u_{BB}). \quad (3.5)$$

Based on Eq. 3.5, the Flory-Huggins interaction parameter χ is defined as a dimensionless parameter that characterizes the difference of interactions energies in the mixture as

$$\chi \equiv \frac{z}{2} \frac{2u_{AB} - u_{AA} - u_{BB}}{kT}. \quad (3.6)$$

3.1 The control on the surface tension

The entropy of mixing is defined starting from thermodynamic definition of entropy $S = k_B \ln \Omega$, where k_B is the Boltzmann constant and Ω is the number of ways to arrange the species on the lattice. Thus, for a single molecule of species A , the entropy change on mixing is

$$\Delta S_A = k_B \ln \Omega_{AB} - k_B \ln \Omega_A = k_B \ln \left(\frac{\Omega_{AB}}{\Omega_A} \right) = -k_B \ln \phi_A \quad (3.7)$$

provided that $\Omega_A/\Omega_{AB} = n\phi_A/n$. Since we are considering a binary mixture we have that $\phi_A < 1$, $\Delta S_A > 0$. Overall,

$$\Delta S_{mix} = n_A \Delta S_A + n_B \Delta S_B = -k_B (n_A \ln \phi_A + n_B \ln \phi_B). \quad (3.8)$$

Combining Eq. 3.5 and Eq. 3.8, we obtain the free energy mixing per lattice site, also known as the Flory-Huggins equation

$$\begin{aligned} \Delta F_{mix} &= \Delta U_{mix} - T \Delta S_{mix} \\ &= k_B T \left[\frac{\phi}{N_A} \ln \phi + \frac{1-\phi}{N_B} \ln(1-\phi) + \chi \phi(1-\phi) \right] \end{aligned} \quad (3.9)$$

where $n_A = n\phi_A/N_A$ and $n_B = n\phi_B/N_B$ were used. In Eq. 3.9, the first two terms have entropic origin and always act to promote mixing. The last term has energetic origin and can be positive, thus opposing mixing, zero, in the so-called ideal mixtures, or negative. In particular, the energetic part depends on the sign of χ : if there are favorable contacts between the two species $\chi < 0$ and a mixture with an homogeneous composition is generated whereas if there is a net repulsion between species $\chi > 0$.

Incidentally, the Flory-Huggins interaction parameter shows a temperature dependence that is typically expressed, empirically, via the sum of two terms

$$\chi(T) \cong c + \frac{b}{T} \quad (3.10)$$

with the temperature-independent term c referred as the entropic contribution and the second term representing the enthalpic part. Thus, the sign of b determines the behavior of the mixture as a function of the temperature: $b > 0$ implies that χ decreases as temperature is raised, $b < 0$ favors demixing upon an increase

in temperature. The latter is the case of polymer solutions where PNIPAM – widely discussed in this Thesis – is involved which thus presents good solvent conditions at low temperatures, while the solvent quality decreases leading to polymer collapse when the temperature is risen.

The Flory-Huggins interaction parameter χ can be estimated via the solubility parameter δ . This is related to the energy of vaporization ΔE of a certain species A , that is the energy of all interactions between the molecule and its neighbors that have to be disrupted to remove the molecule from its pure state. This is defined as

$$\delta_A = \sqrt{\frac{\Delta E_A}{v_A}} \quad (3.11)$$

with v_A the volume of the molecule A . Thus, the interaction energy per site in the pure state A , previously introduced in Eq. 3.4, is related to the solubility parameter δ_A via

$$-\frac{zu_{AA}}{2} = v_0 \frac{\Delta E_A}{v_A} = v_0 \delta_A^2 \quad (3.12)$$

with v_0 the volume per site and the minus sign due to the fact that u_{AA} is defined negative while the vaporization energy is defined to be positive. Similar expression can be derived for B , while the interaction energy between A and B is estimated from the geometric mean approximation, so that $-\frac{zu_{AB}}{2} = v_0 \delta_A \delta_B$. Substituting these expressions in the definition of χ , Eq. 3.6,

$$\chi \cong \frac{v_0}{k_B T} (\delta_A - \delta_B)^2 \quad (3.13)$$

provides a straight way to quantify the Flory-Huggins interaction parameter starting from known quantities, usually tabulated for a variety of different molecules.

3.1.2 Mapping onto DPD

The link between the Flory-Huggins theory and the DPD repulsion parameters has been established by Groot and Warren in 1997 [182]. In particular, they determined a linear relation

$$\chi = f \Delta a \quad (3.14)$$

where f is a constant for a given DPD reduced density and $\Delta a = a_{AB} - a_{AA}$ is the difference in the DPD repulsion parameter between similar and dissimilar particles. This equation assumes that all particles have the same volume and density, so that interactions among different particles of the same species are always the same, that is $a_{AA} = a_{BB}$.

An important aspect is now the coarse-graining procedure, which finally allows to determine the value of χ and all the interaction parameters required in the simulation. Here, the coarse-graining is based on averaging the volumes of the involved molecules so that the DPD beads remain as small as possible [197, 198]. Considering the case of water/hexane, treated in the next Sections, their molecular volume is 30 and 218 Å³, respectively. The species will have similar volumes in case we choose each bead to be made of three water molecules and an hexane molecule to be made of two beads. In this way, the average volume is 99 Å³; this represents v_0 in Eq. 3.6. Based on this procedure, it is possible to calculate the value of χ for a water/hexane system and thus the value of the cross-interaction DPD parameter via Eq. 3.14. For the case being, this will essentially determine the quality of the repulsion between beads of different species and thus generate an interfacial tension. We also remark that no consideration concerning the microgel particle was made to calculate these parameters.

By following this procedure, in order to mimic a water/hexane (w, h) system, we use $a_{ww} = a_{hh} = 8.8$ and $a_{hw} = 31.1$ (according to the definition of a in Eq. 2.3) with a cutoff radius $r_c = 1.9\sigma$ and a reduced solvent density $\rho_{\text{DPD}} = 4.5$. The Flory-Huggins interaction parameter for this system is 24.9. The surface tension γ can be expressed in terms of the diagonal components of the pressure tensor as [198, 199]

$$\gamma = \frac{1}{2}L_z \left[p_{zz} - \frac{p_{xx} + p_{yy}}{2} \right] \quad (3.15)$$

where L_z is the measure of the side of the simulation box perpendicular to the interface; the x and y components define the plane of the interface. Under the chosen simulation conditions, we find $\gamma \approx 50$ mN/m in close agreement to the measured one [200]. Similar considerations are valid for a water/benzene interface, which is also analyzed in the next Sections and for which the DPD simulation parameters can be found in Ref. [126].

3.2 Modeling the microgel-solvent interactions

Since the parameters describing the interactions for the explicit solvent are defined by the protocol examined above, we now analyze in detail the choice of the microgel-water a_{mw} and microgel-hexane a_{mh} interaction parameters in simulations and their interplay with the surface tension between the two solvents.

The main contributions to the free energy that dictate the shape of a PNIPAM microgel adsorbed at an interface are [113]: (i) the tendency to maximise its surface so as to minimise the solvent-solvent interface; (ii) the higher affinity for water with respect to oil, which makes the polymer chains to organize in such a way to be mostly solvated by water; (iii) the elasticity of the microgel, which acts against changes in volume and shape. Given the disordered and inhomogeneous nature of the microgels, the interplay between these three contributions is non-trivial and hard to quantify *a priori*, although there exist theoretical models that can help in detecting qualitative trends [151, 201].

To choose appropriately the values of the solvophobic parameters, we first need to calculate the swelling curve of a single microgel in a one-component bulk fluid where the monomer-solvent interaction is controlled by a single solvophobic parameter a , which will be later used to mimic monomer-water and monomer-hexane interactions, respectively. The corresponding radius of gyration $R_{g,bulk}$ for a microgel with crosslinker concentration $c = 3.8\%$ is shown in Figure 3.1(a) as a function of a , quantifying the size variation of the microgel with the change in solvent affinity. Via this procedure, we determine the range of a -values for which the microgel goes from a maximally swollen case ($a \approx 1$, below which the coupling between the solvent and the monomers would be too small to properly thermalize the microgel) to a state where the majority of the solvent is expelled from the network and the microgel has collapsed ($a \approx 8$). This is the range within which a_{mw} and a_{mh} should be chosen. Considering the higher affinity for water, it is clear that one should set $a_{mw} < a_{mh}$, as these two values directly control the effective monomer-water and monomer-hexane interactions. However, the balance between a_{mw} and a_{mh} and their interplay with the given water-oil surface tension produce nontrivial effects, as shown in the following.

3.2 Modeling the microgel-solvent interactions

First of all, it is important to note that for $a_{mw} \sim 1$ the microgel never takes the “fried-egg” shape. In particular, we test three different combinations that comprise $a_{mw} = 1$ and a value of $a_{mh} > a_{mw}$, as indicated schematically in Fig. 3.1(a). Under all these conditions (see Figure 3.1(b)) the microgel only partially adsorbs at the interface, remaining mostly in the water region and retaining a quasi-spherical shape. This is explained by a too small free energy gain provided by the spreading of the particle and the reduction of the water-oil contact surface with respect to

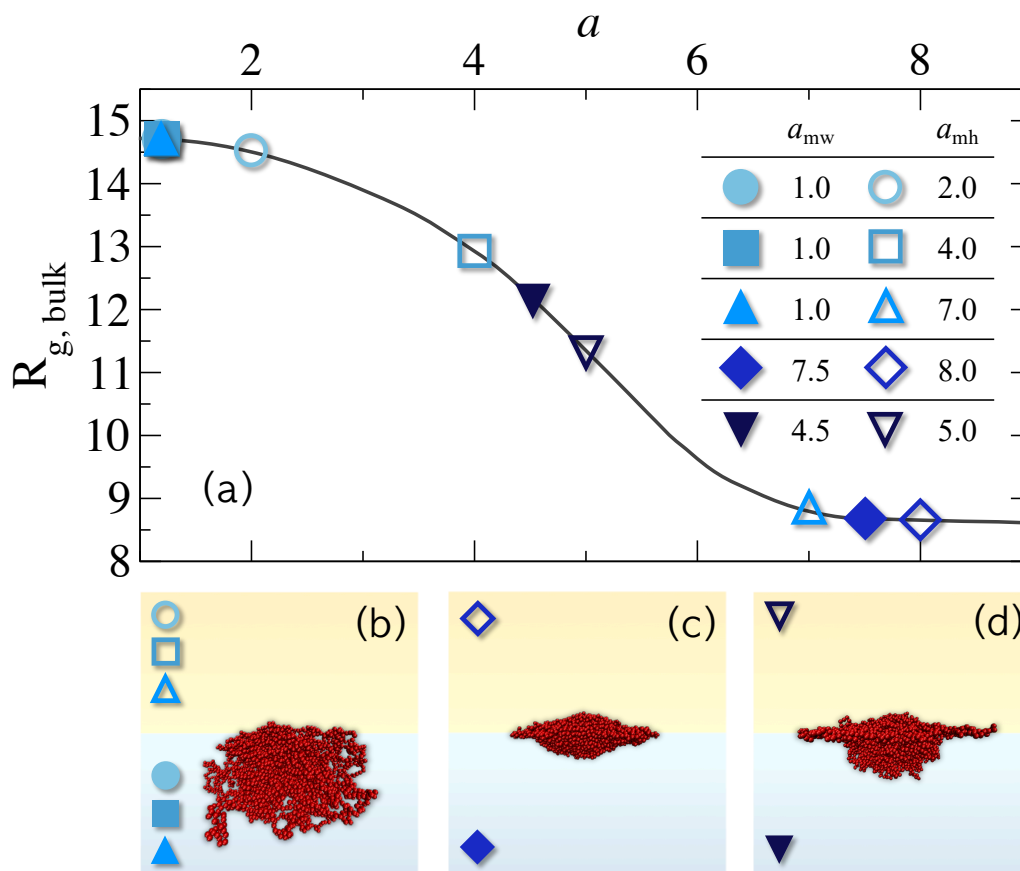


Figure 3.1: Choice of the monomer-solvent interaction parameters. (a) Radius of gyration $R_{g,bulk}$ of a microgel with crosslinker concentration $c = 3.8\%$ in a one-component bulk fluid with solvophobic parameter a . Along with the calculated swelling curve (black solid line), pairs of solvophobic parameters for monomer-water (a_{mw} , full symbols) and monomer-hexane (a_{mh} , empty symbols) interactions, which we analyze in interfacial simulations, are highlighted and listed in the inset table. As expected, for the three choices where $a_{mw} = 1.0$, $R_{g,bulk}$ coincides (the corresponding filled symbols are superimposed onto each other). The maximum extension of the microgel on the plane of the interface is obtained for the combination of parameters $a_{mw} = 4.5$, $a_{mh} = 5.0$. Representative snapshots (b), (c), (d) are side views that exemplify the conformation assumed by the microgel at the interface for different $a_{mw} - a_{mh}$ choices.

3.3 Characterization of the microgel at the liquid-liquid interface

the elastic and entropic contributions of the microgel, that are consequently found to dominate the microgel behavior under these conditions. By contrast, choosing high values of both a_{mh} and a_{mw} , the bad quality of two solvents makes the microgel collapse onto itself, taking a lens-shaped conformation, as shown in Figure 3.1(c). In this case, the microgel interacts in a rather similar manner with both solvents and a difference in protrusion on the water side, despite being present, is barely noticeable.

It is only for intermediate values of the solvophobic parameters that the elastic free energy contribution can be overcome by the interfacial term, which is strong enough to make the microgel spread over the interface to minimise the contact surface between the two solvents. In addition, the not-so-high solvophobicity now also allows the microgel to present a clear preference for water with respect to oil, thus giving rise to a well-defined core-centered protrusion in the water phase and a nearly zero protrusion into the oil. Figure 3.1(d) shows a simulation snapshot of a microgel taking the “fried-egg” conformation obtained by choosing $a_{mw} = 4.5$ and $a_{mh} = 5.0$, which are the values we will use for the microgel-water/hexane system throughout the next section.

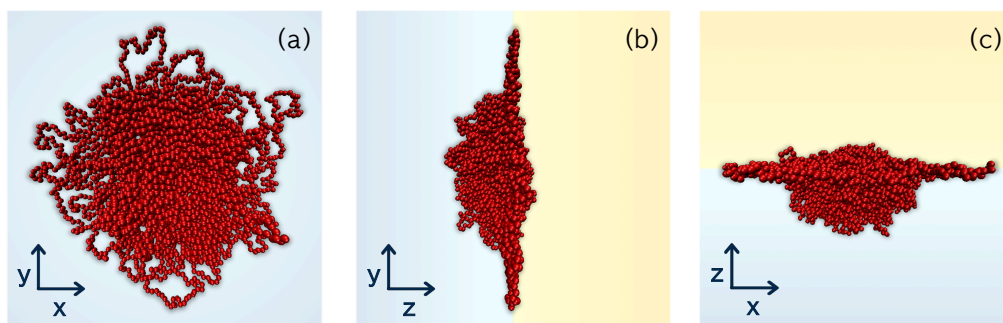


Figure 3.2: A microgel at a liquid-liquid interface. Simulation snapshots of a microgel at a water-oil interface in the three different planes of observation: (a) top view (interface plane xy), (b,c) side views in which $z < 0$ corresponds to the water region and $z > 0$ to the oil one, respectively. The observed conformation is loosely called “fried-egg” shape.

3.3 Characterization of the microgel at the liquid-liquid interface

The typical microstructure of an interfacial microgel, resulting from the interplay between particle architecture and surface tension, is reproduced in Fig. 3.2. We recall that the internal structure of microgels comprises of a rather homogeneous core, with a higher density of crosslinkers, and a loose corona complemented by a non-negligible number of dangling chains, where the number of crosslinkers is rather low [82, 202]. As a consequence, a clear flattening of the corona takes place at the interface, which exposes the core, giving rise to a protrusion in the center of the microgel. A realistic modeling of the internal degrees of freedom appears to be crucial to reproduce such phenomenology. Indeed, it is the polymeric, inhomogeneous nature of the system that allows microgels to deform and assume the “fried-egg” shape.

More information on how the microgel arranges itself at the interface is gained by looking at the density profiles reported in Fig. 3.3. In particular, panel (a) displays the $\rho(z)$ density profile, calculated at a distance z from the interface, and obtained by dividing the simulation box along the z -axes into three-dimensional bins that are parallel to the interface. Panel (b) shows instead the $\rho(\zeta)$ density

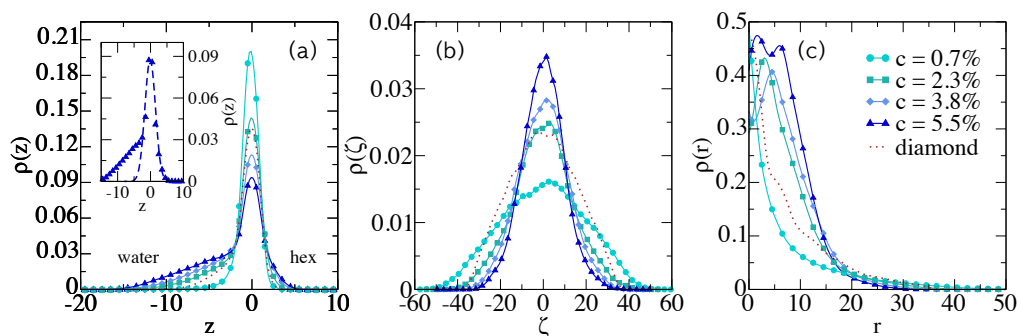


Figure 3.3: Density profiles of the microgels at the interface for disordered ones with $c = 0.7, 2.3, 3.8, 5.5\%$ and for the diamond-lattice-based microgel with $c = 5\%$. Panel (a) shows the density profiles $\rho(z)$ obtained by binning the simulation box parallel to the interface. The inset shows a gaussian fit (dashed line) of the portion of microgel that stands at the interface for $c = 5.5\%$. Panel (b) reports $\rho(\zeta)$ and shows how the microgel flattens at the interface. Panel (c) shows the radial density profiles taken with respect to the center of mass of the microgel; the same four crosslinker ratios are analyzed. Lines are guides to the eye. All data are normalized to the average number of particles of the $c = 5.5\%$ microgels.

3.3 Characterization of the microgel at the liquid-liquid interface

profile, where the bins are taken orthogonally to the interfacial xy -plane and $\zeta = x, y$. This is calculated at distance ζ with respect to the center of mass of the microgel and averaged over the two directions. Finally, the radial density profiles $\rho(r)$, obtained by building spherical shells at distance r from the center of mass of the microgels, are reported in Fig. 3.3(c), providing information on the core size of the microgels. In each panel, we report the density profiles for four different values of the crosslinker ratio c , namely 0.7, 2.3, 3.8 and 5.5%. For completeness, we also provide results for a diamond network microgel with a representative crosslinker concentration $c = 5\%$.

We start by discussing $\rho(z)$. Two main regions are detected: (i) the central part of the profile, which corresponds to the section of the microgel that builds up at the interface. As expected, the maximum density is found at $z = 0$ owing to the greater number of monomers that are present at the interface. The extent of the interfacial region can be properly identified by a gaussian fit to the data, shown in the inset of Fig. 3.3(a) for $c = 5.5\%$, which captures all the signal on the oil side for all studied values of c and confirms the poor solubility of the polymeric material in oil; (ii) a protrusion of the microgel in water, which strongly depends on the crosslinker concentration. Indeed, the more the microgel is crosslinked, the more the core is pronounced, giving rise to an increasingly asymmetric tail in the profiles on the water side. Looking at $\rho(\zeta)$ instead, the highest density is found at the center of the interface ($\zeta = 0$) due to the presence of the core. The distributions become broader and broader as c decreases, since the difference between the core and corona regions is less defined when the number of crosslinkers is small. The same features are also confirmed by the radial profiles $\rho(r)$, where a stronger initial bump signals the presence of a denser, well-defined core, which is indicative of a “fried-egg” shaped microgel. For $c < 1\%$ this feature is found to be almost absent, while it manifestly develops for $c \geq 2.3\%$.

Comparing with the regular diamond network [149, 151, 203] with $c = 5\%$, for which the density profiles are also reported in Fig. 3.3, we find that even for this high value of crosslinker concentration a well-defined core is not present. This is also clearly visible in the snapshots reported in Fig. 3.4. Interestingly, the microgel extension at the interface is even larger than that of the disordered

3.3 Characterization of the microgel at the liquid-liquid interface

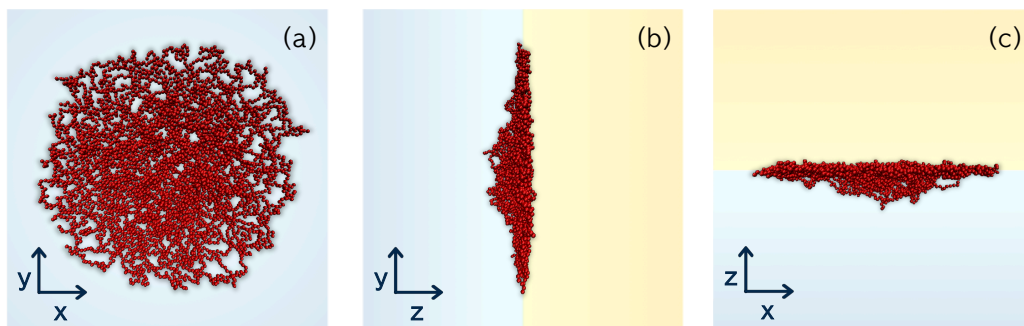


Figure 3.4: Diamond based microgel network. Simulation snapshots of a microgel built on regular diamond network with $N \approx 5000$ monomers and $c = 5\%$ at a water/hexane interface in the three different planes of observation: (a) top view (interface plane xy), (b,c) side views in which $z < 0$ corresponds to the water region and $z > 0$ to the oil one, respectively.

one, again due to the absence of the core. These effects produce an unrealistic conformation of the diamond microgel at the interface, which resembles the one assumed by the disordered network with a much lower crosslinking ratio. Thus, for the regular topology, the “fried-egg” shape is not observed in simulations, limiting the applicability of the diamond model in the description of real particles at interfaces.

Experimentally, we have access to indirect measurements of the lateral microgel size at the water/hexane interface after deposition onto a silicon wafer [113] (see Ref. [126] for experimental details). In this way, the microgels dry out but, following previous works [100, 204], we can assume that they retain the same

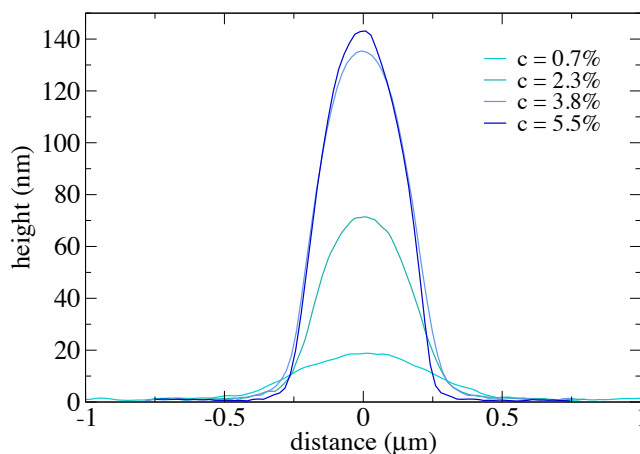


Figure 3.5: AFM height profiles. Height profiles of dry isolated microgels deposited onto silicon wafers, extracted from AFM images, for different values of the crosslinker ratios c .

3.3 Characterization of the microgel at the liquid-liquid interface

extension they had at the interface also under these conditions. The height profiles of dried microgels are reported in Fig. 3.5 as a function of the crosslinking ratios. Qualitatively, they show the same behavior as observed in $\rho(\zeta)$ calculated with simulations (Fig. 3.3), presenting a lower degree of spreading as the crosslinking ratio increases.

3.3.1 Numerical/experimental comparison

In order to assess the validity of the theoretical model, we perform a qualitative comparison with experiments, in terms of both the extension on the interfacial plane \mathcal{D} and the height h of the microgel perpendicular to the interface.

Figure 3.6 shows AFM images of microgels with different c after spreading at the water/hexane interface and deposition onto a silicon substrate. We also report FreSCa cryo-SEM images that provide a picture of the microgel upon vitrification of water and removal of the oil, and the numerical surface profiles from the water and oil sides of the interface. In FreSCa micrographs, the visible part of the microgel is the one protruding from the water phase into the oil. The outer corona is not visible with this technique as the low density of the dangling polymers makes it difficult to achieve sufficient contrast in the SEM imaging. Furthermore, since microgels do not cast any shadow following tungsten coating at a 30° angle, it can be seen that their effective contact angle is below 30° and that they are mostly immersed in water [113]. Comparing the microgel size from the FreSCa cryo-SEM images (Table 3.1 and blue circles in Fig. 3.6) and the AFM data (Table 3.1 and red circles in Fig. 3.6), we see that the measured size \mathcal{D}_{FreSCa} closely corresponds to the size of the more densely crosslinked core part of the microgel. Moreover, the data show that the thickness of the corona relative to the core size becomes smaller as the crosslinking ratio increases, which is expected since a more crosslinked microgel presents less dangling polymer chains.

To compare with numerical results, we first need to determine how the different quantities can actually be compared. In all the measurements, we take as a reference the corresponding microgel size in bulk, for which we measure the hydrodynamic radius R_H , usually determined experimentally via DLS, implying $\sigma_H = 2R_H$. In simulations, R_H is not readily available and thus we adopt an

3.3 Characterization of the microgel at the liquid-liquid interface

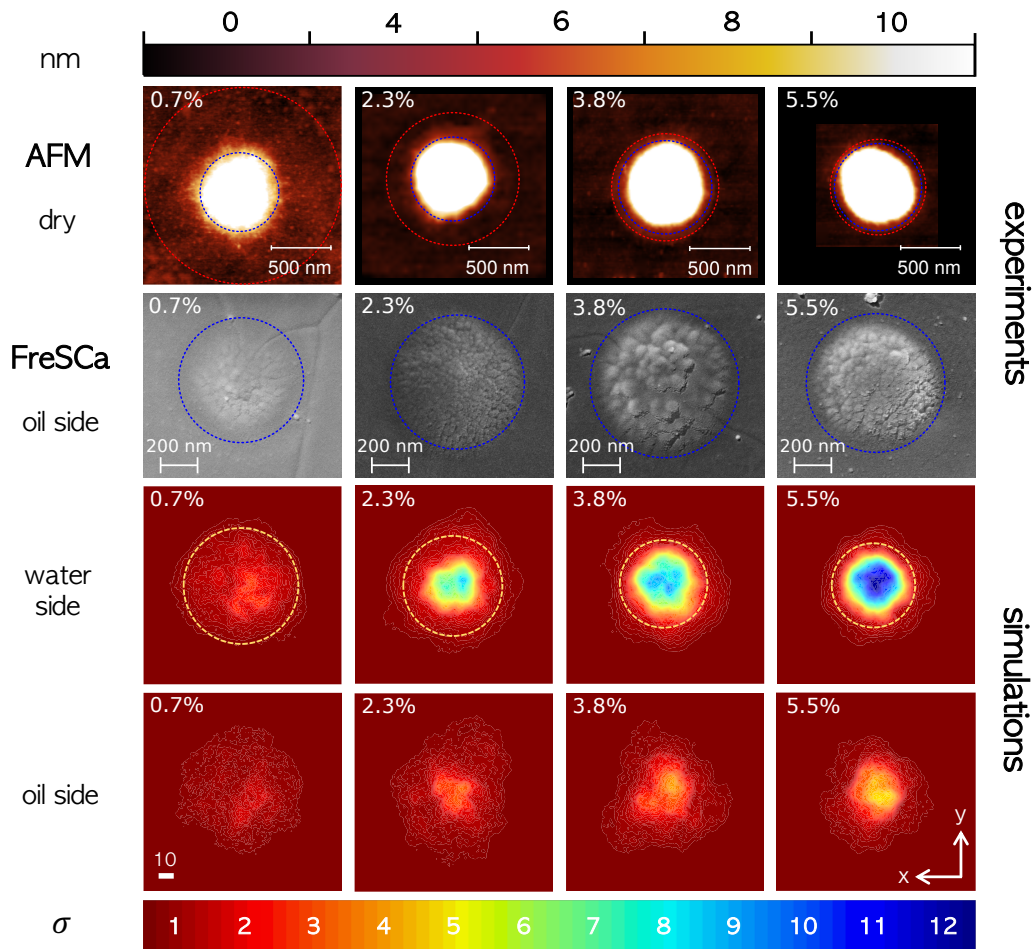


Figure 3.6: Conformation of microgels at the interface in experiments and simulations by varying c . Top row: AFM height images of dried isolated microgels deposited from the water/hexane interface onto a silicon substrate. The top colour bar represents the height measured with AFM in nm . The height scale is saturated at 10 nm in order to show clearly both the thin corona and the higher core in the same image; second row from top: corresponding cryo-SEM images obtained by the FreSCa technique showing a frontal view of the interface with the microgels protruding into the oil phase, after removal of the latter. Red circles correspond to the average diameter measured from the AFM images, and blue circles from the FreSCa cryo-SEM images. It is evident that FreSCa cryo-SEM visualizes the core only; third and fourth rows from top: numerical surface plots of the microgels from the plane of the interface ($z = 0$) towards the water and oil phases, respectively. Yellow circles are representative of the average extension taken for each of the crosslinker ratios analyzed. The bottom colour bar refers to the height of the numerical height profiles for both water and oil sides in units of σ .

operative definition. Namely, we consider the radial density profile $\rho(r)$ of the microgel, and take R_H at the distance where $\rho(r) = 10^{-2}$. The obtained values of R_H compares well to those that are obtained by using the gyration radius R_g , since it was experimentally observed that for microgels $\frac{R_g}{R_H} \approx 0.6$ [67, 68].

3.3 Characterization of the microgel at the liquid-liquid interface

c	σ_H	\mathcal{D}_{AFM}	\mathcal{D}_{FreSCa}
0.7	628 ± 165	1618 ± 98	652 ± 45
2.3	618 ± 83	1095 ± 66	700 ± 62
3.8	597 ± 127	882 ± 30	777 ± 39
5.5	574 ± 73	786 ± 30	724 ± 29

Table 3.1: Experimental characterization in bulk and comparison between AFM and FreSCa. Size of the microgels measured by DLS σ_H and their extension after deposition on a silicon wafer measured by AFM \mathcal{D}_{AFM} , as well as their extension at the interface from FreSCa cryo-SEM measurements \mathcal{D}_{FreSCa} , for different values of the crosslinking ratio c . Data are expressed in nm .

As discussed above, quantitative experimental measures of the particle size at the interface are carried out with an AFM after deposition on a silicon wafer. In this way, we obtain the maximum extension of the particle under the assumption that it matches the one after deposition, as previously established for microgels [130]. From the AFM images, after solvent removal, we can also extract the particle height h , that corresponds to the projected polymer density profile onto the plane of the interface. Unfortunately, our experiments do not make it possible to access the solvated conformation of the microgel at the interface and its protrusion in either of the two liquids, a precious information that is accessible from the numerical simulations only. However, we notice that, even under dry conditions, a small amount of water, up to about 10%, may still be retained in the polymer network. To best reproduce the experimental acquisition techniques, we numerically calculate the extension of the flattened particle at the interface \mathcal{D} as the average maximum distance that opposite edges of the polymer reach on the xy -plane. For the height we report two estimates, for the fully solvated microgel and for the packed network configuration. The first is computed by drawing a surface profile on the oil and water sides of the microgel; the sum of the distances from the plane of the interface defines the height of the microgel. The latter is instead obtained by accumulating on the plane of the interface the number of monomers that occupy a certain (x, y) coordinate, independently of z . The above measures are provided with an error bar that accounts for the differences in the number of monomers and topology of the configurations over which we average.

A comparison between experimental and numerical results is provided in Fig. 3.7 where dimensionless observables are used. In particular, we define the following ratios: $[\%]_{\mathcal{D}}$ quantifies the increased extension of the microgel size at

3.3 Characterization of the microgel at the liquid-liquid interface

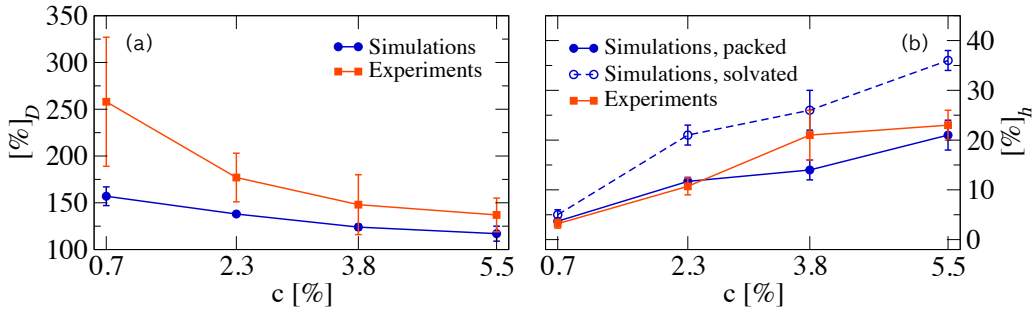


Figure 3.7: Comparison simulations/experiments. (a) Extension ratio $[\%]_{\mathcal{D}}$ with respect to the bulk diameter σ_H for the crosslinker concentrations c analyzed, for simulations (blue circles) and experiments (orange squares); (b) height ratio $[\%]_h$ with respect to the bulk diameter σ_H , measured by AFM for the dry microgel (orange squares) and calculated from simulations for the fully solvated microgel (empty blue circles) and for the packed microgel configuration (full blue circles).

the interface with respect to its bulk value σ_H , while $[\%]_h$ represents the ratio of the microgel height with respect to σ_H . Table 3.2 reports in a detailed manner all the quantities presented in Fig. 3.7.

		Simulations					
c	σ_H	\mathcal{D}	$[\%]_{\mathcal{D}}$	h (packed)	$[\%]_h$ (packed)	h (solvated)	$[\%]_h$ (solvated)
0.7	53.6 ± 0.3	85 ± 5	158 ± 10	2.0 ± 0.2	3.7 ± 0.4	2.9 ± 0.5	5 ± 1
2.3	48.1 ± 0.1	66.2 ± 0.6	138 ± 1	5.6 ± 0.4	11.7 ± 0.9	10 ± 1	21 ± 2
3.8	45.8 ± 0.2	57 ± 1	124 ± 3	6.4 ± 0.9	14 ± 2	12 ± 2	26 ± 4
5.5	43 ± 1	51 ± 2	118 ± 8	9 ± 1	21 ± 3	15.4 ± 0.7	36 ± 2

		Experiments				
c	σ_H	\mathcal{D}	$[\%]_{\mathcal{D}}$	h	$[\%]_h$	
0.7	628 ± 165	1618 ± 98	258 ± 69	20 ± 1	3.2 ± 0.9	
2.3	618 ± 83	1095 ± 66	177 ± 26	66 ± 6	10.7 ± 1.7	
3.8	597 ± 127	882 ± 30	148 ± 32	125 ± 12	21 ± 5	
5.5	574 ± 73	786 ± 30	137 ± 18	133 ± 7	23 ± 3	

Table 3.2: Comparison simulations and experiments. Summary table reporting: for experiments, the size of the microgels σ_H , the extension \mathcal{D} and dry height h of the microgel at the interface for $c = 0.7, 2.3, 3.8, 5.5\%$; for simulations, the solvated and packed heights h . Data are given in nm for the experiments and in units of σ for the simulations. Ratios are in $\%$, always referring to the bulk size σ_H , which is taken from the bulk radial density profiles at $\rho = 10^{-2}$ for simulations and from DLS measurements for experiments.

3.3 Characterization of the microgel at the liquid-liquid interface

Starting with the analysis of the interfacial extension of the microgel, we find a qualitative agreement between experiments and simulations confirming that, by increasing the crosslinker concentration, microgels are less extended at the interface. Indeed, increasing c the polymer network becomes stiffer due to the fact that polymer chains are closer to each other and less free to diffuse around. At the interface this translates into a more compact shape. At the same time, the more the corona contracts, the more the core of the microgel becomes denser and protrudes towards the water phase, as evidenced also in the density profiles and in the height profiles for both simulations and experiments. An important contribution to the total extension of the microgel is given by the flattening of the corona at the interface. As it can be noticed by the height profiles in Fig. 3.6, the spreading is responsible for the increase of $\approx 50 - 60\%$ of the total extension within the interfacial plane. At low crosslinker concentration, a true core can no longer be distinguished and this ratio certainly increases.

It is also important to note that the experimental height of the microgel grows by almost six times moving from $c = 0.7\%$ to $c = 5.5\%$, as shown in Fig. 3.7(b). Interestingly, the cryo-SEM images in Fig. 3.6 show an increase in height also in the oil side, where a visible protrusion, due to the core, is observed at high crosslinker concentration. In simulations, the fully solvated microgel height and the packed one bracket the experimental results, showing a good agreement especially for the low-crosslinked microgels. Moreover, they follow a similar trend as a function of crosslinker concentration.

We notice that a systematically higher extension is found in experiments with respect to numerical results, which might be due to the way in which the size of the microgel is quantified in the two cases and/or due to size effects in simulations. Indeed, our *in silico* microgels are relatively small to correctly take into account the overall extent of the corona. Although we are able to maintain a realistic core-to-corona ratio in terms of their relative extension, we found a significant difference in the maximum chain length, particularly those of the corona or the so-called dangling ends [205]. This may explain the smaller extension of the microgel at the interface with respect to experiments, where the outer dangling polymers are taken into account up to the limit of AFM resolution.

3.3 Characterization of the microgel at the liquid-liquid interface

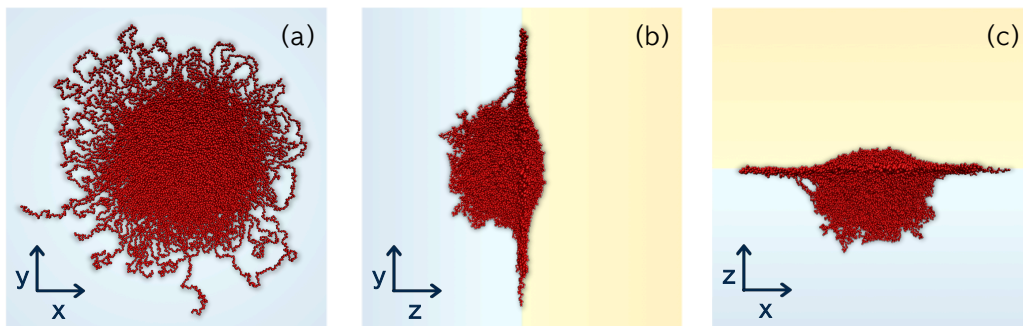


Figure 3.8: A large microgel at a liquid-liquid interface. Simulation snapshots of a large microgel with $N = 42000$ monomers and $c = 5\%$ at a water/hexane interface in the three different planes of observation: (a) top view (interface plane xy), (b,c) side views in which $z < 0$ corresponds to the water region and $z > 0$ to the oil one, respectively.

To further address this point, we tested larger – yet far from experimental conditions – microgels, observing very minor changes in the trends, despite a large increase in computational cost. In particular, we simulated microgels made of 42000 monomers at a water/hexane interface with $c = 3\%$ and $c = 5\%$. Snapshots of the 5% microgel at the interface are shown in Fig. 3.8 from different perspectives, in full analogy with Fig. 3.2. The way the microgel builds up at the interface is very similar to the smaller one, as evidenced by the $\rho(z)$ and $\rho(\zeta)$ (with $\zeta = x, y$) density profiles reported in Fig. 3.9. Also, the presence of a denser core and a thinner corona is confirmed. We observe a more evident core structure in the larger microgels, as signalled by the larger protrusion in $\rho(z)$. However, it is important to note that the interfacial extension does not vary significantly

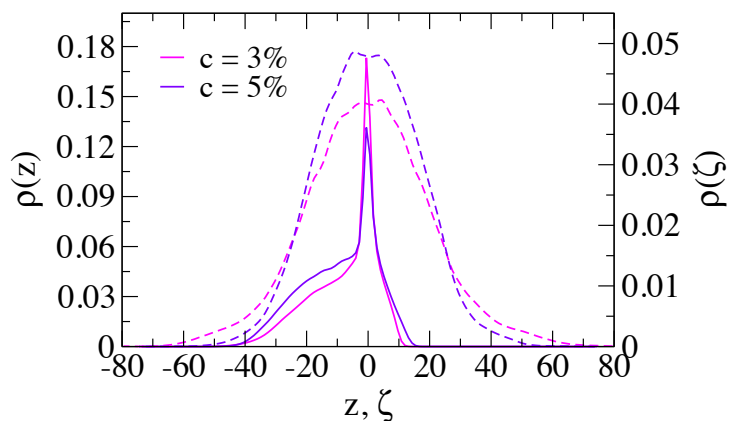


Figure 3.9: Density profiles of larger microgels. We show $\rho(z)$ and $\rho(\zeta)$ density profiles for microgels with $N \sim 42000$ microgel with $c = 3\%$ and $c = 5\%$.

between the two structures. Indeed, we estimate $[\%]_{\mathcal{D}}$ to be 140% for $c = 3\%$ and 121% for $c = 5\%$. These values are in agreement with the trends reported for the smaller microgels in Table 3.2. We stress, however, that in order to evaluate these properties for a $N \sim 42000$ monomers microgel in between the two solvents takes about 10 times in terms of computing time. Since the simulated microgel is still very far away from the size of a real one and given the similarity of the results, we concentrate on the small microgel case. Nonetheless, this additional study provides robustness to our approach, confirming the consistency of the method and the presence of a clearly identifiable “fried-egg” shape, which is even more pronounced for the larger microgels.

3.4 Effects of a different surface tension

We now examine the results for a liquid pair with a different surface tension, to prove the soundness of our approach. In particular, we analyze the case of a water/benzene interface, whose measured surface tension [200] is approximately 30% lower than the one of water/hexane. AFM results for microgels deposited on the water/benzene interface are reported in Table 3.3. The qualitative behavior of the microgel configuration is similar to that observed for water/hexane interface, with a decreasing extension and increasing height of the microgel for increasing crosslinking ratio. Quantifying the difference between the two interfaces, we observe that for $c \gtrsim 3\%$ there is substantially no change of the microgel configuration within the experimental errors. A larger difference is observed for small c , particularly for the 0.7% case, where the explored change in surface tension is able to modify the response of such a loose polymer network.

In simulations, since we expect a similar solubility of PNIPAM in both hexane and benzene, the microgel-solvent interaction parameters have been correspondingly re-mapped. The new monomer-solvent interaction parameters have different absolute values in order to match the new surface tension, but they are still chosen in an intermediate range of the swelling curve in bulk (not shown). Figure 3.10 shows $\rho(z)$ and $\rho(\zeta)$ calculated for the same microgel configuration at the water/benzene and water/hexane interfaces for the crosslinker concentration $c = 3.8\%$. Despite the reduction of the surface tension by roughly 30%, we observe

3.4 Effects of a different surface tension

Experiments				
c	\mathcal{D}	$[\%]_{\mathcal{D}}$	h	$[\%]_h$
0.7	1474 ± 62	234 ± 62	22 ± 2	3.5 ± 1.0
2.3	923 ± 64	149 ± 23	58 ± 4	9.4 ± 1.4
3.8	869 ± 48	146 ± 32	135 ± 9	23 ± 5
5.5	724 ± 68	126 ± 20	160 ± 27	28 ± 6

Table 3.3: Experimental results at the water/benzene interface reporting the extension \mathcal{D} and dry height h of the microgel at the interface for $c = 0.7, 2.3, 3.8, 5.5\%$. Data are given in nm . Ratios are in %, referring to the bulk size σ_H .

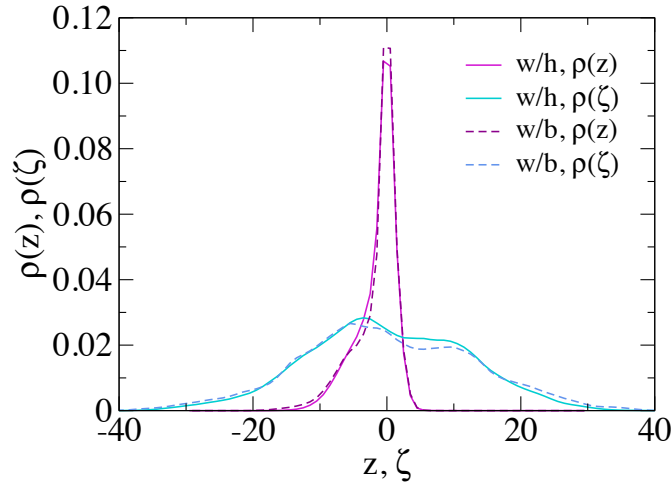


Figure 3.10: Comparison between a microgel at water/benzene and water/hexane interfaces. Effects on $\rho(z)$ and $\rho(\zeta)$ of a different surface tension between different combinations of immiscible liquids, corresponding to water/hexane (w/h) and water/benzene (w/b), for $c = 3.8\%$.

only very small differences in the distribution of monomers for the two interfaces. In particular, the extension on the interfacial plane does not vary significantly, in full agreement with the experimental results. This holds especially for the most widely adopted fraction of crosslinkers $c \gtrsim 3\%$, suggesting that, even for the lowest analyzed surface tension, an equilibrium between spreading and internal elasticity can still be reached. Similar effects have been found when studying the microgel conformation at the interface as a function of pH [113] and of temperature below the VPT [206], as also reported in the Introduction. The microgel extension appears to be almost “saturated” in the studied cases, suggesting that we may only get significantly different results for much lower surface tensions or for large variations of the solution conditions.

3.5 Summary

The emerging potentialities of soft particles, particularly microgels, at liquid-liquid interfaces require microscopic models that reproduce the most relevant features observed experimentally. In this Chapter, we put forward an accurate theoretical description of a single microgel confined at the interface between two immiscible fluids. We first discussed the possible choices for water-monomer and oil-monomer interactions, discriminating cases where the microgel does not adsorb at the interface and those where the configuration is too compact. We interpreted these different scenarios as resulting from the balance between the adsorption and the elastic free energy contributions. We thus determined the optimal conditions under which the microgel maximizes its extension on the plane of the interface and protrudes toward the water phase. In this way, we have been able to reproduce the characteristic “fried-egg” shape at the interface and the increased flattening of the microgel when the number of crosslinkers decreases. Such behavior is not observed for regular networks such as the diamond one, being devoid of a well-defined core. Moreover, we found that the numerical results are robust to size effects and are also valid for different values of the surface tension. Interestingly, the microgel configuration does not change significantly between a water/hexane and a water/benzene interface, despite a 30% variation of the surface tension.

Our modelling is consistent with experimental evidences on several aspects. Firstly, we tune the simulated surface tension to reproduce the one of a water/hydrocarbon interface by adjusting the repulsion parameters and the density of a coarse-grained DPD fluid. Such a solvent description may be exploited in other calculations of particles and polymers at interfaces, given its flexibility in the choice of the involved parameters. Moreover, our study builds on a microgel model whose bulk swelling behavior, density profiles and form factors are directly comparable to the experimentally measured ones [143, 174]. Notably, the internal degrees of freedom are taken into account to reproduce the disordered polymeric network in a realistic way, also with respect to its inhomogeneous density profile, made of a denser core and a fluffier corona. By comparing numerical and experi-

mental results, we found confirmation of the important role played by the corona in determining the extension of the microgel on the plane of the interface.

The aspects we have dealt with are particularly relevant in perspective. From a fundamental point of view, the microscopic model presented here constitutes the basis for the numerical study of more complex assemblies. To investigate the physical origin that underlie the formation of two dimensional or quasi-two-dimensional structures, it is necessary to evaluate microgel-microgel effective interactions on the interface.

Regarding applications, the emulsion-stabilizing effect as well as the use in surface patterning are only some of the recent advances that have been proposed [29, 207, 208] and still require deeper investigations. For instance, patterned thermoresponsive polymer coatings have been identified as a valuable tool in bio-medicine for non-invasive control over cell-adhesion [209]. For these and other purposes, the microscopic understanding of a two dimensional interfacial system, from single-particle studies up to collective behavior, is expected to strongly advance the field [191, 210] and is at the basis for the development of new nano- and micro-structured materials.

The main Reference for this Chapter is:

- F. Camerin, M. A. Fernandez-Rodriguez, L. Rovigatti, Maria-Nefeli Antonopoulou, N. Gnan, A. Ninarello, L. Isa, E. Zaccarelli, Microgels adsorbed at liquid-liquid interfaces: a joint numerical and experimental study, *ACS Nano* **13**, 4548 (2019)

Chapter 4

Microgels at interfaces as effective 2D elastic particles

The conformation retained by a microgel at the interface is a direct consequence of the deformability of polymeric colloids. This feature will influence the collective behavior of these particles and therefore the properties of a macroscopic ensemble. In order to understand what differences to expect and to compare the case of the bulk with that of the interface, before moving on to analyze the latter, it is important to recall the most recent developments for the calculation of the effective interactions in bulk.

While for many years microgels in bulk were thought to interact as an ideal Hertzian model [74], the validity of this assumption has been confirmed to be limited to the regime of low concentrations [75]. The Hertzian model describes the geometrical changes of an elastic sphere upon diametral compression and it is directly linked to the elastic moduli of the body. Furthermore, it is known to be applicable only in the small compression regime. In these conditions, the Hertzian interaction in three dimensions reads as

$$V_H(r) = \begin{cases} U_0(1 - r/\sigma)^\alpha & \text{if } r/\sigma < 1 \\ 0 & \text{otherwise} \end{cases} \quad (4.1)$$

where $\alpha = 5/2$ and the prefactor, also called repulsion strength, $U_0 = \frac{2Y\sigma^3}{15(1-\nu^2)}$ specifically depends on σ (here intended as the size of the particle) and on the

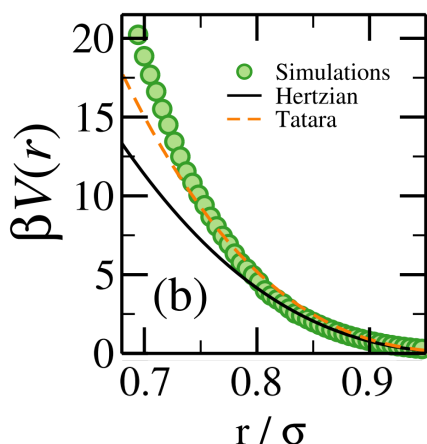


Figure 4.1: Effective interaction in bulk. Adapted from Ref. [211]. Symbols are the effective interaction potential between two microgels in bulk extracted from simulations; the full line is the Hertzian fit (see Eq. 4.1) where Y and ν are calculated from elasticity theory calculations and σ is left as a free parameter; the dashed line is a comparison to the Tatara theory.

zero-stress elastic properties of the single particle, the Young's modulus Y and the Poisson's ratio ν . Therefore, once Y and ν are known, it is directly possible to calculate the interaction within the Hertzian theory (see also below).

This approach has been employed by Rovigatti et al. [211] who compared theoretical calculations with the effective interactions obtained by molecular dynamics simulations. These calculations were based on the same microgel model used and described in the previous Chapters, thus accounting for a disordered polymeric network and favorable comparison to experiments. As also reported in Fig. 4.1, it is clear how the Hertzian theory does account for the microgel-microgel repulsion only in very restricted range, that is below $\approx 6k_B T$, as compared to the outcome provided by the numerical calculation. We underline that the Hertzian fit to the numerical results has been performed by fixing the values of Y and ν , previously computed via elasticity theory calculations. When the interaction between the particles increases over few times the thermal energy, the Hertzian nature of the microgel breaks down as a consequence of the stronger deformation of the particles. Effective interactions are also compared to the Tatara theory, which describes the deformation of a homogeneous sphere subjected to a large strain. Despite the agreement between theory and simulations improves, it cannot capture the microgel-microgel interactions for strengths higher than $10 - 20k_B T$.

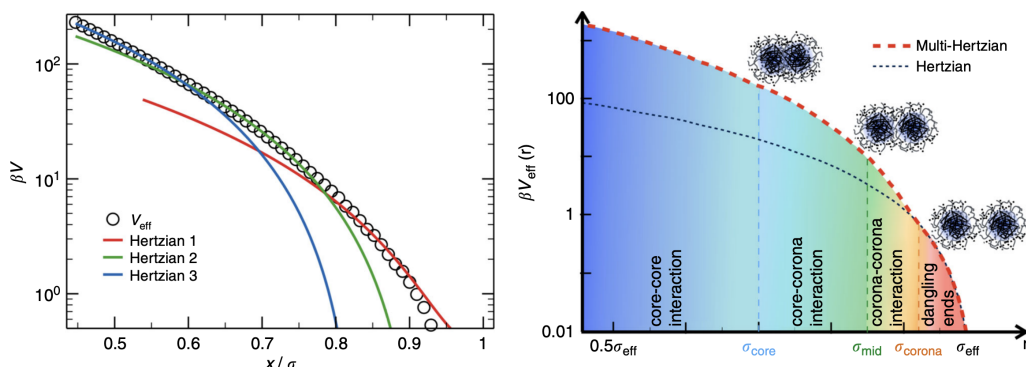


Figure 4.2: Multi-Hertzian model. Reproduced from Ref. [75]. Left: symbols are the effective interaction potential between two microgels in bulk extracted from simulations while full lines represent the fit with the Hertzian model (with increasing Hertzian strength) at different distances. Right: overall multi-Hertzian, as compared to a single Hertzian potential. Different length-scales correspond to different contact regions in the microgel structure: dangling chains, corona-corona, core-corona, core-core interactions.

A further recent step in the understanding the microgel effective interaction in bulk is constituted by the Multi-Hertzian model [75]. This phenomenological approach starts from the assumption that a microgel cannot be represented by a homogeneous elastic sphere. Rather, as previously reported, it is made of a more compact core and of fluffier outer shells. The Multi-Hertzian model thus differentiates between core, corona and dangling chains associating to each of these components a different elasticity and thus a different Hertzian strength. This model is able to fit the simulation outcomes, as reported in Fig. 4.2, where the three Hertzian contributions are also evidenced. Therefore, the complexity of the particle is described by an equally complex interaction potential.

In this Chapter, we present the calculation of both the effective interactions between two microgels at a liquid-liquid interface and their individual elastic properties, using this knowledge to predict their multi-particle response at high densities. Our approach relies on the model for microgel at interfaces presented in the previous Chapter. All the parameters that define the surface tension and the microgel-solvent interactions are left unchanged: the only modification in the model is that we will consider two microgels, one next to the other, for the calculation of the effective potential.

Despite the complex arrangement of the polymer network at the interface and the intrinsic presence of a core-corona structure, the calculation of the effective

interactions between two microgels on the interfacial plane reveals a remarkable agreement with the 2D expression of the Hertzian model for elastic disks for all investigated distances and crosslinker concentrations c . This is clearly different from what was found for the same system in bulk conditions [211] and establishes the validity of the two-dimensional Hertzian model for microgels at interfaces up to large compression regimes. The Young's modulus determined from the effective potential is also directly compared to explicit calculations based on elasticity theory for small and intermediate deformations. Thanks to this method we are able to achieve a full characterization of the elastic response of the microgels in the two-dimensional interfacial plane and we can thus establish a sound comparison to the three-dimensional bulk case. In this way, we will highlight the role of the interfacial tension on the microgel polymer chains.

Having determined how such complex particles interact with each other, we are finally able to carry out our study also at the collective level by investigating the dynamical phase behavior of an ensemble of these effective elastic disks. When softness and elasticity are taken into account in the interparticle interaction a rich behavior is, in general, expected [25, 26, 212]. In particular, we find the presence of multiple reentrant melting phenomena, where a glass is melted simply by an increase in particle concentration. Although similar findings have long been predicted for simple soft models [213], here, for the first time, such scenario is found for microscopically-motivated effective interactions and, most importantly, for potential parameters that can be realized in experiments.

4.1 Effective interaction potential

The two-body effective potential $V_{\text{eff}}(r)$ between the microgels at a water/hexane interface is evaluated by means of extensive simulations in explicit solvent exploiting the Umbrella Sampling technique [11, 214, 215]. This method allows to uniformly sample all distances between the centers of mass of the microgels by adding a harmonic potential between them. For each sampled window i , we evaluate the probability distribution $P(r, \Delta_i)$ of finding the microgels' centers of mass at distance r given the equilibrium length of the spring Δ_i . The final probability for the entire range of explored distances is obtained by first removing

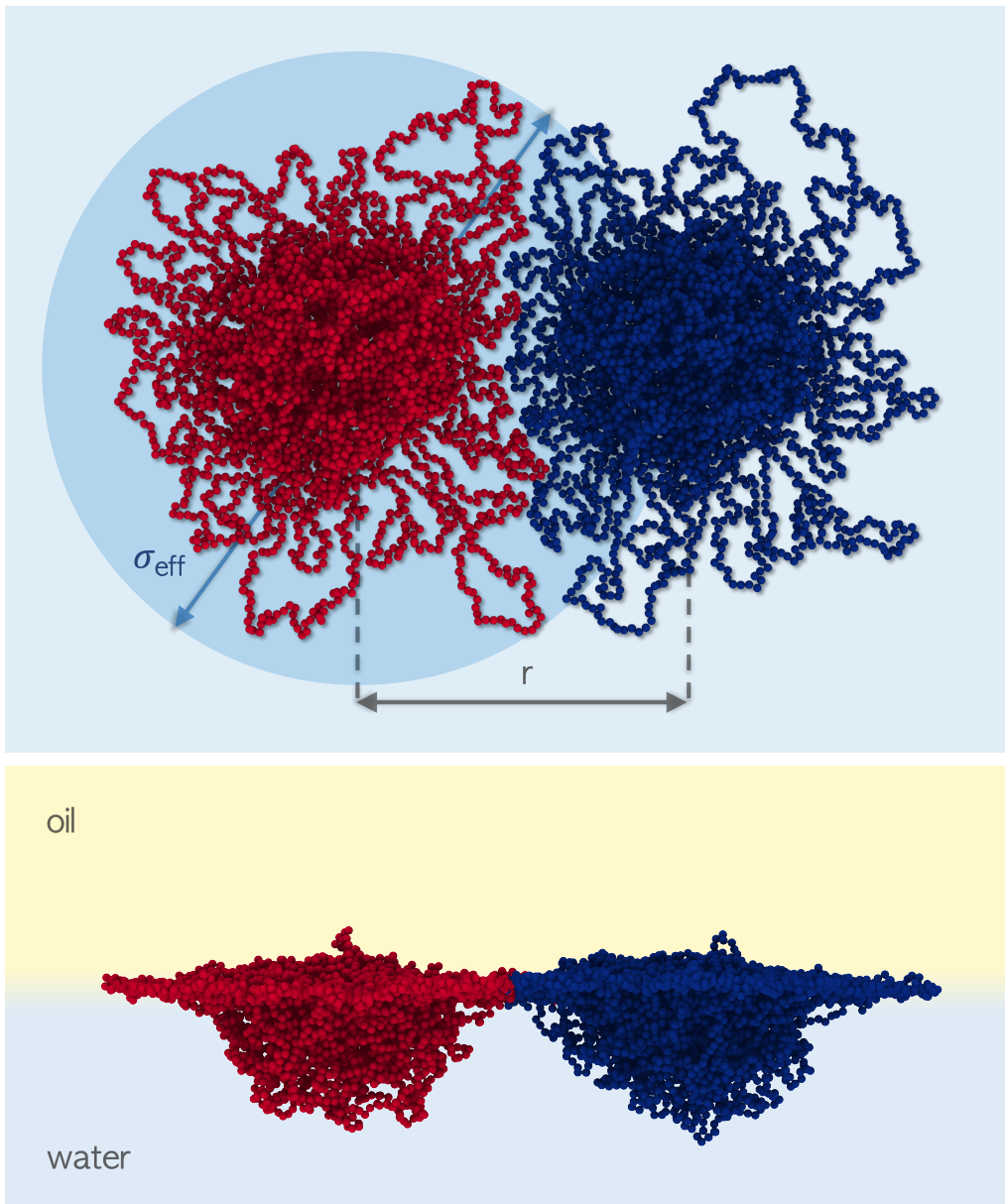


Figure 4.3: Microgels interacting at the interface. Top and side simulation snapshots of two microgels with $c = 5\%$ at the water-oil interface at a representative distance $r \approx 40\sigma$. The effective diameter of the microgel is σ_{eff} . Solvent particles are not shown for clarity.

the contribution of the bias potential and by subsequently merging $P(r, \Delta_i)$ into $P(r)$ for all the windows *via* a least-square method. Finally, the potential of mean force V_{eff} is retrieved knowing that

$$V_{\text{eff}} = -k_B T \ln(P(r)) + C, \quad (4.2)$$

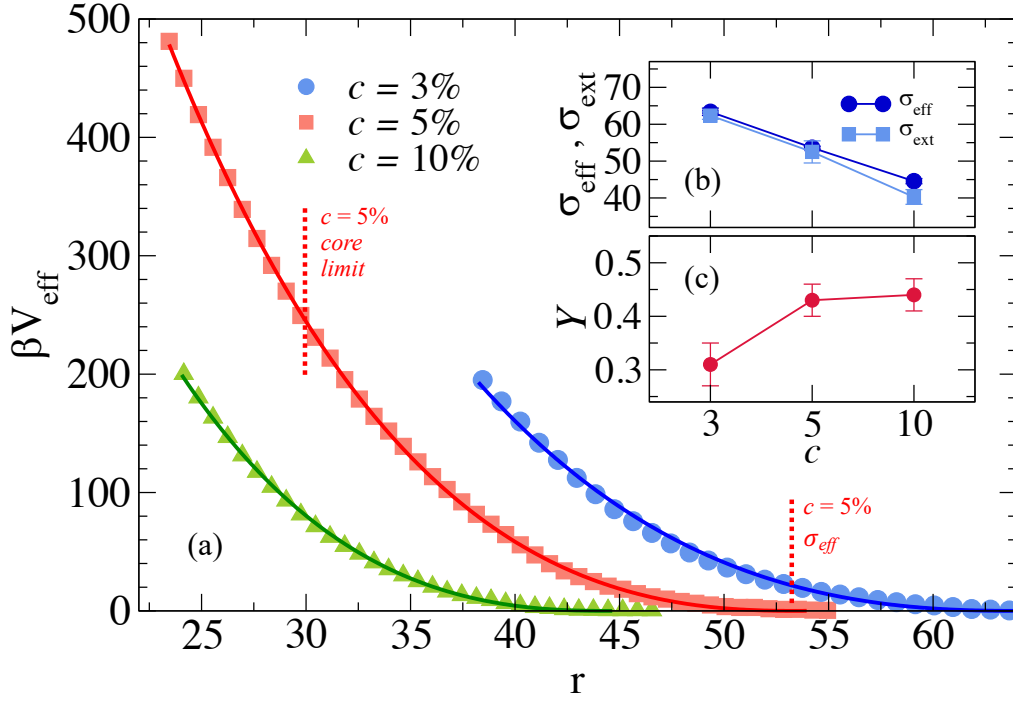


Figure 4.4: Effective potentials for microgels at the liquid-liquid interface and related 2D Hertzian fit parameters. (a) Numerical results refer to three values of the crosslinker concentrations c : 3% (circles), 5% (squares) and 10% (triangles). Full lines are fits to numerical results using Eq. 4.3. The two vertical dotted lines indicate the value $\sigma_{\text{eff}} \approx 53\sigma$ and the distance at which the cores of the two microgels get in contact ($r \approx 30\sigma$) for $c = 5\%$; (b) microgel effective diameter σ_{eff} compared to the extension on the plane of the interface σ_{ext} calculated as in Ref. [126], in units of σ ; (c) Young's modulus Y extracted from the 2D Hertzian fit to V_{H} in units of $k_B T / \sigma^2$.

where C is such that $V_{\text{eff}}(r \rightarrow \infty) = 0$.

For two microgels adsorbed at the interface, this is shown in Fig. 4.4(a) for all investigated values of c , rescaled by $\beta = 1/k_B T$. The numerical results are compared to the two-dimensional Hertzian expression [216, 217] that reads as

$$V_{\text{H}}(r) = \frac{\frac{1}{2}\pi Y \sigma_{\text{eff}}^2 \left(1 - \frac{r}{\sigma_{\text{eff}}}\right)^2}{\ln\left(\frac{2}{1 - \frac{r}{\sigma_{\text{eff}}}}\right)} \quad (4.3)$$

where r is the distance between the centers of mass of the microgels at the interface, σ_{eff} quantifies the effective microgel diameter on the interfacial plane and Y is the Young's modulus of the individual particle. The agreement between the numerical results and the theoretical fits is remarkable for all probed distances and all studied values of c . Therefore, it clearly emerges from these findings that

two microgels confined at an interface effectively behave as 2D elastic objects, further confirming the soft repulsive nature of their mutual interactions.

In principle, this repulsive behavior can be reproduced by other functional forms of the interaction potential. For instance, we could consider a gaussian functional form, that was used to describe brush-coated spherical nanoparticles in bulk [218, 219] and at an interface [179]. Such a simple model can be written as

$$V_{\text{gaussian}}(r) = b \exp(-d(r - e)^2) \quad (4.4)$$

where b , d , e are fitting parameters and r is the distance between the centers of mass of the particles. From a structural perspective, the conformation that microgels retain at interfaces may resemble the one of such particles, given the presence of extended, flexible polymer chains surrounding a more compact core. For polymer brushes, there exists a scaling theory for the fitting parameters b and d [219]. Surprisingly, the functional form in Eq. 4.4 was found to describe the calculated interactions for these systems quite well. Nonetheless, there should not be any physical reason for this framework to be applicable to our system. In addition, the gaussian fit does not account for any deformation of the polymer at the interface, being developed for 3D bulk systems.

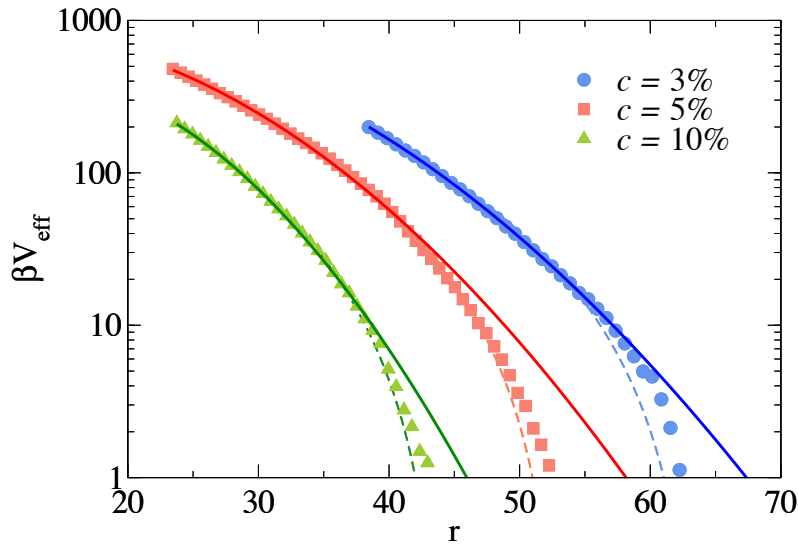


Figure 4.5: Effective potentials for microgels at an interface and gaussian fit. Symbols are simulation results, full lines are fits according to Eq. 4.4 and dashed lines are fits according to Eq. 4.3 (2D Hertzian fits).

4.1 Effective interaction potential

$c(\%)$	b	d	e
3	910	0.002	12.7
5	871	0.003	8.5
10	462	0.005	18.0

Table 4.1: Gaussian fit. Fitting parameters according to Eq. 4.4.

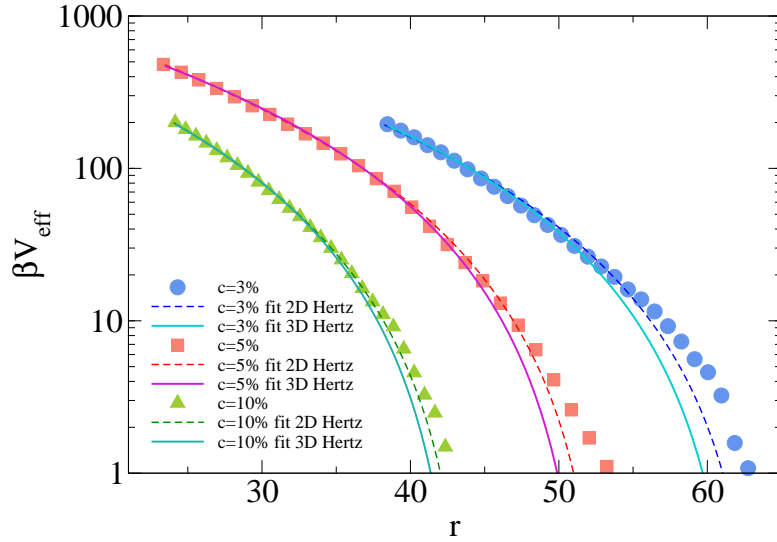


Figure 4.6: Comparison of other fits to the effective potentials. For the three values of crosslinker analyzed, we compare the fits of the numerical data (symbols) by using a 2D Hertzian (dashed lines) and a 3D Hertzian potential (solid lines).

We report in Fig. 4.5 our calculated potentials and the corresponding fits with Eq. 4.4 and with the 2D Hertzian model previously shown in Fig. 4.4. We find that the latter agrees much better with data also at large distances between the microgels, while the gaussian form fails in this regime. Although this is the region in which data are most affected by statistical noise being the probed energy of the order of a few $k_B T$ s, the gaussian fit would give rise to a potential which tends to zero at distances that are clearly non-compatible with the dimensions of the microgel particles analyzed here (see also the comparison with σ_{ext} in Fig. 4.4(b)). While we could think of operating the gaussian fit in a reduced region of distances, *i.e.* only for short ones, it is important to stress that the parameters that we would extract from such fits cannot be related to any physical feature of our system. For the sake of completeness, the fitting parameters for the gaussian functional form are reported in Table 4.1, where it is evident that in the case of parameter e , we cannot even identify a clear trend as a function of the crosslinker concentration.

4.1 Effective interaction potential

c	U_0	σ	Y_{th}	ν_{th}	σ_{ext}	U_0^{th}
3	2065	62.6	0.11	0.09	62.3	3575
5	2078	52.4	0.18	0.1	52.5	3507
10	1454	43.7	0.72	0.17	40.3	6470

Table 4.2: Comparison of 3D Hertzian fit parameters to theoretical values. The 3D Hertzian potential U_0 and σ are compared with the corresponding strength estimated from theory U_0^{th} and with the calculated extension σ_{ext} .

Given the quasi-2D nature of the adsorbed microgels, it is also interesting to compare the simulation data to the 3D version of the Hertzian potential. We thus fit the effective potentials with Eq. 4.1 using as free parameters U_0 and σ . The resulting values, shown in Table 4.2, can be compared to $U_0^{th} = \frac{2Y_{th}\sigma_{ext}^3}{15(1-\nu_{th}^2)}$ where Y_{th} and ν_{th} are the moduli extracted from elasticity theory calculations (see below), while σ_{ext} is the extension of the microgel on the plane of the interface. In Fig. 4.6 we observe not only that the quality of the fits is worse with respect to the 2D model but, most importantly, we find that, while the value of σ remains plausible, there is a strong discrepancy between the estimated U_0 and the corresponding theoretical prediction U_0^{th} . These results clearly indicate the inadequacy of the 3D Hertzian potential in describing the simulation data.

We thus conclude that the 2D Hertzian description is the most appropriate to treat the effective interactions between microgel particles at an interface.

Experimentally, small microgels – having a diameter $\lesssim 200$ nm – are the best candidates to interact as a 2D Hertzian, since they do not experience long-range attractions due to capillary effects [130]. Indeed, the latter have been widely reported [138, 220, 221] and found to be relevant only for microgels large enough to induce a local deformation of the water/oil interface [130]. By contrast, our solvent modeling is aimed essentially at reproducing the surface tension and the microgels solubility, both of which have a direct influence on the conformation of the particle. We can thus directly probe the elastic interactions between the microgels without the interference of attractive capillary forces.

These outcomes also evidence the presence of a single characteristic length in the potential up to a center-to-center distance as small as the interaction radius of the microgel ($\sim \sigma_{eff}/2$) for the case $c = 5\%$, which we have probed up to a repulsion of $\approx 500k_B T$. The observed behavior is strikingly different from the

corresponding bulk one, as described above. Indeed, in bulk, the distinction between core and corona imposes to consider different kind of interactions, depending on the investigated distances [75], that would describe different inner regions of the particle with changing elastic properties. Instead, at an interface, the microgel behaves as if the polymer network were more homogeneous and uniform, as indicated by the continuous and steady growth of the potential that persists even inside the core region, here corresponding to $r \lesssim 30\sigma$ for $c = 5\%$, as also reported in Fig. 4.4(a). This behavior suggests a dominant role of the surface tension which completely controls the properties of the microgel at the interface, so that even the part of the core that protrudes from the plane of the interface effectively contributes to the 2D Hertzian description. Thus, microgels adsorbed at interfaces represent the first colloidal system to behave as an ideal Hertzian model, when considered as two-dimensional objects on the interfacial plane.

By fitting the calculated potential with Eq. 4.3, we can obtain the effective diameter σ_{eff} of the flattened microgel and its Young's modulus Y . Interestingly, the latter quantity can be also directly estimated from the fit of the calculated potentials, at odds with the corresponding 3D case where two non-independent elastic parameters, namely Y and the Poisson's ratio ν , are contained in the Hertzian prefactor, see Eq. 4.1. The resulting fit parameters are shown in Fig. 4.4(b-c). In particular, the effective diameter is found to be very close, at all c , to the microgel extension σ_{ext} , displayed in Fig. 4.4(b), that can be estimated by taking opposite edges of the microgel on the interfacial plane [126]. The slight underestimation of σ_{ext} as compared to σ_{eff} is associated to the fact that effective interaction calculations are also sensitive to the outer dangling chains. This information is partially lost by averaging over the distance of all opposite sites on the plane of the interface. As expected, the extension of the microgel at the interface decreases as a function of c in agreement with experiments [126], since softer microgels deform more strongly, and hence spread more at the interface. The corresponding values of Y are reported in Fig. 4.4(c), showing that higher crosslinking leads to stiffer networks, following expectations and in agreement with findings for microgels in bulk (see also below) [211].

4.2 Elasticity theory calculations

The estimate of the Young's modulus extracted from the fit can be compared to the one obtained through the use of elasticity theory in 2D. Within this theoretical approach, we can calculate all the elastic moduli of a microgel from equilibrium simulations of single particles, as explained in the following.

4.2.1 Assessment of the elastic moduli

The approach employed hereafter has been used for the first time in the calculation of the elastic properties of virus capsids and subsequently of microgel particles in bulk [211, 222]. For the case being, this is based on the evaluation of the area and shape fluctuations of the microgel on the plane of the interface whose distributions are then linked to the elastic moduli. These will refer to the two-dimensional projection of the microgel on the interface, assuming that they are dominated by corona fluctuations. The shape of the microgel on the interfacial plane is studied by building the two-dimensional convex hull, that is the smallest convex set of points that encloses the microgel. At this point, for each configuration, it is possible to diagonalize the gyration tensor of this new set of points and obtain the semi-axes s_1 and s_2 of the ellipse that enclose microgel. The advantage of this procedure is related to the fact that it does not depend explicitly on the mass distribution of the microgel (which, especially in the outer shells, is heterogeneous) and should thus provide more accurate estimates.

The fluctuations in shape for a microgel configuration are evaluated via the strain tensor $\mathbf{C} = \mathbf{F}^T \mathbf{F}$, where \mathbf{F} is the deformation gradient tensor which quantifies the local deformation of a given object [223]. This is defined with respect to a reference configuration which in our case is taken as the configuration whose semi-axes are $\langle s_1 \rangle$ and $\langle s_2 \rangle$, where $\langle \cdot \rangle$ denote an ensemble average. In this way,

$$\mathbf{C} = \begin{pmatrix} \left(\frac{\langle s_1 \rangle}{\langle s_1 \rangle} \right)^2 & 0 \\ 0 & \left(\frac{\langle s_2 \rangle}{\langle s_2 \rangle} \right)^2 \end{pmatrix} = \begin{pmatrix} \lambda_1^2 & 0 \\ 0 & \lambda_2^2 \end{pmatrix}$$

and its invariants are

$$J = \sqrt{\det \mathbf{C}} = \sqrt{\lambda_1^2 \lambda_2^2} \quad (4.5)$$

$$I = \text{tr } \mathbf{C}/J = (\lambda_1^2 + \lambda_2^2)/J. \quad (4.6)$$

Following Ref. [224], the elastic energy U of a two-dimensional object can be written as a function of the invariants J and I of the strain tensor as

$$U(J, I) = U_0 + W(J) + W(I) \quad (4.7)$$

where U_0 is the energy of the reference configuration. The particular choice of W as a function of J and I depends on the specific elastic model employed. Here, we considered the Mooney-Rivlin model, which is known to be valid also beyond the linear elastic regime, for which the elastic energy reads [222, 223]

$$U(J, I) = U_0 + \frac{S}{2} [K(J - 1)^2 + G(I - 2)]. \quad (4.8)$$

with $S = \pi \langle s_1 \rangle \langle s_2 \rangle$, K the bulk modulus and G the shear modulus.

The function W in Eq. 4.7 can be approximated with the potentials of mean force [222]

$$W(X) = -k_B T \ln P(X) + D \quad (4.9)$$

with $X = J, I$, $P(X)$ is the respective probability distribution and D an arbitrary constant. Thus, for each configuration, we evaluate $P(J)$ and $P(I)$ which are then fitted to functions of the form

$$f(X; M_X, X_0, \gamma, C) = M_X (X - X_0)^\gamma + C \quad (4.10)$$

with $\gamma = 2$ when $X = J$ and $\gamma = 1$ when $X = I$, to obtain M_J and M_I . As an example, this procedure is reported in Fig. 4.7 for microgels with $c = 10\%$.

Combining with Eq. 4.8, the first two elastic moduli are readily obtain as

$$K = \frac{2M_J}{S} \quad (4.11)$$

$$G = \frac{2M_I}{S}. \quad (4.12)$$

It is interesting to observe that K , being a measure of the resistance of an object upon compression, is linked to a change in volume as indicated by the invariant J . On the other hand, the second invariant expresses a variation of the

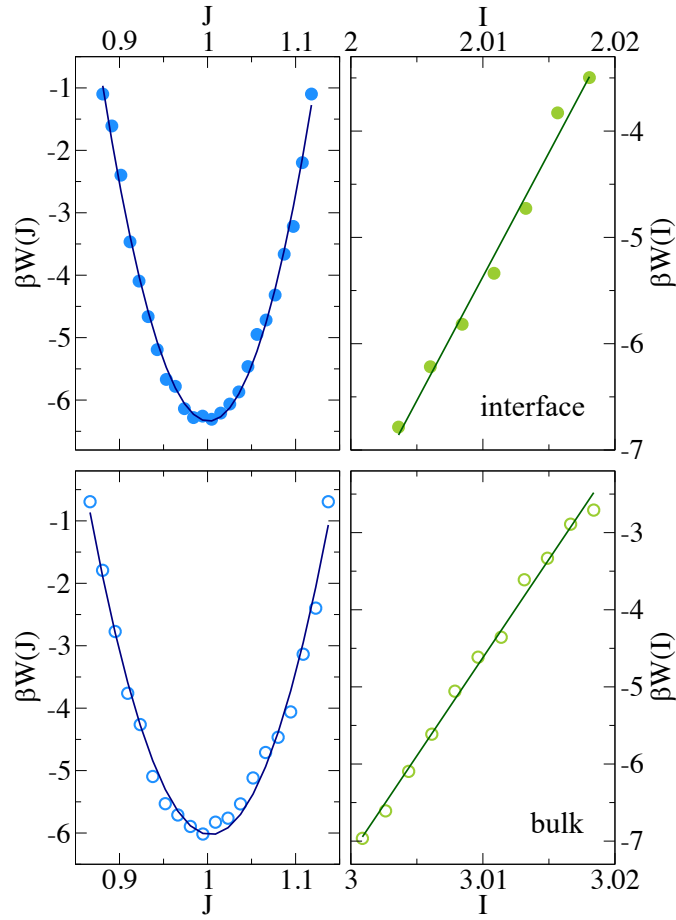


Figure 4.7: Potential of mean force $W(J)$ and $W(I)$ for a microgel at the interface and in bulk for $c = 10\%$. Symbols are simulation data (interface, upper panels; bulk, lower panels) and full lines are fits according to Eq. 4.10.

shape at fixed volume, being in fact connected to the shear modulus G . Y and ν only depend on K and G as [225]

$$\nu = \frac{K - G}{K + G} \quad (4.13)$$

$$Y = \frac{4KG}{K + G} \quad (4.14)$$

The Young modulus is a measure of the overall stiffness of a given material, and constitutes the proportionality constant between applied stress and strain; the Poisson's ratio, instead, quantifies the tendency of an object to deform in a given direction, provided a stress is applied in the normal direction [226]. Similar

expressions can be derived for the 3D case and can be found, for instance, in Ref. [211].

Regarding the specific choice of U , we have further checked that the obtained results do not crucially depend on the specific form of the employed W . To this aim, we also employed the linear elastic model (Hookean) [223, 227] and the Saint-Venant-Kirchhoff model [228, 229], finding results for the moduli, particularly the Young's modulus, that are very close to the ones presented hereafter. They display the same increase with respect to the bulk model and a similar monotonic increase with c .

4.2.2 Interfacial and bulk elastic moduli

Following the protocol just explained, we thus compute the 2D elastic moduli for a microgel at the interface. In order to compare with the corresponding bulk properties, we also perform a similar procedure in 3D for the same microgel topologies in the presence of explicit solvent. However, bulk and interfacial moduli are naturally given in different units. To convert the 2D moduli into 3D ones, we consider that for two-dimensional objects the stress normal to the interfacial plane is zero, the so-called plane-stress conditions [226, 230]. In this way, there exist relations to convert 2D moduli into 3D ones, by assuming that the 2D object has a given (small) thickness h :

$$G^{(3)} = G^{(2)}/h \quad (4.15)$$

$$Y^{(3)} = Y^{(2)}/h \quad (4.16)$$

$$K^{(3)} = \frac{4G^{(2)}K^{(2)}}{3h(3G^{(2)} - K^{(2)})}, \quad (4.17)$$

where $X^{(3)}$ indicates the converted 3D moduli (in units of $k_B T/\sigma^3$) from the 2D results $X^{(2)}$ (in units of $k_B T/\sigma^2$) with $X = G, Y, K$. Also, we have that [230]

$$\nu^{(3)} = \nu^{(2)}. \quad (4.18)$$

In our case, we consider h to be roughly equal to the monomer size, σ , as in the outer shells chains do not pile up, but remain confined to the interfacial plane,

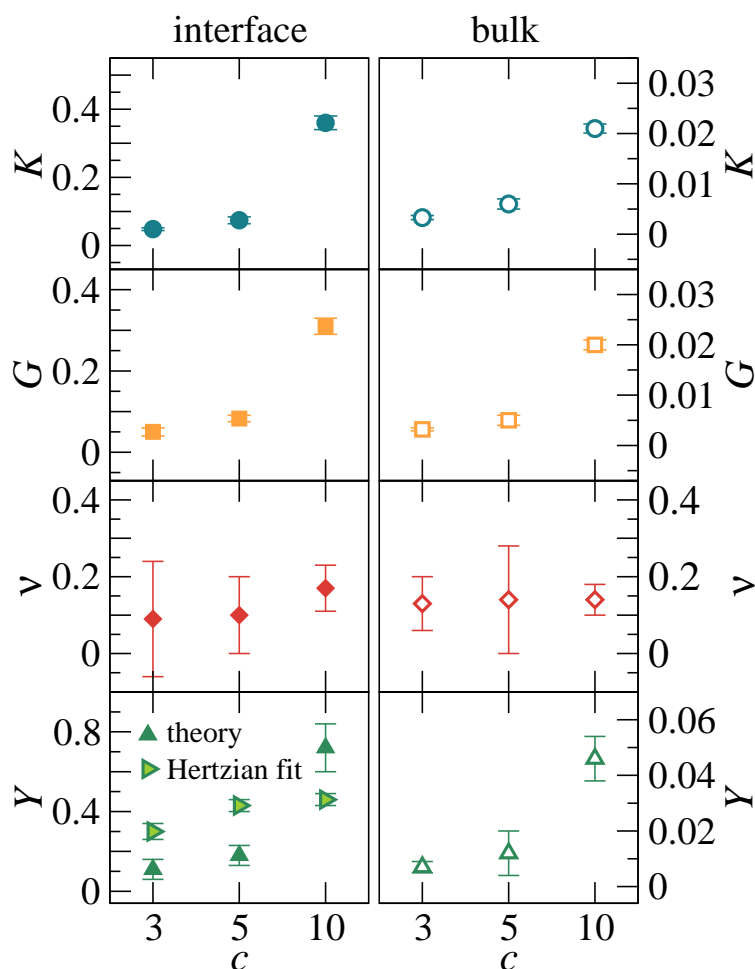


Figure 4.8: Elastic moduli at the interface and in the bulk. Bulk modulus K , shear modulus G , Poisson's ratio ν and Young's modulus Y for the same microgel topology at the interface (full symbols) and in bulk (empty symbols) with explicit solvent as a function of c . In the last row, the theoretical results for Y are also compared to the ones obtained from the effective potential fits with the Hertzian model (Eq. 4.3), also reported in Fig. 4.4(c). K , G and Y are in units of $k_B T / \sigma^3$ to appropriately compare bulk and interface moduli, where the latter are divided by the thickness of the shell at the interface ($\approx \sigma$); ν is dimensionless. Error bars estimated from the fits of $P(J)$ for K and $P(I)$ for G are propagated in the calculation of ν and Y .

providing the dominant contribution to the elastic response of the microgels. Furthermore, as previously reported in Chapter 3 based on AFM studies, the realistic width of a microgel corona is below 7 nm, that is a fully compatible size to the one we extract for a single *in silico* microgel monomer by comparing the form factors of numerical and laboratory microgels [174], as shown in Chapter 1.

The resulting elastic moduli are reported in Fig. 4.8 as a function of the crosslinker concentration both for microgels at interfaces (left panels) and in

bulk (right panels). Overall, we observe a monotonic increase of K , G and Y as a function of c , while ν remains nearly constant. We note that the non-linear dependence of G and Y on c is to be expected, since the chains are not Gaussian and the network contains both dangling ends and loops [231, 232]. These trends are preserved both in the bulk and at the interface. We stress that our two independent estimates of the Young's modulus, namely the one provided by the Mooney-Rivlin theory and that obtained by the 2D Hertzian fitting, also reported in Fig. 4.8, are consistent with each other. We highlight in this way how the single-particle properties of a microgel at an interface are fully reflected in the multi-particle behavior. The most striking result of this analysis is the fact that all three moduli at the interface are significantly larger, by approximately one order of magnitude, than their respective bulk counterparts. As for the Poisson's ratio, even though we find similar values in both cases, it should be noted that its upper limit in 2D is 1.0 while in 3D is 0.5 [225].

These findings provide a robust evidence of the reduced flexibility of the microgels at a liquid-liquid interface, an issue that up to now has either been extracted from indirect results or sometimes related to charge effects [233, 234]. Instead, we directly prove that it is entirely attributable to the presence of the interface, where microgels assume a much more stretched configuration with respect to their standard arrangement in bulk. We are able to establish this link thanks to the relative simplicity of our model, whereby a neutral microgel spontaneously adsorb at the interface without any externally-imposed confinement. Under these conditions, microgels are much more resistant to deformation. Indeed, the corona is completely extended and restrained at the interface with the polymer chains being much less responsive to external forces than in bulk, while still minimizing the surface tension. We further note that no available experimental results have so far reported the lateral elastic response of the microgels on the interfacial plane but rather the perpendicular one over a solid substrate [102]. The lateral response is supposed to be the relevant one for the formation of thin microgel layers or for pattern formation on surfaces [235].

4.3 Multi-particle dynamical response

The level of coarse-graining adopted up to now has allowed us to describe how the properties of single constituents affect their mutual interactions. Now we go one step further by investigating the multi-particle behavior, *i.e.* the condition where many microgel particles interact on the interfacial plane. To shed light on this aspect, we simulate a system of particles whose interaction potential is the one we extracted previously, that is the 2D Hertzian potential. In this way, by further coarse-graining our system, we are able to assess for instance the dynamical response of microgels that are adsorbed on the interfacial plane.

The research on the phase behavior of soft colloids has recently gained much interest: being the archetype potential to describe interactions among elastic particles, the Hertzian phase diagram has been studied both in three [213, 236] and in two dimensions [237, 238]. Some studies evidenced the presence of multiple crystalline phases accessible at low temperatures as the density of the system increases. Others showed the formation of soft quasicrystals in a high-density 2D system consisting of monodisperse isotropic particles interacting via a simple Hertzian-like potential which does not contain explicit multiple length-scales to stabilize such structures. In the two dimensional studies, however, the investigations that have been carried out were limited to a change in the value of the exponent of the well-known 3D Hertzian without considering that a variation in the dimensionality of the problem implies a change in the functional form itself. Indeed, the logarithmic correction arising in Eq. 4.3 cannot be properly captured by a simple variation in the Hertzian exponent.

The phase behavior of the 2D Hertzian potential is assessed by means of molecular dynamics simulations in two dimensions with 5000 particles of unit mass m and diameter σ_{eff} , interacting *via* Eq. 4.3. We use σ_{eff} as the unit of length, so that the area fraction is defined as $\phi = \frac{\pi}{4} \langle \sigma_{\text{eff}}^2 \rangle \rho$, with ρ the number density. We fix $k_B T = 1$, which defines the unit of energy, *via* a Langevin thermostat. In order to have access to the dynamical response, we avoid crystallization by setting the polydispersity to $p = 0.2$. We analyze a range of ϕ from 0.8 to 2.8 for a 2D Hertzian strength, defined as $A = \pi Y \sigma_{\text{eff}}^2 / (2 \ln 2)$, that goes from 220 to $1150 k_B T$. We note that A has units of energy over length squared, meaning

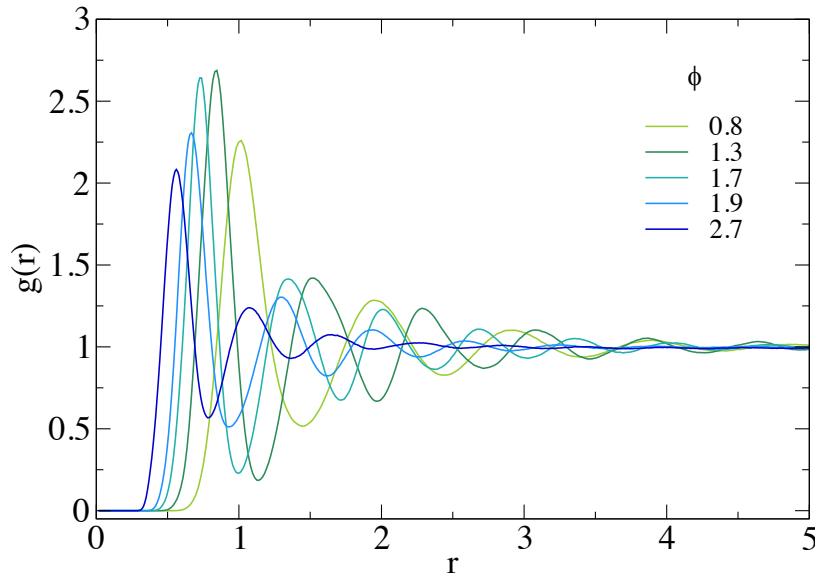


Figure 4.9: Radial distribution function. Pair correlation function $g(r)$ as a function of the distance r (measured in units of σ), for some representative packing fractions ϕ at Hertzian strength $\approx 680k_B T$ for $p = 0.2$.

that it changes value depending on the units of measurement used (σ and σ_{eff} for the monomer-resolved system and the coarse-grained systems, respectively). For all ϕ and A , we monitor the presence of a liquid-like disordered structure by calculating the radial distribution function. As an example, this is reported in Fig. 4.9 for an intermediate value of the Hertzian strength. Representative simulation snapshots are instead shown in Fig. 4.10.

To determine the glass region in the 2D phase diagram, we run simulations for $\sim 2 \times 10^7$ timesteps and we calculate the mean-squared displacement $\langle \Delta r^2 \rangle$ of the particles (see Fig. 4.11), extracting the long-time self-diffusion coefficients D :

$$D = \lim_{t \rightarrow \infty} \frac{\langle \Delta r^2 \rangle}{4t} \quad (4.19)$$

where t is the simulation time. Since we are only interested in providing a state diagram assessment, we do not perform an extensive characterization of the glassy dynamics of the system and we just monitor the onset of non-ergodicity within the timescale of our simulations. We attribute this condition to state points where we find $D \lesssim 2.5 \times 10^{-5}$, roughly three orders of magnitude lower than the

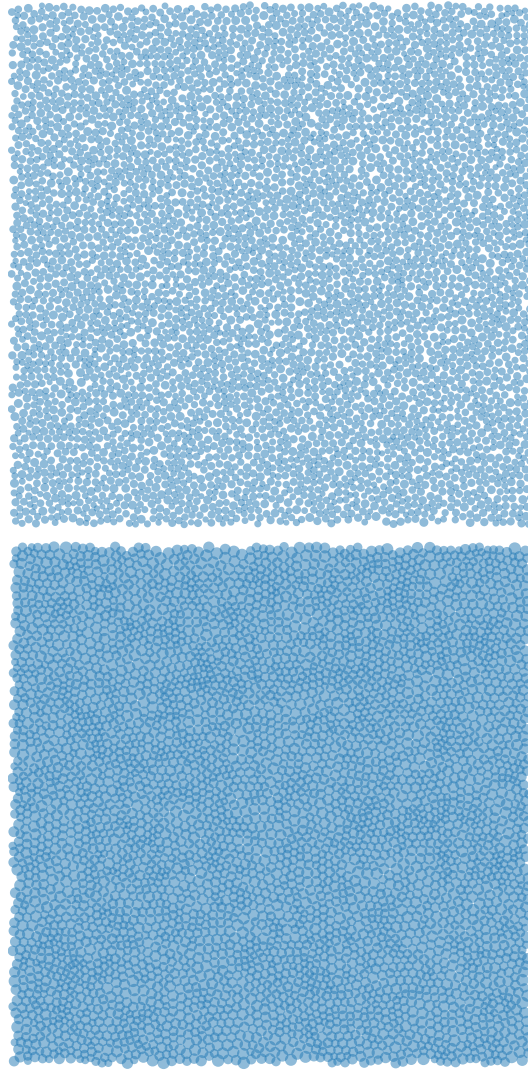


Figure 4.10: Multi-particle simulations snapshots. Representative snapshots for the multi-particle simulations for (top) $\phi = 0.8$ and (bottom) $\phi = 1.8$ at Hertzian strength $A \approx 680k_B T$.

corresponding low-density value. Under these conditions, the system has become so slow that aging is present within our simulation time window.

It is important to notice that, in our simulations, particles are assumed to have fixed size, differently from bulk conditions where recent simulations and experiments have shown that deswelling plays an important role for concentrated microgel suspensions [81, 85, 239]. Instead, there is no reported evidence of deswelling when microgels are compressed at the interface. This is again due to the dominant role of the surface tension which makes adsorbed microgels much

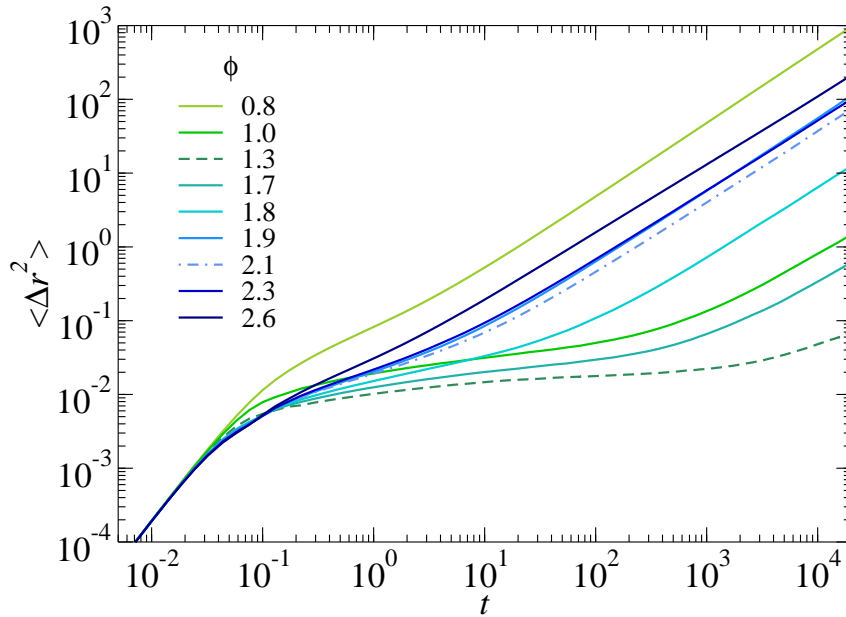


Figure 4.11: Reentrant behavior. Mean-squared displacement of disks interacting with the 2D Hertzian potential for different area fractions ϕ at a representative value of Hertzian strength $\approx 680k_B T$. The dashed line signals the onset of a glass while the dashed-and-dotted line highlights a further slowdown of the dynamics at higher ϕ .

less responsive to external stimuli [128, 195]. In this way, their compression is simply associated with a smooth and monotonic decrease of their interparticle distance, as described experimentally in Ref. [130].

Figure 4.12(a) reports the self-diffusion coefficients D extracted from the long-time behavior of the mean-squared displacements of the effective microgels for different values of ϕ and A . Importantly, we reveal the onset of two clear reentrant melting phenomena where the diffusivity, at first, decreases leading to the formation of a glassy system and then it grows again. This increase takes place primarily for $\phi \gtrsim 1.5$ with a local maximum emerging at $\phi \sim 1.9$. For higher densities, after a further slowdown, the system re-fluidifies again acquiring a finite diffusion coefficient. Interestingly, at the new local maximum appearing for $\phi \sim 2.5$, the value of D is even larger than that at the previous maximum.

Previous works have shown that one can estimate the locus of the glass transition by monitoring the so-called iso-diffusivity (iso- D) lines [240–242], along which D remains constant. Importantly, it has been shown that the iso- D lines always maintain, for not too large values of the probed D , the same shape as the

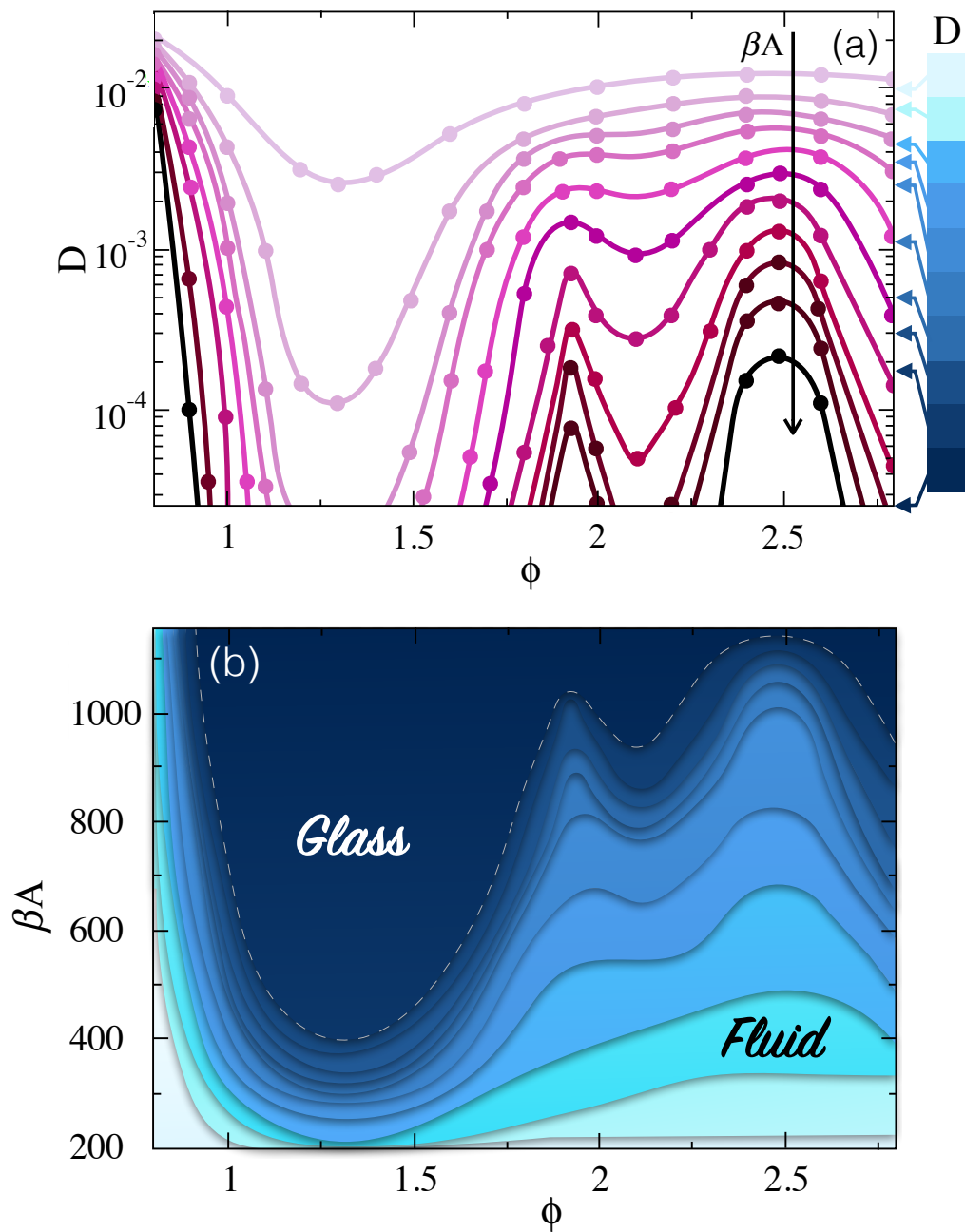


Figure 4.12: 2D Hertzian phase diagram. (a) Diffusion coefficient D as a function of the area fraction ϕ for different values of the 2D Hertzian strength A . From top to bottom, A takes the following values: 226, 340, 409, 453, 566, 680, 793, 906, 974, 1042, 1133 $k_B T$; symbols are simulation data and lines serve as guides to the eye. The lowest reported value of D is taken as the non-ergodicity limit; (b) phase diagram showing βA as a function of ϕ , extracted by taking the iso- D lines from (a). The dashed line signals the onset of the glass region; state-points with the same color-coding have the same value of diffusion coefficient.

ultimate line of arrest. Thus, by extrapolating to the $D \rightarrow 0$ limit, it is possible to locate the glassy region of a system. By taking a set of different isodiffusivity lines in Fig. 4.12(a), we draw the corresponding fluid-glass state diagram for the 2D Hertzian model, shown in Fig. 4.12(b).

We notice that for the present system a fluid-like region persists at high densities for $\beta A \lesssim 1100$. We also stress that similar reentrant features in the dynamics have long been predicted in the three dimensional version of the Hertzian potential [213] and in extensive simulations of monomer-resolved single-chain nanoparticles [243]. This phenomenon is typically linked to the soft nature of the interaction potential that, in contrast to hard-core ones where the packing of the particles is limited by excluded volume interactions, makes it possible to restore long-time diffusive motion at high densities, thanks to a balance between energetic and entropic contributions, as also observed in simulations of the Gaussian core model [244] or of the star polymer potential [241]. Nevertheless, reentrant transitions have never been found in experiments of soft [57] and ultra-soft colloids [245]. While microgels in bulk conditions do not show high-density liquid states due to their deviations from an ideal Hertzian behavior [75, 86], as also confirmed experimentally [57, 83, 246], those at interfaces stand as optimal candidates for displaying such an intriguing dynamical behavior.

Crucially, thanks to the knowledge of the functional form of the potential, we can now predict the experimental features of microgels that will most likely show a reentrant behavior. Indeed, since the repulsive Hertzian strength A depends on the Young's modulus and on the effective diameter of the particles, we need to consider microgels whose combined spreading and elastic properties at the interface fall into the predicted reentrant range. It turns out that we need to focus on microgels with relatively small size, since a reduction of the particle diameter strongly affects the value of the Hertzian strength, which depends quadratically on it. To be more precise, we perform additional simulations of microgels made of 2000 and 3000 monomers, besides those with ≈ 5000 monomers. In order to avoid long computational times for the calculation of the effective interactions, we directly determine the Hertzian strengths *via* elasticity theory calculations and by measuring σ_{ext} for single particles with different sizes and crosslinker

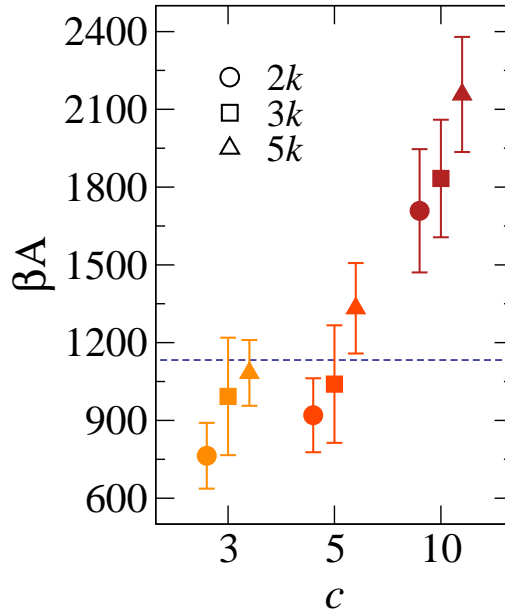


Figure 4.13: Dependence of the 2D Hertzian strength A on the crosslinker concentration for microgels of various sizes. Value of βA are extracted *via* the theoretical calculation of Y and σ_{ext} for microgels assembled with $N \approx 2000$ (circles), 3000 (squares) and 5000 (triangles) monomers for $c = 3\%$ (orange), 5% (red) and 10% (dark red). Symbols are slightly displaced on the x-axis to enhance readability. The dashed line indicates the largest value of the Hertzian strength for which a reentrant transition could be observed (see Fig. 4.12). Data are averaged over four different topologies for each combination of N and c .

concentrations at the interface.

We report the estimated repulsive strengths as a function of c in Fig. 4.13 and find that soft and small microgels have an Hertzian strength that falls in the range where a reentrant behavior of the dynamics is present, according to the phase diagram in Fig. 4.12(b). We also confirm that the value of the Young’s modulus does not exhibit a strong size dependence, especially for $c = 3\%$ and 5% (see Fig. 4.14), in qualitative agreement to experimental findings on microgels of different sizes [247–249]. Hence, from this analysis, we conclude that highly crosslinked microgels will always display glassy dynamics at the interface, independently on their size. Instead, low-crosslinked microgels whose Young’s modulus at the interface is around $0.1 - 0.3k_B T/\sigma^2$ and whose extended size is between $\approx 35 - 50\sigma$ are expected to show a reentrant dynamics. Thanks to the mapping established in Chapter 1 with experiments [126, 174], we are now able to convert these predictions to real values which, for laboratory microgels,

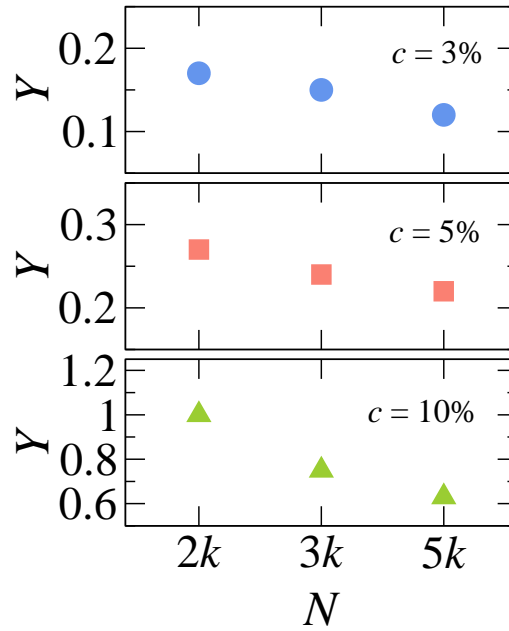


Figure 4.14: Young modulus for different crosslinker concentrations and microgel sizes. Dependence of the Young modulus as a function of $c = 3\%, 5\%, 10\%$ for $N = 2000, 3000, 5000$ microgel monomers at the interface. Data are in units of $k_B T / \sigma_m^2$.

correspond to hydrodynamic diameters in bulk $\lesssim 200$ nm. This value is well within the commonly investigated experimental range and offers the additional advantage that capillary effects should be less relevant. Therefore, adsorbed microgels of small size and low crosslinking ratio constitute a realistic model system to experimentally investigate the presence of a reentrant dynamics, long postulated in the realm of soft colloids.

It is also instructive to think where this regime can be observed in terms of compression isotherms to which experiments typically refer to. From the present calculations, we estimate that the value of the area fraction is reduced by about a half as compared to the corona-corona contact at low densities. Even though these compressions are not too high [130], a number of critical issues may emerge and these are ultimately linked to the real-time visualization of the microgels at the interface, which is essential to retrieve dynamical information from the interfacial microgel assembly and thus observe the reentrant melting at high densities. Currently most of the studies are performed *ex-situ* by means of atomic force microscopy (AFM) on silica wafer or similar techniques, from which only structural static information can be extracted. However, the real-time

visualization is just one of the options for the experimental verification since other approaches could be devised. For instance, one could imagine to put forward a rheological investigation and analyze the response of the microgel ensemble at different packing fractions. Overall, we believe that our predictions will stimulate experimental work to confirm the predicted dynamical behavior for microgels at interfaces.

4.4 Summary

In summary, in this Chapter we have provided the first numerical estimate of the two-body effective interaction potential of microgel particles adsorbed at an interface. The complex arrangement of such particles on the interfacial plane is thus rationalized with a simple functional form that reveals that they interact like effective elastic disks with a Young's modulus that increases with the crosslinker concentration. Notably, the values of the elastic moduli at the interface, after appropriate rescaling, are found to be roughly one order of magnitude higher than the one measured in bulk, as also confirmed by elasticity theory calculation of single microgel particles. This can be attributed to the dominant effects of the interfacial tension, which controls the response of the polymer network to an external stress, making it much stiffer and resistant to deformation with respect to the same network in good solvent conditions. This result has profound consequences on the properties of a generic interfacial assembly of soft colloids, not limited to microgel particles. Indeed, we expect that the reduced mobility of the polymer chains and their enhanced stiffness should be taken into account in the development of novel materials that rely on deformable constituents of any kind. As demonstrated by our results, this effect should be expected at interfacial conditions with large surface tensions, independently of the presence of intrinsic charges in the material or in the fluids. In this respect, our results call for direct experimental verification which could unambiguously shed light on these aspects.

From a more fundamental perspective, we have clearly demonstrated that the knowledge that is gained on the bulk properties of soft colloids cannot be directly transferred to the interface, which should be considered as a completely

separate case, where particles behave and interact in a different way. Indeed, we have here numerically shown that microgels at interfaces follow the Hertzian predictions as 2D objects even at very short separations, well beyond the small-deformation regime. This is in stark contrast to microgels in bulk, where the validity of the Hertzian model was found to apply only up to interactions of the order of few $k_B T$, while model like the Multi-Hertzian are needed where overlaps between particles and deformation start to be probed. This was due to the internal morphology of the microgel, that imposes multiple length scales to be included in the description of the collective behavior. Instead, at the interface, the behavior is completely dominated by the very extended coronas. We can thus state that microgels do have distinct properties depending on the environment in which they are placed, opening up new avenues for their exploitation. A similar scenario should be expected for any soft particle adsorbed at interfaces with respect to the corresponding behavior in bulk conditions.

The extensive analysis of the multi-particle dynamics has further evidenced the emergence of reentrant dynamics, where the system behaves as an ergodic fluid up to very large densities, well above individual particles contact, sometimes loosely called jamming. Experimentally, small (nano-sized) soft microgels appear to be the ideal candidates to verify our theoretical predictions, as indicated by the values of the Young's modulus and of the interfacial extension at which the reentrance is observed. In addition, small colloids are the least likely to experience capillary attractions at the interface, and hence will behave more similarly to the ones we have simulated.

The main Reference for this Chapter is:

- F. Camerin, N. Gnan, J. Ruiz-Franco, A. Ninarello, L. Rovigatti, E. Zaccarelli, Microgels at interfaces as 2D effective particles, *Physical Review X* **10**, 031012 (2020)

Chapter 5

Hollow microgels

Responsiveness is certainly one of the features to which microgels owe their popularity [27]. Especially from an applicative point of view, this has undoubtedly stimulated many chemical and industrial applications. Among these, drug delivery is particularly noteworthy. Indeed, as previously reported, microgels may be designed to respond to a number of external stimuli (including pH, ionic strength, specific ions and metabolites, temperature) and external fields such as light, magnetic fields, and ultrasound [52, 250, 251]. All of these represent means of triggering the release of a certain substance once incorporated in the polymer network. In fact, thanks to their hydrophilicity, proteins and peptide drugs can be enclosed with only moderate conformational changes and limited aggregation, thus preserving the biological activity of the drug. The clearest example comes from the responsivity provided by temperature, in case temperature-sensitive polymer such as PNIPAM or poly(ethylene glycol)-containing polymers are employed. Nolan et al. [252] after encapsulating insulin when microgels are swollen at low temperature noted the drug release on microgel deswelling above the volume phase transition temperature. Other fascinating applications are related for instance to the light-dependent drug release in azo-dextran microgels based on trans-cis isomerization of an azobenzene moiety in the microgel crosslinker [253].

In this context, an important role is played by microgels that have a different topology from the standard core-corona ones. Recently, hollow microgels are in fact receiving much interest as a potential drug delivery system [52, 254]. Contrarily to standard microgels, these are only made of an external shell: being deprived

of an inner dense core, they are the perfect candidate to host macromolecules even allowing to finely control the incorporated amount. In a broad sense, therefore, they can represent an efficient carrier for other molecules, as also demonstrated numerically [255].

Similarly to standard microgels, they may also prove to be crucial to answer fundamental questions in physics. In the previous Chapters, we have shown how the same macromolecule under different conditions can lead to different physical properties simply as a result of a change in its conformation, from the bulk to the interface. It is therefore natural to expect that microgels consisting of a different topology have different and unexpected features to be investigated.

At the moment, there are essentially two different protocols to synthesize such particles, namely the inclusion of a sacrificial core and the use of two different chemically-responsive compounds. In the former case [85], the procedure is similar to the usual precipitation polymerization method which in this case takes place onto silica cores to generate hard core-shell microgels. The silica cores are subsequently dissolved by means of sodium hydroxide, leaving only the external polymer shell. The latter synthetic procedure, initially proposed by Nayak et al. [40], exploits a degradable crosslinker (N,N'-(1,2-dihydroxyethylene)bisacrylamide, DHEA) to synthesize core particles, whereas a nondegradable crosslinker (BIS) is used to add a shell onto the first core-corona microgel. The inner particle is then degraded by addition of sodium periodate, which cleaves the vicinal diol in DHEA. Very recently, Nickel et al. [41] synthesized also hollow microgel particles with an anisotropic shape. In this case, the microgel shell was synthesized onto an ellipsoidal hematite core, which is covered by a silica layer. After polymerization, the core is etched in a two-step procedure. For anisotropic hollow microgels, one could envision a rich phase behavior with complex liquid crystalline-ordering phenomena as compared to rigid isotropic particles.

The properties of hollow microgels can be further enriched by adding charged groups in the network. In Ref. [43] the authors discussed how the size and structure of the cavity of hollow charged microgels may be controlled by varying pH and ionic strength. In particular, it was found that by increasing the pH of the solution, the charges that are present in the polymer network allow to preserve the

size of the cavity. Also, this would allow an enlargement of the cavity compared to that of the same microgels in the uncharged state.

The role of the cavity has also been investigated in one of the few fundamental studies on this system. Scotti et al. [85] made use of experiments and Monte Carlo simulations of a simple model system to determine the role of the microgel architecture in overcrowded environments. By comparing regular and hollow microgels surrounded by a three-dimensional matrix formed by regular microgels, they established that the presence of the cavity leads to a greater deswelling of the particles, with respect to a decrease in the crosslinker concentration. It thus appears that, by exploiting the additional degree of freedom constituted by the internal cavity, hollow microgels can be compressed further than regular microgel particles.

These examples show how this is a field of active research, although basic characterizations have yet to be made. For instance, a relevant aspect concerns the density profiles of these particles which, as it is known, cannot be directly derived from experiments but have to rely on theoretical fitting of the form factors. While in the case of standard microgels the extended-fuzzy-sphere model appears to work quite well as discussed in Chapter 1, here instead unrealistic density profiles are often obtained. Also, the use of techniques that do not assume *a priori* a functional form but are based on iterative fitting procedures for a given form factor [256] seems not to lead to reliable density profiles. A second aspect to be explored is certainly the behavior of these microgels as a function of temperature and shell thickness. In addition to providing useful information from an applicative point of view, this can be relevant to understand the collective response of an ensemble of hollow microgels.

In this Chapter, we thus propose a study aimed at the characterization of single-particle hollow microgels. This will be done using what we have learned for standard microgels, starting from the modeling which takes into account the polymeric nature of the particles. In order to obtain a comprehensive description, we will couple simulations and experiments, the latter again performed by the group of Prof. Lucio Isa at ETH Zurich. This will be particularly useful to obtain a realistic description of the internal distribution of monomers. In fact, we will

compare numerical and experimental form factors in the same way we did for standard microgels in Chapter 1. Once a meaningful comparison is established, we will discuss the density profiles which are directly obtained in simulations. To assess the effects of temperature, we make use of the solvophobic potential V_α . The same procedure is then adopted for microgels with a different shell thickness and the different response is analyzed.

Finally, we study the conformation of hollow microgels at a liquid-liquid interface, for which we expect significant differences with respect to standard microgels due to the absence of the core.

5.1 Characterization in bulk

The *in silico* synthesis of hollow microgel particles is based on that of regular ones, largely discussed in Chapter 1. Usually, two and four folded patchy particles are confined and assembled in a spherical cavity of radius Z (always expressed in units of length σ). In this case, however, we make use of an additional force field which prevents the particles to enter an inner region of radius Z_{in} with $Z_{in} < Z$. In this way, particles are effectively confined in a spherical shell, with the inner force field mimicking the sacrificial silica core or the polymeric core which is subsequently removed. The interactions between patchy particles during the assembly as well as the polymer bead-spring model are not changed with respect to the standard case, whereas we modulate monomer density and designing force acting on the crosslinkers. We stress that such kind of microgels are still largely less investigated with respect to the standard microgels. Thus, it is non-trivial to determine which model could best represent the experimental outcomes.

5.1.1 Dependence of the shell thickness

We start by comparing numerical and experimental form factors of standard microgels with those of hollow microgel particles in the swollen state, with $\alpha = 0$, while in later stage we will consider temperature effects. Experimentally, while the former are obtained via the precipitation polymerization procedure, the latter are obtained synthesizing core and corona with different polymers, as described

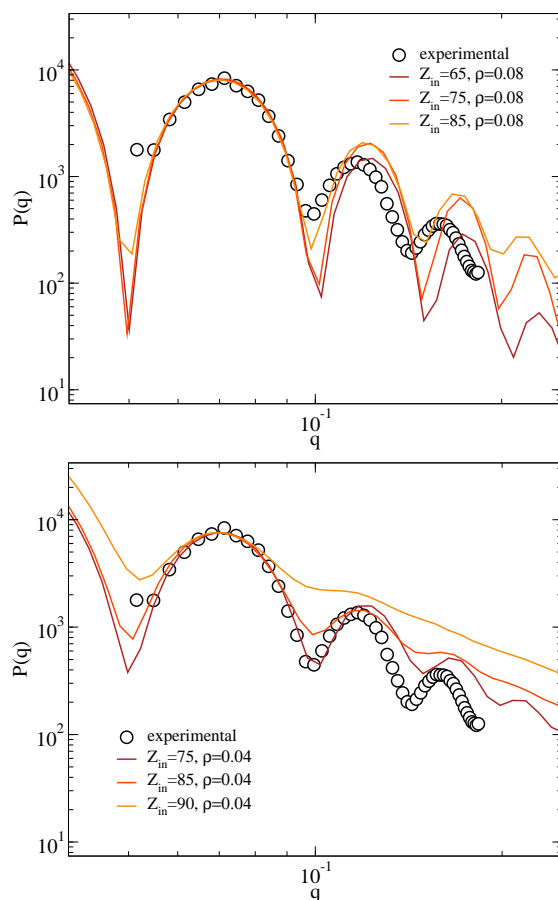


Figure 5.1: Form factors comparison for the thin-shell hollow microgel. Top: form factors at a fixed number density $\rho = 0.08$ and outer radius $Z = 100\sigma$, varying the inner size of the cavity Z_{in} . Bottom: form factors at a fixed number density $\rho = 0.04$ and outer radius $Z = 100\sigma$, varying the inner size of the cavity Z_{in} . Form factors are arbitrarily rescaled in the x and y-axes and compared to experimental outcomes (symbols).

in the introductory section. In particular, PNIPAM and DHEA (10% mol) are used for the inner core synthesis while PNIPAM and BIS (5% mol) are used for the outer shell.

The first microgel we consider (also called *thin-shell* hollow microgel) has a cavity whose diameter is about the 75% of the overall external diameter, according to experimental DLS measures. Numerically, we consider microgels with external radius $Z = 100\sigma$, and we vary other parameters such as the size of the internal cavity and the monomer density, starting from $\rho = 0.08$ used for the modeling of regular microgels [174]. Adopting the same procedure described in Chapter 1, the form factors are compared by superimposing the maximum of the first peak. Some of these comparisons are reported in Fig. 5.1 where we show both numerical

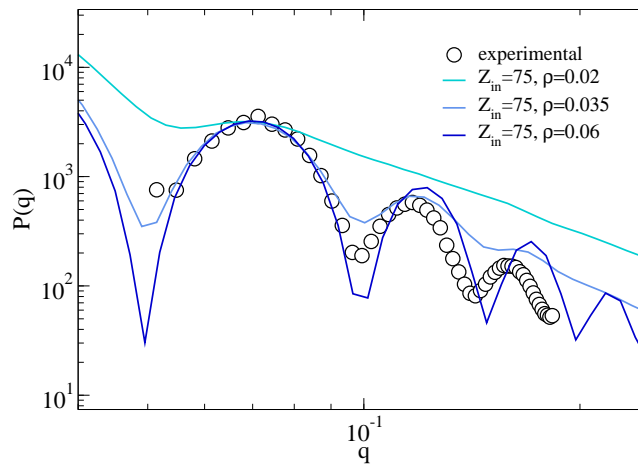


Figure 5.2: Form factors comparison for the thin-shell hollow microgel. Form factors at a fixed inner radius $Z_{in} = 75\sigma$ and outer radius $Z = 100\sigma$, varying the internal density ρ . Form factors are arbitrarily rescaled in the x and y-axes and compared to experimental outcomes (symbols).

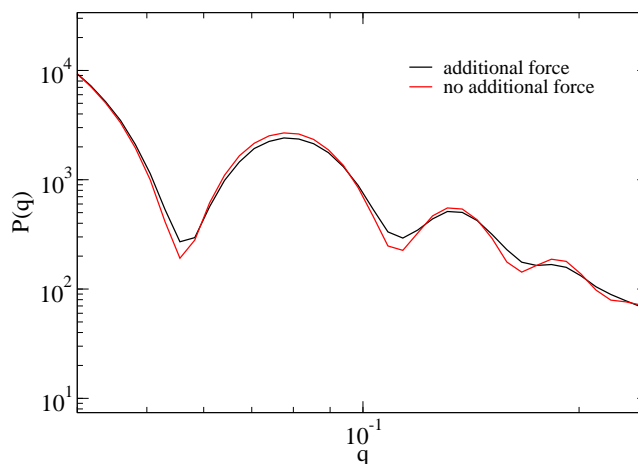


Figure 5.3: Effect of the designing force on crosslinkers for the thin-shell hollow microgel. The form factors of microgels synthesized by adding or not a designing force on the crosslinkers are compared. In particular, we consider the case with $Z = 100\sigma$, $Z_{in} = 75\sigma$ and $\rho = 0.035$. Form factors are arbitrarily rescaled in the x and y-axes.

and experimental form factors. We thus observe how by lowering the internal density and increasing the size of the cavity the agreement with the experimental form factor improves as the peaks become smoother and shift to lower q -values. In Fig. 5.2, we vary the internal density at fixed $Z_{in} = 75$. Therefore, it appears that $\rho \approx 0.035$ best describes the experimental form factor, revealing that the method of synthesis employed generates polymeric shells that are less dense than the average density found for regular microgels. Also, as shown in Fig. 5.3, it

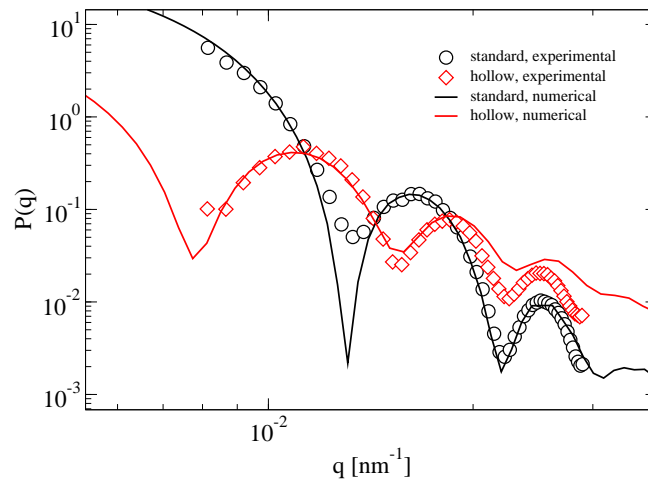


Figure 5.4: Form factors of regular and thin-shell hollow microgels. Comparison of numerical (lines) and experimental (symbols) form factors for regular ($Z = 100\sigma$, $\rho = 0.08$) and hollow microgels ($Z = 100\sigma$, $Z_{in} = 75\sigma$, $\rho = 0.035$). In both cases, $c = 5\%$. Form factors are arbitrarily rescaled in the y-axes.

is important to note that there are no relevant differences between the case in which a designing force is added on crosslinkers and that in which this is not included during the assembly. Minor discrepancies between the two cases could be attributed to different degrees of assembly for the two configurations which should thus be averaged among other microgel realizations. Fig. 5.4 summarizes these results and compare the form factor of a hollow microgel to that of a regular

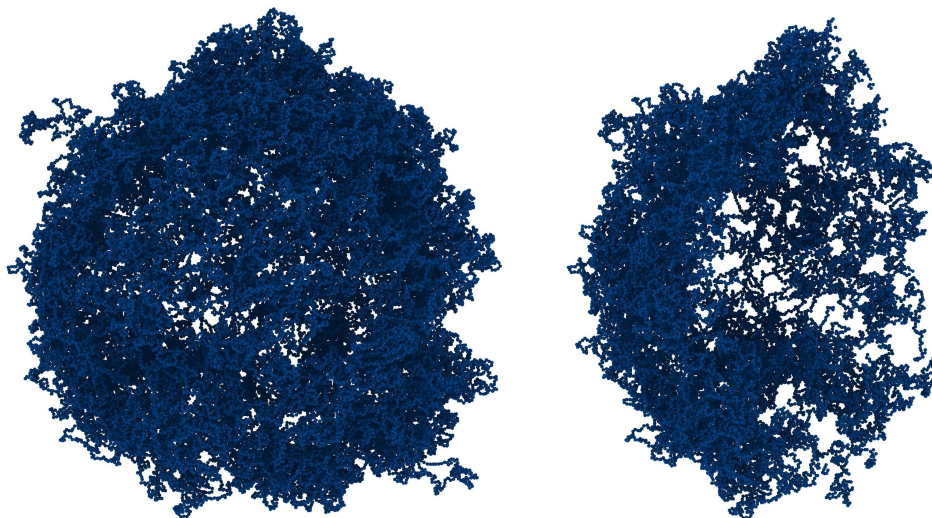


Figure 5.5: Simulation snapshots for the thin-shell hollow microgels. Full hollow microgel with a thin shell (left) and corresponding slice (right).

one. In particular, the same numerical form factor used in Chapter 1 for regular microgels fits the form factor of the regular microgel shown in Fig. 5.4 in a fully satisfactory way, despite the synthesis and the analysis being performed by different operators in different laboratory conditions. In this way, we also confirm the reproducibility of our results. Simulation snapshots of the thin hollow microgel are shown in Fig. 5.5.

We now discuss a second hollow microgel (also called *thick-shell* hollow microgel), whose nominal cavity is half of the total microgel diameter. In this case we

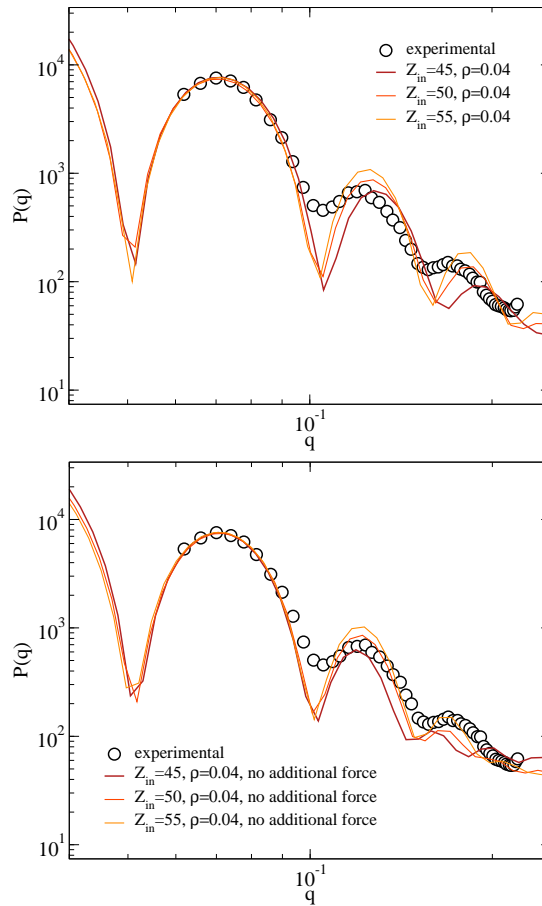


Figure 5.6: Effect of the designing force on crosslinkers for the thick-shell hollow microgel. Top: form factors at a fixed number density $\rho = 0.04$ and outer radius $Z = 100\sigma$, varying the inner size of the cavity Z_{in} ; a designing force is applied on crosslinkers as for standard core-corona microgels. Bottom: form factors at a fixed number density $\rho = 0.04$ and outer radius $Z = 100\sigma$, varying the inner size of the cavity Z_{in} ; no designing force is applied on crosslinkers. Form factors are arbitrarily rescaled in the x and y-axes and compared to experimental outcomes (symbols).

start the analysis from $\rho = 0.04$, which already provides a reasonable description of the experimental data for the thinner hollow microgel. As shown in Fig. 5.6, the presence or not of the additional force on the crosslinkers turns out to be crucial for this microgel. In fact, by comparing the case with and without force for the same density and same inner core radii, in the former condition there is a systematic shift to higher q -values for the second and the third peaks. Next, we consider $Z_{in} = 50$ and vary the internal density around $\rho = 0.04$ (see Fig. 5.7) revealing a constant decrease in intensity especially in the third peak by increasing ρ . Also in this case the model with $\rho = 0.035$ best describes the experimental data.

A final comparison is displayed in Fig. 5.8 where we also report a size assessment, by reducing the overall size of the microgel and the corresponding inner core radius by 25%. In Fig. 5.9, we show two simulations snapshots. The agreement is fully satisfactory for both models, with the smaller microgel presenting a slightly reduced intensity for high q peaks. This is analogous to what observed for standard microgels in Chapter 1 by reducing the number of monomers from $N \approx 330000$ to $N \approx 42000$ and ≈ 5000 . For hollow microgels, the reduction in size reported here is equivalent of reducing the number of particles by almost 2.5 times, from $N \approx 128000$. Smaller hollow particles, *e.g.* with $Z = 50$, would

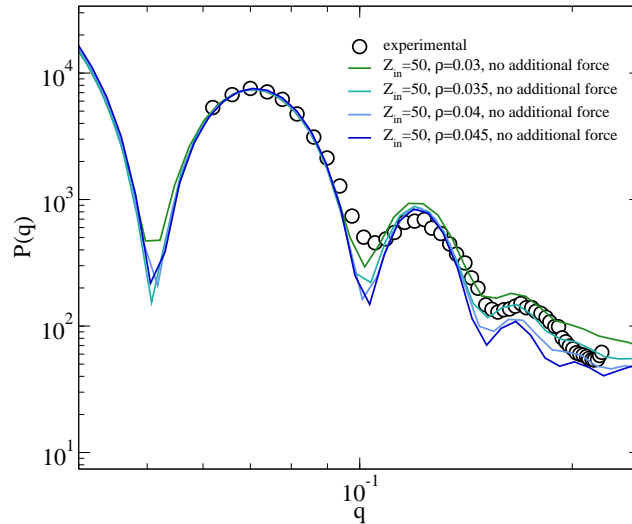


Figure 5.7: Form factors comparison for the thick-shell hollow microgel. Form factors at a fixed inner radius $Z_{in} = 50\sigma$ and outer radius $Z = 100\sigma$, varying the internal density ρ . Form factors are arbitrarily rescaled in the x and y-axes and compared to experimental outcomes (symbols).

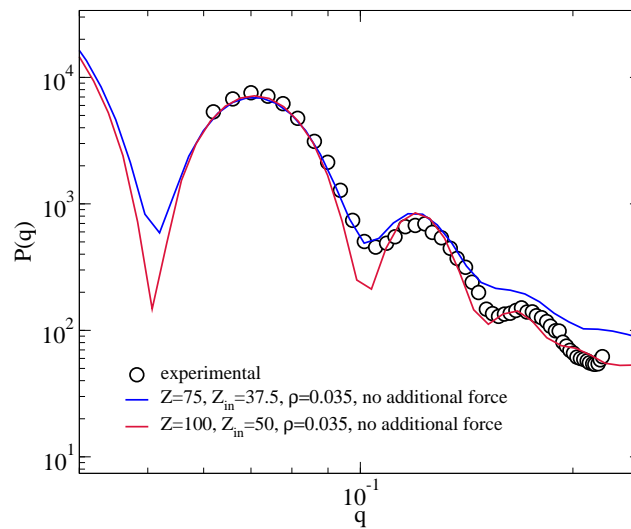


Figure 5.8: Form factors of thick-shell hollow microgels. Comparison of numerical (lines) and experimental (symbols) form factors for thick hollow microgels with two different overall sizes ($Z = 100\sigma$, $Z_{in} = 50\sigma$, $\rho = 0.035$ and $Z = 75\sigma$, $Z_{in} = 37.5\sigma$, $\rho = 0.035$). In both cases, $c = 5\%$. Form factors are arbitrarily rescaled in the y-axes.

not show any distinctive feature in the form factor (not shown) and are thus not appropriate to establish a proper comparison between numerical and experimental data. We also remark the importance of tuning the internal distribution of crosslinkers during the assembly, allowing to correctly reproduce the form factors at smaller length-scales (high wavevectors): while for the first analyzed case this

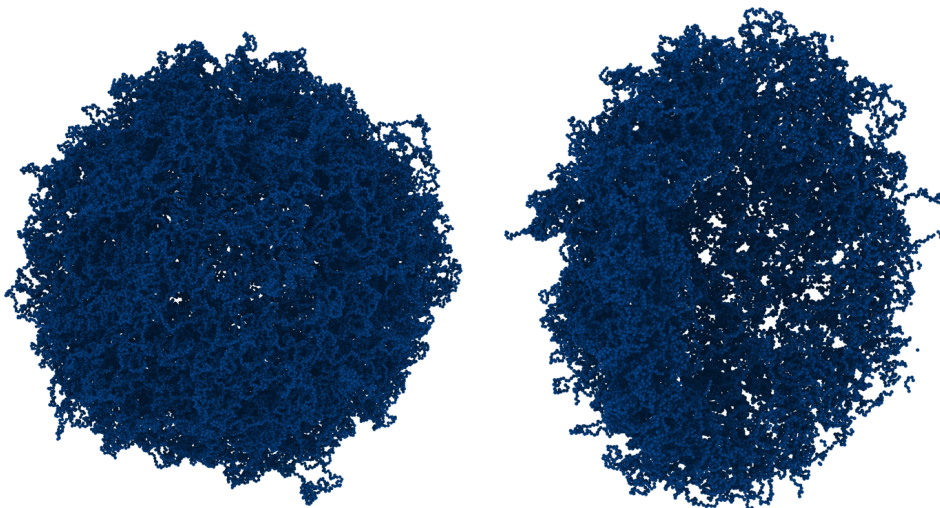


Figure 5.9: Simulation snapshots for the thick-shell hollow microgel. Full hollow microgel with a thick shell (left) and corresponding slice (right).

is not crucial, in the latter, when the shell already covers half of the total diameter, it induces notable changes in the shape of the form factor.

In the following, for both $Z_{in} = 75$ and 50, we consider the models with no additional force on the crosslinkers and $\rho = 0.035$.

5.1.2 Temperature effects

Building on these results, we study the temperature dependence of hollow microgels. Figure 5.10 shows the form factors for the microgels with different shell thickness for different values of α . We observe that for $\alpha \lesssim 0.5$ the form factors can be essentially superimposed in both cases. In fact, there is only a small shift to higher q values, as a consequence of the reduced microgel size with increasing temperature. For $\alpha > 0.5$, the behavior of the form factor is found to be dependent on the shell thickness. In particular, a quite abrupt change in its shape occurs, for microgels with a thinner shell, for $0.6 < \alpha < 0.7$ whereas, for microgels with a thicker shell, for $0.8 < \alpha < 0.9$.

To observe the structural changes that occur around these values it is more convenient to move to real space, and thus study the density profiles. These are reported in Fig. 5.11 and clearly evidence a range of effective temperatures from

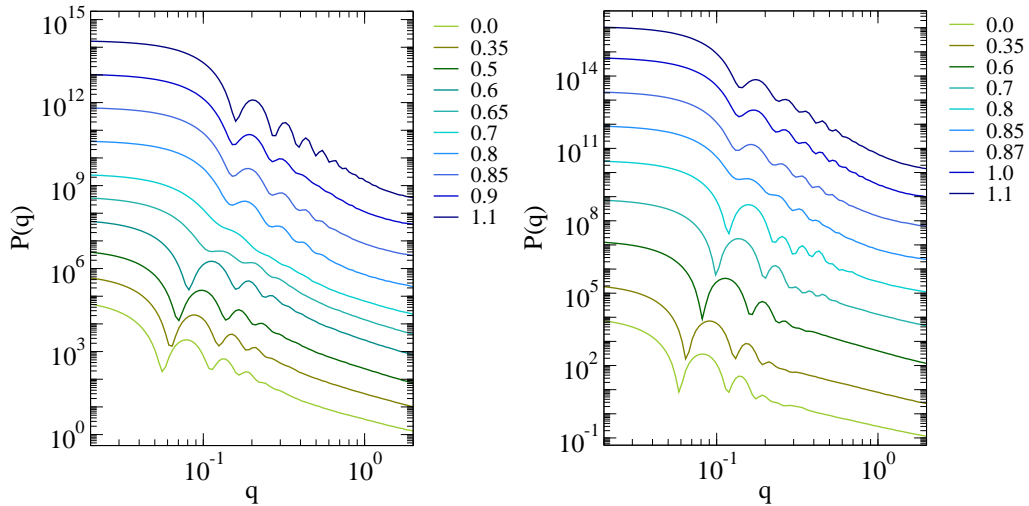


Figure 5.10: Numerical form factors as a function of effective temperature. Left: form factors as a function of the wavevector q for different values of α for the thin-shell hollow microgel. Right: form factors as a function of the wavevector q for different values of α for the thick-shell hollow microgel. Form factors are arbitrarily rescaled on the y-axis for visual clarity.

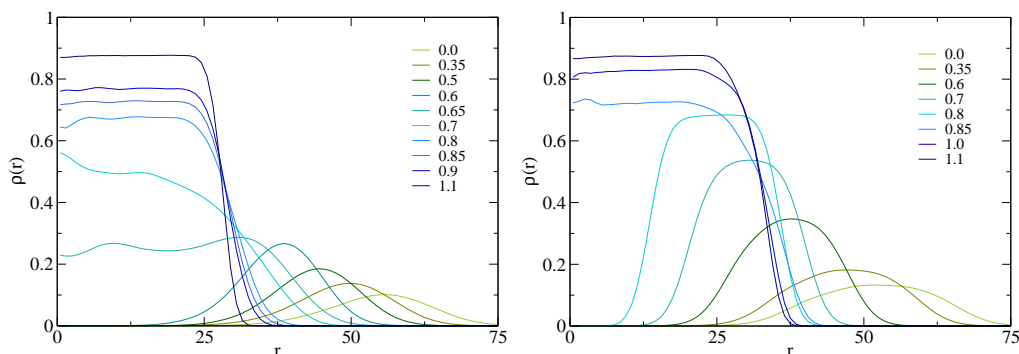


Figure 5.11: Density profiles of hollow microgels as a function of effective temperature. Top: radial density profiles for the thin-shell hollow microgel for different values of α . Bottom: radial density profiles for the thick-shell hollow microgel for different values of α .

which the density profile moves from that of a polymeric shell to that of a standard microgel, in which the internal cavity is completely filled by the polymer network. Therefore, by tuning the thickness of the shell, it is possible to tune the microgel density profile and adjust the temperature at which this takes place.

It is then possible to map numerical form factors onto experimental ones at different temperatures. Since experiments were performed at 25 and 45°C, the corresponding values of α for which there should be correspondence are 0.2 – 0.4 and a value higher than 0.8, according to the mapping established for regular microgels in Chapter 1. As shown in Fig. 5.12, the best agreement is obtained for $\alpha = 0.35$ in the swollen state and for $\alpha \approx 0.85$ and 0.87 (for thin and thick shell hollow microgels, respectively) in the collapsed state. The slight difference we found for the two cases should correspond to a difference in temperature of the order of one degree, which is well within the experimental error.

The swelling behavior for hollow microgels is shown in Fig. 5.13, where we report the swelling ratio $R_g/R_{g,max}$ as a function of the effective temperature α . In this way, we evidence how a thinner polymer shell allows for a higher swelling degree. In any case, even hollow microgels with a thicker shell swell more than standard microgels (whose swelling ratio is approximately around 0.5).

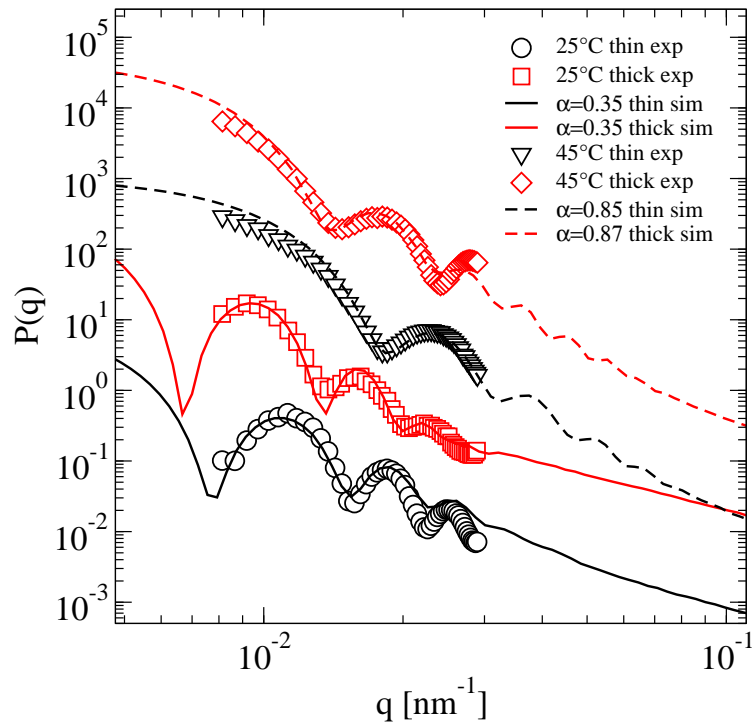


Figure 5.12: Temperature effects on the form factors. Comparison between experimental (symbols) and numerical (lines) form factors at 25 and 45°C for thin and thick-shell hollow microgels. Form factors are arbitrarily rescaled in the y-axis for visual clarity.

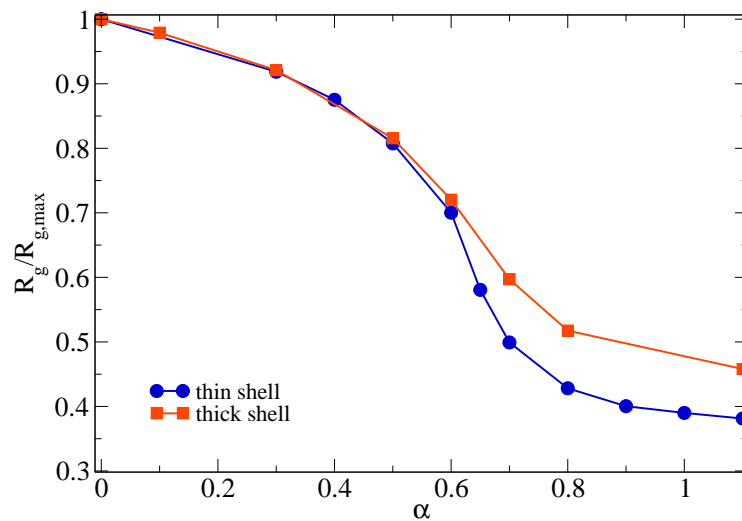


Figure 5.13: Swelling curves. Normalized gyration radius $R_g/R_{g,max}$ as a function of the swelling parameter α for the thin and thick-shell hollow microgels.

5.2 Conformation at the interface

Being deprived of an inner dense core, the conformation of hollow microgels at the interface is expected to be quite different from that of standard microgels whose conformation at the interface resemble that of a fried-egg. While polymer chains will certainly extend towards the water phase for their enhanced solubility, we should not expect strong protrusion as for standard core-corona microgels. We thus test the behavior of hollow microgel particles at a liquid-liquid interface, in full analogy with what has been performed for regular microgels in previous Chapters. In particular, we will consider the same modeling of the surface tension, mimicking a common water/hexane interface, and the same microgel-solvent interactions. For this analysis, we will employ smaller microgels with $Z = 75$

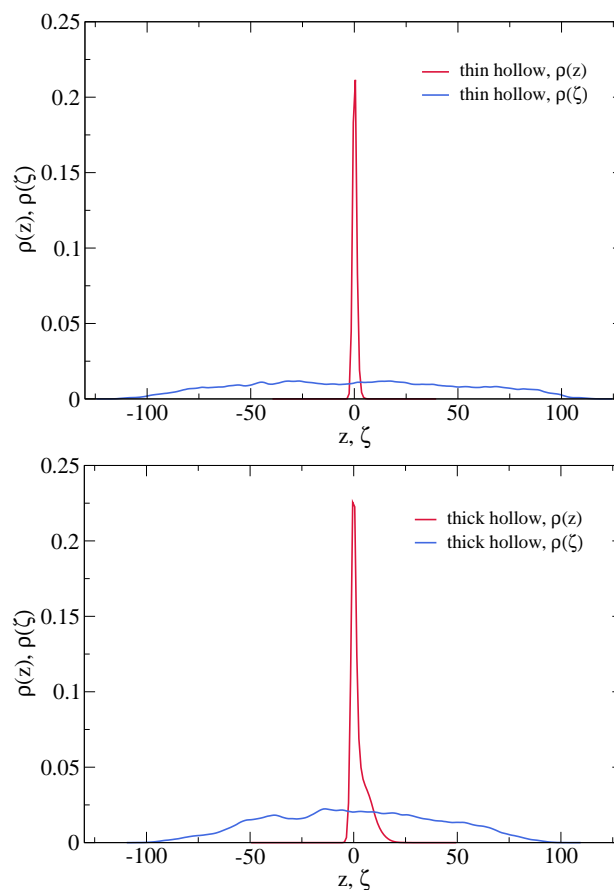


Figure 5.14: Density profiles at the interface. Top: density profiles $\rho(z)$ and $\rho(\zeta)$ for the thin-shell hollow microgel adsorbed at the interface. Bottom: density profiles $\rho(z)$ and $\rho(\zeta)$ for the thick-shell hollow microgel adsorbed at the interface.

(instead of the $Z = 100$ discussed before) to sensibly reduce the computation cost due to the presence of solvent particles. The density profiles $\rho(z)$ and $\rho(\zeta)$, as defined in Chapter 3, are reported in Fig. 5.14 for the thin and thick-shell hollow microgel, respectively, while their conformation at the interface can be visualized with the simulation snapshots reported in Fig. 5.15. The strongest differences are found of course for the microgels with a thin shell, which present a completely flat conformation at the interface. This translates in a flat $\rho(z)$ profile with a thickness across the interface being limited to few monomers. This behavior is related to the fact that the polymer network occupies the empty space left by the absence of the core once this is flattened by the two fluids. We should also take into account that the microgels analyzed here have an average density that is less than half that of standard microgels, a factor that undoubtedly influences the tendency to flatten. In this way, the difference in protrusion towards the preferred solvent is substantially not present. By comparing the $\rho(\zeta)$ profiles with that of a standard

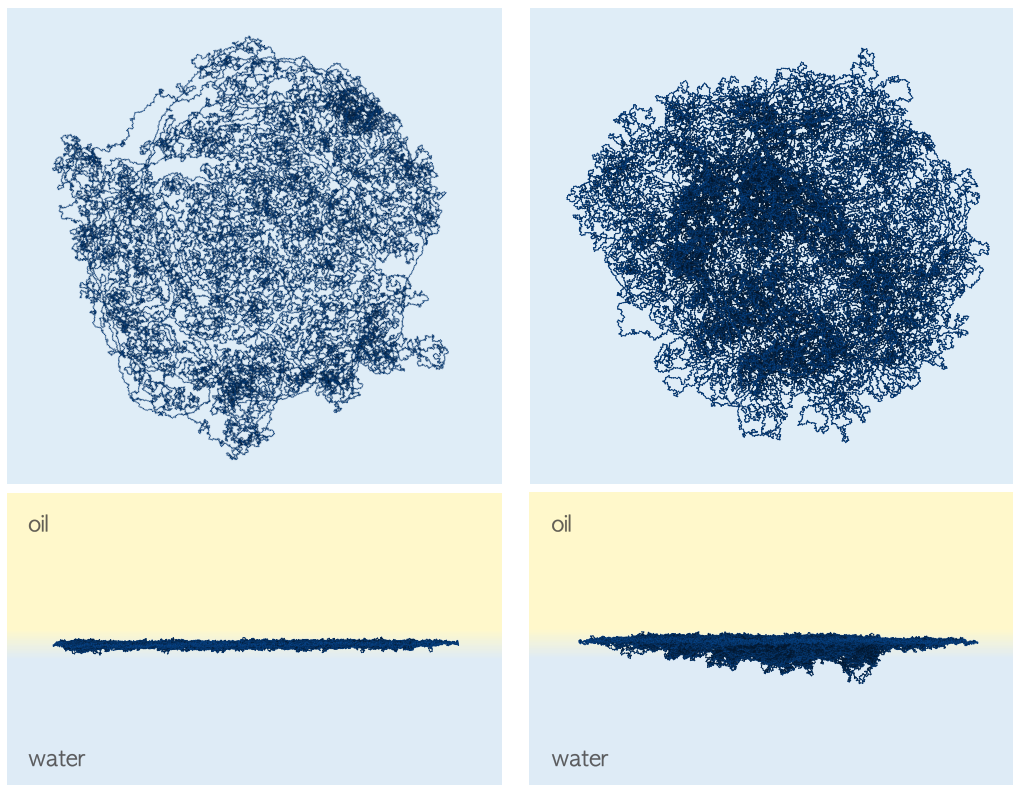


Figure 5.15: Simulation snapshots for hollow microgels at the interface. Top and side views of a thin-shell (left) and a thick-shell (right) microgels adsorbed at a liquid-liquid interface.

microgel (shown in Chapter 3) we can notice a substantial decrease in its density, especially in correspondence with the center of the microgel.

The microgel with a thicker shell exhibits a small bump in the lateral microgel profile, due to the higher amount of monomers that are present in the network. In this case, the presence of the bump is related to a quite uniform protrusion of the chains over all microgel extension rather than being related to the presence of the core as in the regular microgels, as it is clearly visible by the simulation snapshots. The polymer chains cannot fully adsorb at the interface and thus slightly protrude towards the water phase.

The main Reference for this Chapter is:

- J. Vialetto, F. Camerin, F. Grillo, L. Rovigatti, E. Zaccarelli, L. Isa, From single-particle hollow microgels in bulk to their collective behavior at interfaces, *in preparation* (2020)

Conclusions and Perspectives

Microgels are colloidal particles widely studied in different fields and they are promising model systems for fundamental investigations. In this Thesis, we have considered liquid-liquid interfaces as a tool to investigate microgels under a different condition with respect to the classical three-dimensional bulk study. This new line of research has been established by some recent experimental studies that have determined how the conformation of a single particle at the interface is radically different from the typical spherical colloid. The interest that has followed has been mainly focused on discovering novel practical applications for this system, which have proved to be undoubtedly noteworthy. On the other hand, from a more fundamental perspective, it is also important to address the origin of their macroscopic and collective behavior. In order to shed light on this aspect, which was ultimately the purpose of this Thesis, we employed numerical simulations and experiments thanks to which we were able to add a further piece to the knowledge of microgels and discover further potentialities.

Therefore, the first Chapters of this Thesis were dedicated to the analysis of the single components required to build a sound modeling of microgel particles at liquid-liquid interfaces, starting with the microgel model, going through the inclusion of an explicit solvent, to finally reach the single microgel absorbed at the interface. In order to build a model for microgels, it is important to take into account the polymeric nature of these colloidal particles. In this way, two are the essential features that have to be considered, namely the presence of a disordered network and the inhomogeneous distribution of crosslinkers which typically results from the chemical synthesis conditions. In Chapter 1, we thus described the coarse-graining procedure to build the microgel particles then employed in

the proceeding of the Thesis. Our microgel model is based on the self-assembly of patchy particles with two and four patches. We introduced an additional designing force to the latter, which represent crosslinkers, that allows to concentrate a higher amount of particles at the center of the microgel, forming its core, and leaving a lower monomer density in the corona. This core-corona structure cannot be obtained whenever simpler models are used, such as the diamond-lattice-based microgel model. In this case, crosslinkers are uniformly distributed and connected by polymer chains of equal length, not describing a realistic physical picture. We further demonstrated the importance of a non-uniform crosslinker distribution by comparing experimental and numerical form factors and showing a good agreement at all temperatures across the volume phase transition of the microgel.

While the study of microgels in bulk conditions can also be performed in the presence of an implicit solvent, this is not true when dealing with liquid-liquid interfaces. For this reason, in Chapter 2, we introduced an explicit solvent treatment by inserting in the simulation box coarse-grained solvent particles. There, we compared different ways of modeling an explicit solvent, either by means of particles with excluded volume interactions or via a soft bounded potential within the dissipative particle dynamics framework. In the first case, by analyzing the form factors and comparing with those calculated in implicit solvent, we found the presence of artifacts in the microgel form factors which were not retrieved in case DPD was used. The study of microgels with the explicit solvent also allowed us to make an estimate of how much these colloids can actually retain the solvent: in the swollen state, microgels are found to be filled by solvent while it is almost completely expelled at high temperatures. The entire protocol to model solvent particles described in this Chapter is also applicable to systems other than microgels, in every case a generic polymer is involved.

By combining the knowledge acquired in the first two Chapters, in Chapter 3, we discussed the model for single microgel particles adsorbed at interfaces. The parameters of the DPD solvent are tuned in such a way that the surface tension between the two fluids is that of a water/hexane interface. The study of a single microgel, although it is necessary preliminary step for the assessment of their collective behavior, allowed us to determine their microstructure at the

interface as a function of the crosslinker concentration. Indeed, we confirmed an increasingly marked core-protrusion towards the preferred water phase and a reduced extension on the interfacial plane as the crosslinker concentration increases more and more, as also evidenced by the experimental AFM and FreSca imaging. Further confirming the importance of a correct modeling of the microgel, we verified that a microgel built on a regular lattice cannot reproduce this behavior, due to the absence of a real core.

The link between individual particles at interfaces and their collective behavior relies in the microgel-microgel interaction potential, which effectively corresponds to perform a further level of coarse-graining. The calculation of the two-body effective potential for standard microgels, discussed in Chapter 4, evidenced the presence of a single characteristic length, being well described by a 2D Hertzian potential. A possible explanation for this has to do with the further stretching of the polymer chains, which thus reduces the distinction between the core and the corona. We also discovered a stiffening of the microgel and an increase of the elastic moduli by almost one order of magnitude as compared to bulk conditions. Most importantly, we found that small and loosely crosslinked particles interacting with a 2D Hertzian potential undergo a fluid-glass-fluid reentrant transition in a range of parameters that is compatible for future experimental observations. In this respect, the work presented in this Thesis establishes microgels at interfaces as a new model system for fundamental investigations, paving the way for the experimental synthesis and research on unique high-density liquid-like states. From a material science perspective, these results can guide the development of novel assembly and patterning strategies on surfaces and the design of novel materials with desired interfacial behavior.

Chapter 5 was instead dedicated to the analysis of hollow microgels, for which an entirely different conformation at the interface has to be expected. In this case, they are effectively synthesized with a cavity in the center of the particle. As for standard microgels, we first verify the compatibility of the form factors with those extracted via SLS experiments for two different shell thicknesses. The differences between the two are also evident in the numerical density profiles studied as a function of the effective temperature. While in both cases the final

state involves the filling of the cavity, for thin hollow microgels this transition takes place at lower effective temperatures than for thicker microgels. Another important aspect resulting from the comparison with experimental form factors concerns the density of the polymer that makes up the shell, which is lower by more than 50% the average density of a standard microgel. This also has an effect on the conformation at the interface. On the one hand, the lack of the core makes it possible to obtain substantially flat particles at the interface and, on the other hand, due to the reduced polymer density, an even greater extension than that of a standard microgel is expected. A similar behavior was indeed observed for microgels with an ultra-low crosslinker concentration.

It will be important in the future to extend the study on the microgel effective interactions to crowded configurations to investigate the validity of the present results at considerably high packing fractions where additional mechanisms, like faceting or interpenetration, may become relevant. Under these conditions, many-body effects should also play a prominent role despite these cannot properly be quantified due to severe computational limitations, since a huge number of particles should be used. Similar considerations should be extended to microgels in bulk conditions, for which high-density states still require appropriate theoretical assessment. The analysis can be further broadened to other topologies such as hollow microgels. In that case, as previously described, the conformation of the microgel is completely different with most of the chains being adsorbed, or in proximity, of the interface. More specifically, it will be interesting to understand the influence of the topology on the effective interaction potential and, for instance, the consequences of the reduction in the polymer density we found for hollow particles.

On the side of the microgel modeling, an important aspect that has been overlooked up to this moment is the role of the dangling chains. In particular, the assembly process we exploit for our model generates in the periphery of the microgel mostly closed loops, while dangling chains are essentially not present. This is a direct consequence of the use of two and four folded patchy particles which unlikely generate "dead-end" chains in favor of a fully-assembled network.

Nonetheless, they are believed to be present in laboratory microgels, especially when the synthesis is performed via the precipitation polymerization procedure. Although we do not expect major changes for the types of analysis performed in the Thesis, the dangling chains could have important implications in the diffusive behavior of the microgel and thus manifest through the hydrodynamic properties of the system, which we expect to investigate in the near future.

All in all, the research presented in this Thesis opens the way for the investigation of microgels at the interface as a simple realization of 2D elastic particles. We expect that the evidence reported will have important consequences on the study of two-dimensional elastic objects at the fundamental level and for the clever design of composite materials.

A brief description of parallel work on charged microgels

In this section, we will briefly outline a work-in-progress project started during the course of the PhD. This is strictly related to the work presented in the previous Chapters and concerns the modeling of charged microgels.

Ionic microgel particles are intriguing systems in which the properties of polymer colloids are enriched by the presence of charged groups. Charged microgels are typically synthesized co-polymerizing PNIPAM and polyacrylic acid (pAAc) so that the thermoresponsive properties of the former are combined with the pH-responsive features of the latter [36, 257, 258]. Indeed, at low pH, the already high concentration of hydronium in solution inhibits the dissociation of pAAc favoring the formation of an almost neutral microgel. On the contrary, for high pH, charged monomers dissociate generating a charged distribution throughout the entire polymer network. It is obvious that a series of direct applicative advantages derives from the double responsivity as it has been done for the smart design of optical devices based on colloidal photonic crystals [28].

The importance in the study of charged microgels, in addition to this type of capabilities, can help to analyze other key issues in the behavior of colloidal microgels. As pointed out in the Introduction, the role of the charges in the study of so-called neutral microgels has yet to be clarified and deepened, to confirm that structural features of microgels directly originate from the presence of these charges [30]. At the same time, it will be important to understand where charged moieties are exactly located, although it seems likely to be in the outer region of

the microgel in order to minimize the electrostatic repulsive interactions. Another aspect that needs to be clarified, for example, has to do with the role of the charges in the presence of a confinement at the interface. For all these aspects, the numerical simulations can be very helpful, thanks to the ability to study some details that could not be analyzed with experiments. It is clear, however, that an appropriate modelling of the particles is necessary, complicated by the fact that in this case the particles also contain charges. So far, several investigations of the swelling behavior of charged microgels have relied on a mean-field treatment of the polymer network [259] while counterions are often considered in an implicit fashion via the Debye-Huckel theory [260, 261].

Our work thus focuses on two main aspects, namely the use of a disordered network and the explicit inclusion of counterions in the model. Regarding the first point, an important contribution came from the modeling of neutral microgels in bulk, presented in Chapter 1. While previous studies were based on the diamond-lattice-based model [135, 262–264], we account for the effect of the network topology in a more realistic way, ensuring that internal density and swelling behavior could reproduce experimental results. A charged configuration is obtained by assigning a negative charge to some of the monomers of a neutral microgel. The overall charge is balanced by the presence of coarse-grained counterions.

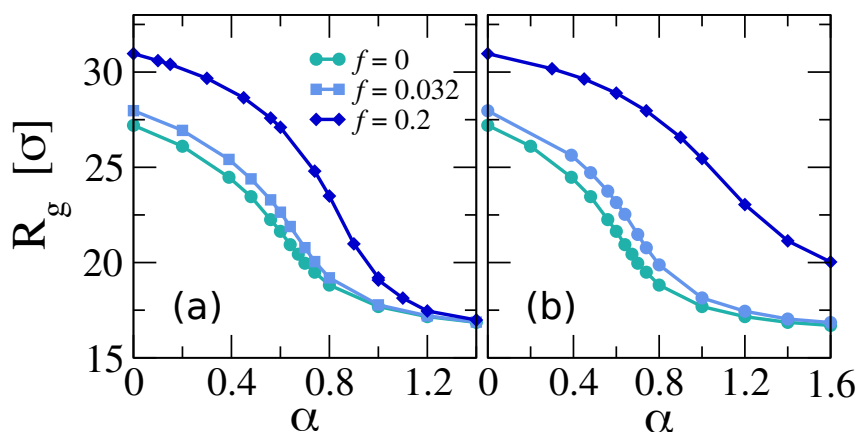


Figure C.1: Swelling curves of charged microgels. Adapted from Ref. [265]. Gyration radius as a function of effective temperature for different charge fractions f in case (a) charged ions have a varying affinity for the solvent and (b) have always a high affinity for the solvent.

A brief description of parallel work on charged microgels

A relevant aspect of the modeling, which has implications in the microgel swelling behavior, relates to the affinity of the charges for the solvent (either implicit or explicit). In fact, we directly compared the case in which charged monomers have always the same affinity of neutral monomers, which increases with increasing effective temperature, to the case in which charged ions have always a high affinity for the solvent. The latter case is equivalent of considering the hydrophilic character of the charged co-polymer at all investigated temperatures, which would increase the stability of the microgel for increasing fraction of charges f . As shown in Fig. C.1, in both cases we observe that, by increasing f , the size of the microgel also increases and correspondingly a shift of the VPT towards larger effective temperatures occurs, in agreement with experimental observations. On the other hand, relevant differences arise when considering the collapsed state of the microgels. In fact, while in the first case a net transition occurs at all f , in the second case, the VPT is essentially suppressed at higher charge fractions. The latter situation is actually the one that is observed experimentally, where it has been shown that even for values of f sensibly lower than 0.2, that is the maximum charge fraction investigated here, the microgel does not achieve a fully collapsed state for temperatures higher than $40^{\circ}C$.

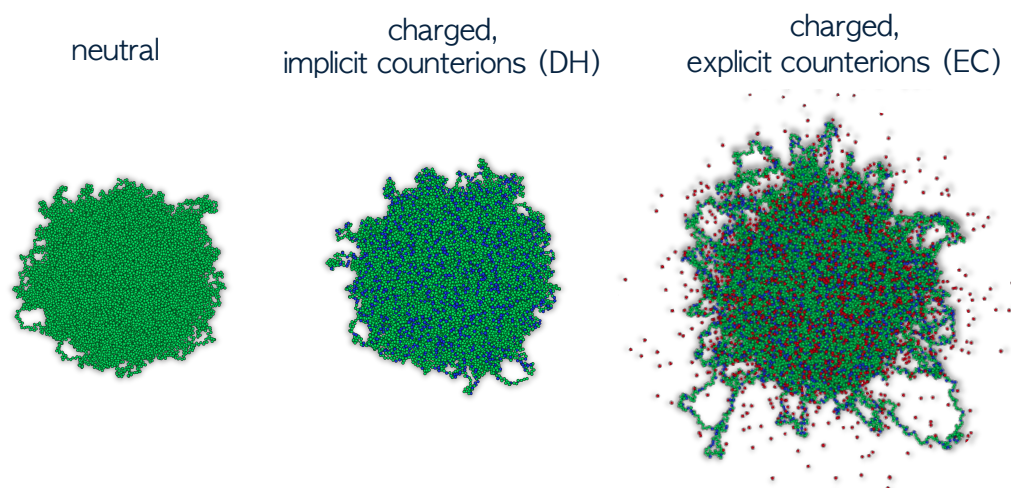


Figure C.2: Simulation snapshots. Adapted from Ref. [266]. Comparison of the models analyzed at an intermediate swelling ratio: neutral, charged with implicit counterions treated with Debye-Huckel and charged with explicit counterions. Green particles are neutral monomers, blue particles are charged monomers and red particles are counterions.

Important differences are instead retrieved in the microgel structure by considering or not an explicit treatment of the counterions. More specifically, our findings highlight that the Debye-Huckel approach fails to take into account the osmotic pressure of both inner counterions, acting in favor of microgel swelling, and external ones, acting against swelling. It is noteworthy to observe how the structural features of a microgel simulated with this implicit model are actually more similar to those of neutral microgels than to the case of a charged microgel with explicit counterions. This is clearly visible also by the simulation snapshots, reported in Fig. C.2 for neutral microgels and for those studied with implicit and explicit counterions at intermediate values of the solvophobic parameter α , where the most dramatic differences arise. The three snapshots refer to the very same network topology and evidence how in the presence of explicit counterions the microgel appears to be made of a core and of a rather inhomogeneous corona. In fact, the most external chains do not completely collapse while they form small clusters between themselves and remain distinct from the homogeneous core. Such features are instead absent for neutral microgels and for microgels with implicit counterions. The reason for this behavior can be found in the fact that, when counterions are explicitly included, it is possible to compensate the

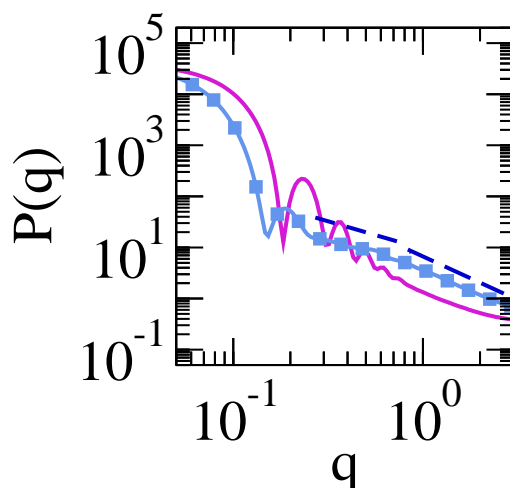


Figure C.3: Form factors. Adapted from Ref. [265]. Comparison of the form factor of neutral (solid line) and charged (symbols and line) microgels at an intermediate swelling ratio. The dashed lines highlight the two regimes at intermediate and high wavevectors that appear for the charged microgels.

balance between attraction and repulsion among monomers also locally. These features are also reflected in the form factor of the microgels, shown in Fig. C.3, in which two distinct regimes appear at intermediate and high wavevectors, thus presenting a shape that is incompatible with the fuzzy-sphere model that usually fits regular microgels. These results have yet to find experimental confirmation.

A final aspect of the single particle modeling concerns the inclusion of explicit solvent. It is possible to demonstrate that the inclusion of DPD particles with the same parameters as it was done for neutral microgels in Chapter 2 allows to reproduce microgels with essentially the same structural features as for the implicit solvent treatment (not shown). Minor differences are found in the swelling behavior for increasing fraction of charges in the polymer network.

The main References for this section are:

- G. Del Monte, F. Camerin, A. Ninarello, N. Gnan, L. Rovigatti, E. Zaccarelli, Charge affinity and solvent effects in numerical simulations of ionic microgels, *Journal of Physics: Condensed Matter*, accepted (2020)
- G. Del Monte, A. Ninarello, F. Camerin, L. Rovigatti, N. Gnan, E. Zaccarelli, Numerical insights on ionic microgels: structure and swelling behavior, *Soft Matter* **15**, 8113-8128 (2019)

List of publications

- J. Vialetto, F. Camerin, F. Grillo, L. Rovigatti, E. Zaccarelli, L. Isa, From single-particle hollow microgels in bulk to their collective behavior at interfaces, *in preparation* (2020)
- G. Del Monte, D. Truzzolillo, F. Camerin, A. Ninarello, N. Gnan, L. Rovigatti, S. Sennato, E. Zaccarelli, The role of electrostatics in the structural features of microgel particles, *in preparation* (2020)
- G. Del Monte, F. Camerin, A. Ninarello, N. Gnan, L. Rovigatti, E. Zaccarelli, Charge affinity and solvent effects in numerical simulations of ionic microgels, *Journal of Physics: Condensed Matter*, accepted (2020)
- F. Camerin, N. Gnan, J. Ruiz-Franco, A. Ninarello, L. Rovigatti, E. Zaccarelli, Microgels at interfaces as 2D effective particles, *Physical Review X* **10**, 031012 (2020)
- J. Ruiz-Franco, F. Camerin, N. Gnan, E. Zaccarelli, Tuning the rheological behavior of colloidal gels through competing interactions, *Physical Review Materials* **4**, 045601 (2020)
- G. Del Monte, A. Ninarello, F. Camerin, L. Rovigatti, N. Gnan, E. Zaccarelli, Numerical insights on ionic microgels: structure and swelling behavior, *Soft Matter* **15**, 8113-8128 (2019)
- A. Ninarello, J. J. Crassous, D. Paloli, F. Camerin, N. Gnan, L. Rovigatti, P. Schurtenberger, E. Zaccarelli, Modeling microgels with a controlled structure across the volume phase transition, *Macromolecules* **52**, 7584-7592 (2019)

List of publications

- F. Camerin, M. A. Fernandez-Rodriguez, L. Rovigatti, Maria-Nefeli Antonopoulou, N. Gnan, A. Ninarello, L. Isa, E. Zaccarelli, Microgels adsorbed at liquid-liquid interfaces: a joint numerical and experimental study, *ACS Nano* **13**, 4548 (2019)
- F. Camerin, N. Gnan, L. Rovigatti, E. Zaccarelli, Modelling realistic microgels in an explicit solvent, *Scientific Reports* **8**, 14426 (2018)

References

- [1] Masao Doi. *Soft matter physics*. Oxford University Press, 2013.
- [2] Jasper van der Gucht. Grand challenges in soft matter physics. *Frontiers in Physics*, 6:87, 2018.
- [3] Richard Anthony Lewis Jones, R Jones, Richard AL Jones, et al. *Soft condensed matter*, volume 6. Oxford University Press, 2002.
- [4] Jean-Pierre Hansen and Ian Randal McDonald. *Theory of simple liquids: with applications to soft matter*. Academic Press, 2013.
- [5] Michael Rubinstein and Ralph H Colby. *Polymer Physics*, volume 23. Oxford University Press New York, 2003.
- [6] Wilson Poon. Colloids as big atoms. *Science*, 304(5672):830–831, 2004.
- [7] Neer Asherie, Aleksey Lomakin, and George B Benedek. Phase diagram of colloidal solutions. *Physical Review Letters*, 77(23):4832, 1996.
- [8] Emanuela Zaccarelli. Colloidal gels: equilibrium and non-equilibrium routes. *Journal of Physics: Condensed Matter*, 19(32):323101, 2007.
- [9] Frank Scheffold and Peter Schurtenberger. Light scattering probes of viscoelastic fluids and solids. *Soft Materials*, 1(2):139–165, 2003.
- [10] Vassiliy Lubchenko and Peter G Wolynes. Theory of structural glasses and supercooled liquids. *Annu. Rev. Phys. Chem.*, 58:235–266, 2007.
- [11] Christos N Likos. Effective interactions in soft condensed matter physics. *Physics Reports*, 348(4-5):267–439, 2001.
- [12] Christos N Likos. Soft matter with soft particles. *Soft matter*, 2(6):478–498, 2006.
- [13] Salvatore Torquato. Perspective: Basic understanding of condensed phases of matter via packing models. *The Journal of chemical physics*, 149(2):020901, 2018.
- [14] James G Berryman. Random close packing of hard spheres and disks. *Physical Review A*, 27(2):1053, 1983.
- [15] MD Rintoul and Salvatore Torquato. Computer simulations of dense hard-sphere systems. *The Journal of chemical physics*, 105(20):9258–9265, 1996.

-
- [16] Peter N Pusey and W Van Megen. Phase behaviour of concentrated suspensions of nearly hard colloidal spheres. *Nature*, 320(6060):340–342, 1986.
- [17] Peter N Pusey and William van Megen. Observation of a glass transition in suspensions of spherical colloidal particles. *Physical review letters*, 59(18):2083, 1987.
- [18] Ludovic Berthier, Daniele Coslovich, Andrea Ninarello, and Misaki Ozawa. Equilibrium sampling of hard spheres up to the jamming density and beyond. *Physical review letters*, 116(23):238002, 2016.
- [19] Andrea J Liu and Sidney R Nagel. Jamming is not just cool any more. *Nature*, 396(6706):21–22, 1998.
- [20] Sebastian Golde, Thomas Palberg, and Hans Joachim Schöpe. Correlation between dynamical and structural heterogeneities in colloidal hard-sphere suspensions. *Nature Physics*, 12(7):712–717, 2016.
- [21] Rafael Díaz Hernández Rojas, Giorgio Parisi, and Federico Ricci-Tersenghi. Inferring the particle-wise dynamics of amorphous solids from the local structure at the jamming point. *Soft Matter*, 2020.
- [22] Yang Jiao, Timothy Lau, Haralampos Hatzikirou, Michael Meyer-Hermann, Joseph C Corbo, and Salvatore Torquato. Avian photoreceptor patterns represent a disordered hyperuniform solution to a multiscale packing problem. *Physical Review E*, 89(2):022721, 2014.
- [23] Germán Rivas, Javier A Fernández, and Allen P Minton. Direct observation of the enhancement of noncooperative protein self-assembly by macromolecular crowding: indefinite linear self-association of bacterial cell division protein ftsz. *Proceedings of the National Academy of Sciences*, 98(6):3150–3155, 2001.
- [24] Duyu Chen, Wen Yih Aw, Danelle Devenport, and Salvatore Torquato. Structural characterization and statistical-mechanical model of epidermal patterns. *Biophysical journal*, 111(11):2534–2545, 2016.
- [25] Dimitris Vlassopoulos and Michel Cloitre. Tunable rheology of dense soft deformable colloids. *Current opinion in colloid & interface science*, 19(6):561–574, 2014.
- [26] R Allen LaCour, Carl Simon Adorf, Julia Dshemuchadse, and Sharon C Glotzer. The influence of softness on the stability of binary colloidal crystals. *ACS Nano*, 13(12):13829–13842, 2019.
- [27] Alberto Fernandez-Nieves, Hans Wyss, Johan Mattsson, and David A Weitz. *Microgel suspensions: fundamentals and applications*. John Wiley & Sons, 2011.
- [28] L Andrew Lyon and Alberto Fernandez-Nieves. The polymer/colloid duality of microgel suspensions. *Annual Review of Physical Chemistry*, 63:25–43, 2012.

- [29] Joanna B Thorne, George J Vine, and Martin J Snowden. Microgel applications and commercial considerations. *Colloid and Polymer Science*, 289(5-6):625, 2011.
- [30] Matthias Karg, Andrij Pich, Thomas Hellweg, Todd Hoare, L Andrew Lyon, Jérôme J Crassous, Daisuke Suzuki, Rustam A Gumerov, Stefanie Schneider, and Igor I Potemkin. Nanogels and microgels: From model colloids to applications, recent developments, and future trends. *Langmuir*, 35(19):6231–6255, 2019.
- [31] Alberto Martín-Molina and Manuel Quesada-Pérez. A review of coarse-grained simulations of nanogel and microgel particles. *Journal of Molecular Liquids*, 280:374–381, 2019.
- [32] Julian Oberdisse and Thomas Hellweg. Recent advances in stimuli-responsive core-shell microgel particles: synthesis, characterisation, and applications. *Colloid and Polymer Science*, 2020.
- [33] Matthias Karg and Thomas Hellweg. New “smart” poly (nipam) microgels and nanoparticle microgel hybrids: Properties and advances in characterisation. *Current Opinion in Colloid & Interface Science*, 14(6):438–450, 2009.
- [34] RH Pelton and P Chibante. Preparation of aqueous latices with n-isopropylacrylamide. *Colloids and surfaces*, 20(3):247–256, 1986.
- [35] Brian R Saunders and Brian Vincent. Microgel particles as model colloids: theory, properties and applications. *Advances in Colloid and Interface science*, 80(1):1–25, 1999.
- [36] Sofi Nöjd, Peter Holmqvist, Niels Boon, Marc Obiols-Rabasa, Priti S Mohanty, Ralf Schweins, and Peter Schurtenberger. Deswelling behaviour of ionic microgel particles from low to ultra-high densities. *Soft Matter*, 14(20):4150–4159, 2018.
- [37] Robert Pelton. Temperature-sensitive aqueous microgels. *Advances in Coll. and Interf. Science*, 85(1):1–33, 2000.
- [38] Eric Siemes, Oleksii Nevskyi, Dmytro Sysoiev, Sarah K Turnhoff, Alex Oppermann, Thomas Huhn, Walter Richtering, and Dominik Wöll. Nanoscopic visualization of cross-linking density in polymer networks with diarylethene photoswitches. *Angewandte Chemie International Edition*, 57(38):12280–12284, 2018.
- [39] Andrea Scotti, Urs Gasser, Emily S Herman, Miguel Pelaez-Fernandez, Jun Han, Andreas Menzel, L Andrew Lyon, and Alberto Fernández-Nieves. The role of ions in the self-healing behavior of soft particle suspensions. *Proceedings of the National Academy of Sciences*, 113(20):5576–5581, 2016.
- [40] Satish Nayak, Daoji Gan, Michael J Serpe, and L Andrew Lyon. Hollow thermoresponsive microgels. *Small*, 1(4):416–421, 2005.

- [41] Anne C Nickel, Andrea Scotti, Judith E Houston, Thiago Ito, Jérôme Crassous, Jan Skov Pedersen, and Walter Richtering. Anisotropic hollow microgels that can adapt their size, shape, and softness. *Nano Letters*, 19(11):8161–8170, 2019.
- [42] Veronique Lapeyre, Natacha Renaudie, Jean-Francois Dechezelles, Hassan Saadaoui, Serge Ravaine, and Valerie Ravaine. Multiresponsive hybrid microgels and hollow capsules with a layered structure. *Langmuir*, 25(8):4659–4667, 2009.
- [43] Sarah K Wypysek, Andrea Scotti, Mohammed O Alziyadi, Igor I Potemkin, Alan R Denton, and Walter Richtering. Tailoring the cavity of hollow polyelectrolyte microgels. *Macromolecular rapid communications*, 41(1):1900422, 2020.
- [44] Jérôme J Crassous, Hervé Dietsch, Patrick Pfliegerer, Vikash Malik, Ana Diaz, Liliane Ackermann Hirshi, Markus Drechsler, and Peter Schurtenberger. Preparation and characterization of ellipsoidal-shaped thermosensitive microgel colloids with tailored aspect ratios. *Soft Matter*, 8(13):3538–3548, 2012.
- [45] Jérôme J Crassous, Adriana M Mihut, Linda K Månsson, and Peter Schurtenberger. Anisotropic responsive microgels with tuneable shape and interactions. *Nanoscale*, 7(38):15971–15982, 2015.
- [46] Irmgard Bischofberger and Veronique Trappe. New aspects in the phase behaviour of poly-n-isopropyl acrylamide: systematic temperature dependent shrinking of pnipam assemblies well beyond the lcst. *Sci. Rep.*, 5:15520, 2015.
- [47] AK Lele, MM Hirve, MV Badiger, and RA Mashelkar. Predictions of bound water content in poly (n-isopropylacrylamide) gel. *Macromolecules*, 30(1):157–159, 1997.
- [48] Michael Heskins and James E Guillet. Solution properties of poly (n-isopropylacrylamide). *Journal of Macromolecular Science—Chemistry*, 2(8):1441–1455, 1968.
- [49] Timo Brandel, Viktor Sabadasch, Yvonne Hannappel, and Thomas Hellweg. Improved smart microgel carriers for catalytic silver nanoparticles. *ACS omega*, 4(3):4636–4649, 2019.
- [50] Yan Lu, Sebastian Proch, Marc Schrunner, Markus Drechsler, Rhatt Kempe, and Matthias Ballauff. Thermosensitive core-shell microgel as a “nanoreactor” for catalytic active metal nanoparticles. *Journal of Materials Chemistry*, 19(23):3955–3961, 2009.
- [51] Hua Li, Guoping Yan, Shunnian Wu, Zijie Wang, and KY Lam. Numerical simulation of controlled nifedipine release from chitosan microgels. *Journal of Applied Polymer Science*, 93(4):1928–1937, 2004.

- [52] Helena Bysell, Ronja Månsson, Per Hansson, and Martin Malmsten. Microgels and microcapsules in peptide and protein drug delivery. *Advanced Drug Delivery Reviews*, 63(13):1172–1185, 2011.
- [53] Justin D Debord and L Andrew Lyon. Thermoresponsive photonic crystals. *The Journal of Physical Chemistry B*, 104(27):6327–6331, 2000.
- [54] Luca Prodi. Luminescent chemosensors: from molecules to nanoparticles. *New Journal of Chemistry*, 29(1):20–31, 2005.
- [55] Ahmed M Alsayed, Mohammad F Islam, Jian Zhang, Peter J Collings, and Arjun G Yodh. Premelting at defects within bulk colloidal crystals. *Science*, 309(5738):1207–1210, 2005.
- [56] Divya Paloli, Priti S Mohanty, Jérôme J Crassous, Emanuela Zaccarelli, and Peter Schurtenberger. Fluid–solid transitions in soft-repulsive colloids. *Soft Matter*, 9(11):3000–3004, 2013.
- [57] Adrian-Marie Philippe, Domenico Truzzolillo, Julian Galvan-Myoshi, Philippe Dieudonné-George, Véronique Trappe, Ludovic Berthier, and Luca Cipelletti. Glass transition of soft colloids. *Physical Review E*, 97(4):040601, 2018.
- [58] Zexin Zhang, Ning Xu, Daniel TN Chen, Peter Yunker, Ahmed M Alsayed, Kevin B Aptowicz, Piotr Habdas, Andrea J Liu, Sidney R Nagel, and Arjun G Yodh. Thermal vestige of the zero-temperature jamming transition. *Nature*, 459(7244):230–233, 2009.
- [59] Thomas A Caswell, Zexin Zhang, Margaret L Gardel, and Sidney R Nagel. Observation and characterization of the vestige of the jamming transition in a thermal three-dimensional system. *Physical Review E*, 87(1):012303, 2013.
- [60] C Austen Angell. Formation of glasses from liquids and biopolymers. *Science*, 267(5206):1924–1935, 1995.
- [61] Johan Mattsson, Hans M Wyss, Alberto Fernandez-Nieves, Kunimasa Miyazaki, Zhibing Hu, David R Reichman, and David A Weitz. Soft colloids make strong glasses. *Nature*, 462(7269):83–86, 2009.
- [62] Valentina Nigro, Barbara Ruzicka, Beatrice Ruta, Federico Zontone, Monica Bertoldo, Elena Buratti, and Roberta Angelini. Relaxation dynamics, softness, and fragility of microgels with interpenetrated polymer networks. *Macromolecules*, 53(5):1596–1603, 2020.
- [63] Pieter Van Der Scheer, Ties Van De Laar, Jasper Van Der Gucht, Dimitris Vlassopoulos, and Joris Sprakel. Fragility and strength in nanoparticle glasses. *ACS nano*, 11(7):6755–6763, 2017.
- [64] Markus Stieger, Jan Skov Pedersen, Peter Lindner, and Walter Richtering. Are thermoresponsive microgels model systems for concentrated colloidal suspensions? a rheology and small-angle neutron scattering study. *Langmuir*, 20(17):7283–7292, 2004.

- [65] Thomas Eckert and Walter Richtering. Thermodynamic and hydrodynamic interaction in concentrated microgel suspensions: Hard or soft sphere behavior? *The Journal of Chemical Physics*, 129(12):124902, 2008.
- [66] Thomas Hellweg, CD Dewhurst, E Brückner, K Kratz, and W Eimer. Colloidal crystals made of poly (n-isopropylacrylamide) microgel particles. *Colloid and Polymer Science*, 278(10):972–978, 2000.
- [67] H Senff and W Richtering. Temperature sensitive microgel suspensions: Colloidal phase behavior and rheology of soft spheres. *The Journal of Chemical Physics*, 111(4):1705–1711, 1999.
- [68] Holger Senff and Walter Richtering. Influence of cross-link density on rheological properties of temperature-sensitive microgel suspensions. *Colloid and Polymer Science*, 278(9):830–840, 2000.
- [69] M Pelaez-Fernandez, Anton Souslov, LA Lyon, Paul M Goldbart, and A Fernandez-Nieves. Impact of single-particle compressibility on the fluid-solid phase transition for ionic microgel suspensions. *Physical review letters*, 114(9):098303, 2015.
- [70] Matthew Clements, Srinivasa Rao Pullela, Andres F Mejia, Jingyi Shen, Tieying Gong, and Zhengdong Cheng. Thermosensitive hard spheres. *Journal of colloid and interface science*, 317(1):96–100, 2008.
- [71] Priti S Mohanty, Divya Paloli, Jérôme J Crassous, Emanuela Zaccarelli, and Peter Schurtenberger. Effective interactions between soft-repulsive colloids: Experiments, theory, and simulations. *The Journal of Chemical Physics*, 140(9):094901, 2014.
- [72] B Sierra-Martin and A Fernandez-Nieves. Phase and non-equilibrium behaviour of microgel suspensions as a function of particle stiffness. *Soft Matter*, 8(15):4141–4150, 2012.
- [73] Jérôme J Crassous, Miriam Siebenbürger, Matthias Ballauff, Markus Drechsler, Oliver Henrich, and Matthias Fuchs. Thermosensitive core-shell particles as model systems for studying the flow behavior of concentrated colloidal dispersions. *The Journal of chemical physics*, 125(20):204906, 2006.
- [74] Lev Davidovich Landau and Evgenii Mikhailovich Lifshits. *Theory of Elasticity: By LD Landau and EM Lifshitz. Translated from the Russian by JB Sykes and WH Reid*. Pergamon Press, 1964.
- [75] Maxime J Bergman, Nicoletta Gnan, Marc Obiols-Rabasa, Janne-Mieke Meijer, Lorenzo Rovigatti, Emanuela Zaccarelli, and Peter Schurtenberger. A new look at effective interactions between microgel particles. *Nature communications*, 9(1):5039, 2018.
- [76] You-Liang Zhu and Zhong-Yuan Lu. Phase diagram of spherical particles interacted with harmonic repulsions. *The Journal of Chemical Physics*, 134(4):044903, 2011.

- [77] Giovanni Romeo and Massimo Pica Ciamarra. Elasticity of compressed microgel suspensions. *Soft Matter*, 9(22):5401–5406, 2013.
- [78] Jianzhong Wu, Gang Huang, and Zhibing Hu. Interparticle potential and the phase behavior of temperature-sensitive microgel dispersions. *Macromolecules*, 36(2):440–448, 2003.
- [79] Huaguang Wang, Xuebang Wu, Zhengang Zhu, CS Liu, and Zexin Zhang. Revisit to phase diagram of poly (n-isopropylacrylamide) microgel suspensions by mechanical spectroscopy. *The Journal of chemical physics*, 140(2):024908, 2014.
- [80] Priti S Mohanty, Sofi Nöjd, Kitty van Gruijthuijsen, Jérôme J Crassous, Marc Obiols-Rabasa, Ralf Schweins, Anna Stradner, and Peter Schurtenberger. Interpenetration of polymeric microgels at ultrahigh densities. *Scientific Reports*, 7(1):1–12, 2017.
- [81] I Bouhid De Aguiar, Ties Van de Laar, Martine Meireles, Antoine Bouchoux, Joris Sprakel, and Karin Schroën. Deswelling and deformation of microgels in concentrated packings. *Scientific reports*, 7(1):1–11, 2017.
- [82] Gaurasundar M Conley, Philippe Aebischer, Sofi Nöjd, Peter Schurtenberger, and Frank Scheffold. Jamming and overpacking fuzzy microgels: Deformation, interpenetration, and compression. *Science Advances*, 3(10):e1700969, 2017.
- [83] Gaurasundar M Conley, Chi Zhang, Philippe Aebischer, James L Harden, and Frank Scheffold. Relationship between rheology and structure of interpenetrating, deforming and compressing microgels. *Nature communications*, 10(1):2436, 2019.
- [84] U Gasser, JS Hyatt, J-J Lietor-Santos, ES Herman, L Andrew Lyon, and A Fernandez-Nieves. Form factor of pnipam microgels in overpacked states. *The Journal of chemical physics*, 141(3):034901, 2014.
- [85] Andrea Scotti, Alan R Denton, Monia Brugnoli, Judith E Houston, Ralf Schweins, Igor I Potemkin, and Walter Richtering. Deswelling of microgels in crowded suspensions depends on cross-link density and architecture. *Macromolecules*, 52(11):3995–4007, 2019.
- [86] Frank Scheffold, Pedro Díaz-Leyva, Mathias Reufer, Nasser Ben Braham, Iseult Lynch, and James L Harden. Brushlike interactions between thermoresponsive microgel particles. *Physical review letters*, 104(12):128304, 2010.
- [87] Roy Stanley Burdon. *Surface tension and the spreading of liquids*. Cambridge University Press, 2014.
- [88] Manuel F Ruiz-Lopez, Joseph S Francisco, Marilia TC Martins-Costa, and Josep M Anglada. Molecular reactions at aqueous interfaces. *Nature Reviews Chemistry*, pages 1–17, 2020.

-
- [89] Dieter Bothe and Arnold Reusken. *Transport Processes at Fluidic Interfaces*. Springer, 2017.
- [90] Willem Norde. *Colloids and interfaces in life sciences and bionanotechnology*. CRC Press, 2011.
- [91] Brent S Murray. Microgels at fluid-fluid interfaces for food and drinks. *Advances in Colloid and Interface Science*, 271:101990, 2019.
- [92] Man-hin Kwok, Guanqing Sun, and To Ngai. Microgel particles at interfaces: phenomena, principles, and opportunities in food sciences. *Langmuir*, 35(12):4205–4217, 2019.
- [93] Yves Chevalier and Marie-Alexandrine Bolzinger. Emulsions stabilized with solid nanoparticles: Pickering emulsions. *Colloids and Surfaces A: Physicochemical and Engineering Aspects*, 439:23–34, 2013.
- [94] Robert Aveyard, Bernard P Binks, and John H Clint. Emulsions stabilised solely by colloidal particles. *Advances in Colloid and Interface Science*, 100:503–546, 2003.
- [95] David Julian McClements. Protein-stabilized emulsions. *Current opinion in colloid & interface science*, 9(5):305–313, 2004.
- [96] Jin-Woong Kim, Daeyeon Lee, Ho Cheung Shum, and David A Weitz. Colloid surfactants for emulsion stabilization. *Advanced materials*, 20(17):3239–3243, 2008.
- [97] Marcel Rey, Miguel Angel Fernandez-Rodriguez, Matthias Karg, Lucio Isa, and Nicolas Vogel. Poly-n-isopropylacrylamide nanogels and microgels at fluid interfaces. *Accounts of Chemical Research*, 2020.
- [98] Syuji Fujii, Elizabeth S Read, Bernard P Binks, and Steven P Armes. Stimulus-responsive emulsifiers based on nanocomposite microgel particles. *Advanced Materials*, 17(8):1014–1018, 2005.
- [99] Zifu Li and To Ngai. Microgel particles at the fluid–fluid interfaces. *Nanoscale*, 5(4):1399–1410, 2013.
- [100] Marcel Rey, Miguel Ángel Fernández-Rodríguez, Mathias Steinacher, Laura Scheidegger, Karen Geisel, Walter Richtering, Todd M Squires, and Lucio Isa. Isostructural solid-solid phase transition in monolayers of soft core-shell particles at fluid interfaces: structure and mechanics. *Soft Matter*, 12(15):3545–3557, 2016.
- [101] By Marcel Rey, Roey Elnathan, Ran Ditcovski, Karen Geisel, Michele Zanini, Miguel-Angel Fernandez-Rodriguez, Vikrant V Naik, Andreas Frutiger, Walter Richtering, Tal Ellenbogen, et al. Fully tunable silicon nanowire arrays fabricated by soft nanoparticle templating. *Nano letters*, 16(1):157–163, 2016.

-
- [102] M Friederike Schulte, Andrea Scotti, Arjan PH Gelissen, Walter Richtering, and Ahmed Mourran. Probing the internal heterogeneity of responsive microgels adsorbed to an interface by a sharp sfm tip: Comparing core-shell and hollow microgels. *Langmuir*, 34(14):4150–4158, 2018.
- [103] Zifu Li, Karen Geisel, Walter Richtering, and To Ngai. Poly (n-isopropylacrylamide) microgels at the oil-water interface: adsorption kinetics. *Soft Matter*, 9(41):9939–9946, 2013.
- [104] Sebastian Berger, Haiping Zhang, and Andrij Pich. Microgel-based stimuli-responsive capsules. *Advanced Functional Materials*, 19(4):554–559, 2009.
- [105] Rhutesh K Shah, Jin-Woong Kim, and David A Weitz. Monodisperse stimuli-responsive colloidosomes by self-assembly of microgels in droplets. *Langmuir*, 26(3):1561–1565, 2010.
- [106] Susanne Wiese, Antje C Spiess, and Walter Richtering. Microgel-stabilized smart emulsions for biocatalysis. *Angewandte Chemie*, 125(2):604–607, 2013.
- [107] Eric Dickinson. Microgels-an alternative colloidal ingredient for stabilization of food emulsions. *Trends in Food Science & Technology*, 43(2):178–188, 2015.
- [108] Jongseong Kim, Satish Nayak, and L Andrew Lyon. Bioresponsive hydrogel microlenses. *Journal of the American Chemical Society*, 127(26):9588–9592, 2005.
- [109] Sakiko Tsuji and Haruma Kawaguchi. Colored thin films prepared from hydrogel microspheres. *Langmuir*, 21(18):8439–8442, 2005.
- [110] Tingting Liu, Sebastian Seiffert, Julian Thiele, Adam R Abate, David A Weitz, and Walter Richtering. Non-coalescence of oppositely charged droplets in ph-sensitive emulsions. *Proceedings of the National Academy of Sciences*, 109(2):384–389, 2012.
- [111] Walter Richtering. Responsive emulsions stabilized by stimuli-sensitive microgels: emulsions with special non-pickering properties. *Langmuir*, 28(50):17218–17229, 2012.
- [112] Hadi Mehrabian, Jacco Snoeijer, and Jens Harting. Desorption energy of soft particles from a fluid interface. *Soft Matter*, 2020.
- [113] Karen Geisel, Lucio Isa, and Walter Richtering. Unraveling the 3d localization and deformation of responsive microgels at oil/water interfaces: a step forward in understanding soft emulsion stabilizers. *Langmuir*, 28(45):15770–15776, 2012.
- [114] Mathieu Destribats, Véronique Lapeyre, Mélanie Wolfs, Elisabeth Sellier, Fernando Leal-Calderon, Valérie Ravaine, and Véronique Schmitt. Soft microgels as pickering emulsion stabilisers: role of particle deformability. *Soft Matter*, 7(17):7689–7698, 2011.

- [115] H el ene Monteillet, Marcel Workamp, Jeroen Appel, J Mieke Kleijn, Frans AM Leermakers, and Joris Sprakel. Ultrastrong anchoring yet barrier-free adsorption of composite microgels at liquid interfaces. *Advanced Materials Interfaces*, 1(7):1300121, 2014.
- [116] Mathieu Destribats, V eronique Lapeyre, Elisabeth Sellier, Fernando Leal-Calderon, Val erie Ravaine, and V eronique Schmitt. Origin and control of adhesion between emulsion drops stabilized by thermally sensitive soft colloidal particles. *Langmuir*, 28(8):3744–3755, 2012.
- [117] To Ngai, Sven Holger Behrens, and Helmut Auweter. Novel emulsions stabilized by ph and temperature sensitive microgels. *Chemical communications*, 3:331–333, 2005.
- [118] Bastian Brugger, Brian A Rosen, and Walter Richtering. Microgels as stimuli-responsive stabilizers for emulsions. *Langmuir*, 24(21):12202–12208, 2008.
- [119] Omkar S Deshmukh, Armando Maestro, Michel HG Duits, Dirk van den Ende, Martien Cohen Stuart, and Frieder Mugele. Equation of state and adsorption dynamics of soft microgel particles at an air–water interface. *Soft Matter*, 10(36):7045–7050, 2014.
- [120] Michael C Petty. *Langmuir-Blodgett films: an introduction*. Cambridge University Press, 1996.
- [121] Lucio Isa, Falk Lucas, Roger Wepf, and Erik Reimhult. Measuring single-nanoparticle wetting properties by freeze-fracture shadow-casting cryo-scanning electron microscopy. *Nature communications*, 2(1):1–9, 2011.
- [122] Robert W Style, Lucio Isa, and Eric R Dufresne. Adsorption of soft particles at fluid interfaces. *Soft Matter*, 11(37):7412–7419, 2015.
- [123] Man-hin Kwok and To Ngai. A confocal microscopy study of micron-sized poly (n-isopropylacrylamide) microgel particles at the oil–water interface and anisotropic flattening of highly swollen microgel. *Journal of Colloid and Interface Science*, 461:409–418, 2016.
- [124] Fabrizio Camerin, Nicoletta Gnan, Jos e Ruiz-Franco, Andrea Ninarello, Lorenzo Rovigatti, and Emanuela Zaccarelli. Microgels at interfaces behave as 2d elastic particles featuring reentrant dynamics. *Physical Review X*, 10(3):031012, 2020.
- [125] Karen Geisel, Katja Henzler, Peter Guttman, and Walter Richtering. New insight into microgel-stabilized emulsions using transmission x-ray microscopy: nonuniform deformation and arrangement of microgels at liquid interfaces. *Langmuir*, 31(1):83–89, 2014.
- [126] Fabrizio Camerin, Miguel Angel Fernandez-Rodriguez, Lorenzo Rovigatti, Maria-Nefeli Antonopoulou, Nicoletta Gnan, Andrea Ninarello, Lucio Isa, and Emanuela Zaccarelli. Microgels adsorbed at liquid-liquid interfaces: a joint numerical and experimental study. *ACS nano*, 13:4548–4559, 2019.

- [127] Andrea Scotti, Steffen Bochenek, Monia Brugnoli, Miguel-Angel Fernandez-Rodriguez, Marie F Schulte, JE Houston, Arjan PH Gelissen, Igor I Potemkin, Lucio Isa, and Walter Richtering. Exploring the colloid-to-polymer transition for ultra-low crosslinked microgels from three to two dimensions. *Nature communications*, 10(1):1418, 2019.
- [128] Steffen Bochenek, Andrea Scotti, Wojciech Ogieglo, Miguel Angel Fernandez-Rodriguez, Marie Friederike Schulte, Rustam A Gumerov, Nikita V Bushuev, Igor I Potemkin, Matthias Wessling, Lucio Isa, et al. Effect of the 3d swelling of microgels on their 2d phase behavior at the liquid-liquid interface. *Langmuir*, 35(51):16780–16792, 2019.
- [129] Peter A Kralchevsky and Kuniaki Nagayama. Capillary interactions between particles bound to interfaces, liquid films and biomembranes. *Advances in colloid and interface science*, 85(2-3):145–192, 2000.
- [130] Laura Scheidegger, Miguel Ángel Fernández-Rodríguez, Karen Geisel, Michele Zanini, Roey Elnathan, Walter Richtering, and Lucio Isa. Compression and deposition of microgel monolayers from fluid interfaces: particle size effects on interface microstructure and nanolithography. *Physical Chemistry Chemical Physics*, 19(13):8671–8680, 2017.
- [131] Pawel Pieranski. Two-dimensional interfacial colloidal crystals. *Physical Review Letters*, 45(7):569, 1980.
- [132] Armando Maestro. Tailoring the interfacial assembly of colloidal particles by engineering the mechanical properties of the interface. *Current opinion in colloid & interface science*, 39:232–250, 2019.
- [133] Karen Geisel, Lucio Isa, and Walter Richtering. The compressibility of pH-sensitive microgels at the oil–water interface: Higher charge leads to less repulsion. *Angewandte Chemie International Edition*, 53(19):4905–4909, 2014.
- [134] Christine Picard, Patrick Garrigue, Marie-Charlotte Tatry, Veronique Lapeyre, Serge Ravaine, Veronique Schmitt, and Valerie Ravaine. Organization of microgels at the air–water interface under compression: role of electrostatics and cross-linking density. *Langmuir*, 33(32):7968–7981, 2017.
- [135] Maximilian Marcel Schmidt, Steffen Bochenek, Alexey A Gavrillov, Igor I Potemkin, and Walter Richtering. Influence of charges on the behavior of polyelectrolyte microgels confined to oil-water interfaces. *Langmuir*, 2020.
- [136] Marcel Rey, Adam D Law, D Martin A Buzza, and Nicolas Vogel. Anisotropic self-assembly from isotropic colloidal building blocks. *Journal of the American Chemical Society*, 139(48):17464–17473, 2017.
- [137] Bastian Brugger, Jan Vermant, and Walter Richtering. Interfacial layers of stimuli-responsive poly-(n-isopropylacrylamide-co-methacrylicacid)(pnipam-co-maa) microgels characterized by interfacial rheology and compression isotherms. *Physical Chemistry Chemical Physics*, 12(43):14573–14578, 2010.

- [138] Shilin Huang, Kornelia Gawlitza, Regine von Klitzing, Werner Steffen, and Gunter K Auernhammer. Structure and rheology of microgel monolayers at the water/oil interface. *Macromolecules*, 50(9):3680–3689, 2017.
- [139] Florent Pinaud, Karen Geisel, Pascal Massé, Bogdan Catargi, Lucio Isa, Walter Richtering, Valérie Ravaine, and Véronique Schmitt. Adsorption of microgels at an oil–water interface: correlation between packing and 2d elasticity. *Soft Matter*, 10(36):6963–6974, 2014.
- [140] Simone Ciarella, Marcel Rey, Johannes Harrer, Nicolas Holstein, Maret Ickler, Hartmut Lowen, Nicolas Vogel, and Liesbeth Janssen. Soft particles at liquid interfaces: From molecular particle architecture to collective phase behavior. *arXiv preprint arXiv:2008.13695*, 2020.
- [141] EA Jagla. Phase behavior of a system of particles with core collapse. *Physical Review E*, 58(2):1478, 1998.
- [142] Fabio Grillo, Miguel Angel Fernandez-Rodriguez, Maria-Nefeli Antonopoulou, Dominic Gerber, and Lucio Isa. Self-templating assembly of soft microparticles into complex tessellations. *Nature*, 582(7811):219–224, 2020.
- [143] Nicoletta Gnan, Lorenzo Rovigatti, Maxime Bergman, and Emanuela Zaccarelli. In silico synthesis of microgel particles. *Macromolecules*, 50(21):8777–8786, 2017.
- [144] Letizia Tavagnacco, Emanuela Zaccarelli, and Ester Chiessi. On the molecular origin of the cooperative coil-to-globule transition of poly(n-isopropylacrylamide) in water. *Phys. Chem. Chem. Phys.*, 2018.
- [145] Letizia Tavagnacco, Ester Chiessi, Marco Zanatta, Andrea Orecchini, and Emanuela Zaccarelli. Water–polymer coupling induces a dynamical transition in microgels. *The journal of physical chemistry letters*, 10(4):870–876, 2019.
- [146] Ralf Everaers, Hossein Ali Karimi-Varzaneh, Frank Fleck, Nils Hojdis, and Carsten Svaneborg. Kremer–grest models for commodity polymer melts: Linking theory, experiment, and simulation at the kuhn scale. *Macromolecules*, 53(6):1901–1916, 2020.
- [147] James E Mark et al. *Physical properties of polymers handbook*, volume 1076. Springer, 2007.
- [148] Lorenzo Rovigatti, Nicoletta Gnan, Letizia Tavagnacco, Angel J Moreno, and Emanuela Zaccarelli. Numerical modelling of non-ionic microgels: an overview. *Soft Matter*, 2019.
- [149] Rustam A Gumerov, Artem M Rumyantsev, Andrey A Rudov, Andriy Pich, Walter Richtering, Martin Möller, and Igor I Potemkin. Mixing of two immiscible liquids within the polymer microgel adsorbed at their interface. *ACS Macro Letters*, 5(5):612–616, 2016.

- [150] Monia Brugnoli, Andrea Scotti, Andrey A Rudov, Arjan PH Gelissen, Tobias Caumanns, Aurel Radulescu, Thomas Eckert, Andrij Pich, Igor I Potemkin, and Walter Richtering. Swelling of a responsive network within different constraints in multi-thermosensitive microgels. *Macromolecules*, 51(7):2662–2671, 2018.
- [151] Artem M Rumyantsev, Rustam A Gumerov, and Igor I Potemkin. A polymer microgel at a liquid–liquid interface: theory vs. computer simulations. *Soft Matter*, 12(32):6799–6811, 2016.
- [152] Vladimir Yu Rudyak, Alexey A Gavrilov, Elena Yu Kozhunova, and Alexander V Chertovich. Shell–corona microgels from double interpenetrating networks. *Soft matter*, 14(15):2777–2781, 2018.
- [153] Gaurasundar M Conley, Philippe Aebischer, Sofi Nöjd, Peter Schurtenberger, and Frank Scheffold. Jamming and overpacking fuzzy microgels: Deformation, interpenetration, and compression. *Science Advances*, 3(10):e1700969, 2017.
- [154] S Nikolov, A Fernandez-Nieves, and A Alexeev. Mesoscale modeling of microgel mechanics and kinetics through the swelling transition. *Applied Mathematics and Mechanics*, 39(1):47–62, 2018.
- [155] Vladimir Yu Rudyak, Elena Yu Kozhunova, and Alexander V Chertovich. Towards the realistic computer model of precipitation polymerization microgels. *Scientific reports*, 9(1):1–10, 2019.
- [156] Vladimir Yu Rudyak, Elena Yu Kozhunova, and Alexander V Chertovich. Simulation of interpenetrating networks microgel synthesis. *Soft Matter*, 16(20):4858–4865, 2020.
- [157] Ethan Tumarkin and Eugenia Kumacheva. Microfluidic generation of microgels from synthetic and natural polymers. *Chemical Society Reviews*, 38(8):2161–2168, 2009.
- [158] Sebastian Seiffert and David A Weitz. Controlled fabrication of polymer microgels by polymer-analogous gelation in droplet microfluidics. *Soft Matter*, 6(14):3184–3190, 2010.
- [159] Angel J. Moreno and F. Lo Verso. Computational investigation of microgels: synthesis and effect of the microstructure on the deswelling behavior. *Soft Matter*, 14:7083–7096, 2018.
- [160] Francesco Sciortino and Emanuela Zaccarelli. Reversible gels of patchy particles. *Current Opinion in Solid State and Materials Science*, 15(6):246–253, 2011.
- [161] John D Weeks, David Chandler, and Hans C Andersen. Role of repulsive forces in determining the equilibrium structure of simple liquids. *Journal of Chemical Physics*, 54(12):5237–5247, 1971.

-
- [162] Francesco Sciortino. Three-body potential for simulating bond swaps in molecular dynamics. *The European Physical Journal E*, 40(1):3, 2017.
- [163] Gary S Grest and Kurt Kremer. Molecular dynamics simulation for polymers in the presence of a heat bath. *Physical Review A*, 33(5):3628, 1986.
- [164] Kurt Kremer and Gary S Grest. Dynamics of entangled linear polymer melts: A molecular-dynamics simulation. *Journal of Chemical Physics*, 92(8):5057–5086, 1990.
- [165] Kurt Kremer and Gary S Grest. Molecular dynamics (md) simulations for polymers. *Journal of Physics: Condensed Matter*, 2(S):SA295, 1990.
- [166] Monica Iulia Bulacu. *Molecular dynamics studies of entangled polymer chains*. University Library of Groningen[[Host], 2008.
- [167] Tai-Hsien Wu and Dewei Qi. Advantages of a finite extensible nonlinear elastic potential in lattice boltzmann simulations. *The Hilltop Review*, 7(1):10, 2014.
- [168] Carsten Svaneborg and Ralf Everaers. Characteristic time and length scales in kremer-grest bead-spring polymer melts as a function of chain stiffness. *arXiv preprint arXiv:1808.03503*, 2018.
- [169] Daan Frenkel and Berend Smit. *Understanding molecular simulation: from algorithms to applications*, volume 1. Elsevier, 2001.
- [170] S Nikolov, A Fernandez-Nieves, and A Alexeev. Mesoscale modeling of microgel mechanics and kinetics through the swelling transition. *Applied Mathematics and Mechanics*, 39(1):47–62, 2018.
- [171] Timothy W Sirk, Yelena R Slizoberg, John K Brennan, Martin Lisal, and Jan W Andzelm. An enhanced entangled polymer model for dissipative particle dynamics. *The Journal of chemical physics*, 136(13):134903, 2012.
- [172] Thomas Soddemann, Burkhard Dünweg, and Kurt Kremer. A generic computer model for amphiphilic systems. *The European Physical Journal E*, 6(1):409–419, 2001.
- [173] Stephan Bergmann, Oliver Wrede, Thomas Huser, and Thomas Hellweg. Super-resolution optical microscopy resolves network morphology of smart colloidal microgels. *Physical Chemistry Chemical Physics*, 20(7):5074–5083, 2018.
- [174] Andrea Ninarello, Jérôme J Crassous, Divya Paloli, Fabrizio Camerin, Nicoletta Gnan, Lorenzo Rovigatti, Peter Schurtenberger, and Emanuela Zaccarelli. Modeling microgels with a controlled structure across the volume phase transition. *Macromolecules*, 52(20):7584–7592, 2019.
- [175] Tri T Pham, Ulf D Schiller, J Ravi Prakash, and Burkhard Dünweg. Implicit and explicit solvent models for the simulation of a single polymer chain in solution: Lattice boltzmann versus brownian dynamics. *Journal of Chemical Physics*, 131(16):164114, 2009.

- [176] Justin R Spaeth, Ioannis G Kevrekidis, and Athanassios Z Panagiotopoulos. A comparison of implicit-and explicit-solvent simulations of self-assembly in block copolymer and solute systems. *Journal of Chemical Physics*, 134(16):164902, 2011.
- [177] Jean-Claude Neyt, Aurélie Wender, Véronique Lachet, Aziz Ghoufi, and Patrice Malfreyt. Quantitative predictions of the interfacial tensions of liquid–liquid interfaces through atomistic and coarse grained models. *Journal of Chemical Theory and Computation*, 10(5):1887–1899, 2014.
- [178] Daniel J Arismendi-Arrieta and Angel J Moreno. Deformability and solvent penetration in soft nanoparticles at liquid-liquid interfaces. *arXiv preprint arXiv:1911.06725*, 2019.
- [179] Konrad Schwenke, Lucio Isa, David L Cheung, and Emanuela Del Gado. Conformations and effective interactions of polymer-coated nanoparticles at liquid interfaces. *Langmuir*, 30(42):12578–12586, 2014.
- [180] GA Vliegenthart and Henk NW Lekkerkerker. Predicting the gas–liquid critical point from the second virial coefficient. *The Journal of Chemical Physics*, 112(12):5364–5369, 2000.
- [181] Lorenzo Rovigatti, Barbara Capone, and Christos N Likos. Soft self-assembled nanoparticles with temperature-dependent properties. *Nanoscale*, 8(6):3288–3295, 2016.
- [182] Robert D Groot and Patrick B Warren. Dissipative particle dynamics: Bridging the gap between atomistic and mesoscopic simulation. *Journal of Chemical Physics*, 107(11):4423–4435, 1997.
- [183] Eric E Keaveny, Igor V Pivkin, Martin Maxey, and George Em Karniadakis. A comparative study between dissipative particle dynamics and molecular dynamics for simple-and complex-geometry flows. *J. Chem. Phys.*, 123(10):104107, 2005.
- [184] Pep Espanol and Patrick Warren. Statistical mechanics of dissipative particle dynamics. *EPL (Europhysics Letters)*, 30(4):191, 1995.
- [185] Govardhan Reddy and Arun Yethiraj. Implicit and explicit solvent models for the simulation of dilute polymer solutions. *Macromolecules*, 39(24):8536–8542, 2006.
- [186] Rakwoo Chang and Arun Yethiraj. Solvent effects on the collapse dynamics of polymers. *Journal of Chemical Physics*, 114(17):7688–7699, 2001.
- [187] Tri Thanh Pham, Mohit Bajaj, and J Ravi Prakash. Brownian dynamics simulation of polymer collapse in a poor solvent: influence of implicit hydrodynamic interactions. *Soft Matter*, 4(6):1196–1207, 2008.
- [188] Sebastian Seiffert. Impact of polymer network inhomogeneities on the volume phase transition of thermoresponsive microgels. *Macromolecular Rapid Communications*, 33(13):1135–1142, 2012.

- [189] Axel Habicht, Willi Schmolke, Frank Lange, Kay Saalwächter, and Sebastian Seiffert. The non-effect of polymer-network inhomogeneities in microgel volume phase transitions: Support for the mean-field perspective. *Macromolecular Chemistry and Physics*, 215(11):1116–1133, 2014.
- [190] Sabrina Schmidt, Tingting Liu, Stephan Rütten, Kim-Ho Phan, Martin Möller, and Walter Richtering. Influence of microgel architecture and oil polarity on stabilization of emulsions by stimuli-sensitive core-shell poly (n-isopropylacrylamide-co-methacrylic acid) microgels: Mickering versus pickering behavior? *Langmuir*, 27(16):9801–9806, 2011.
- [191] L Isa, I Buttinoni, Miguel Ángel Fernández-Rodríguez, and Siddarth Ayakulangara Vasudevan. Two-dimensional assemblies of soft repulsive colloids confined at fluid interfaces. *Europhysics Letters*, 119(2):26001, 2017.
- [192] Karen Geisel, Andrey A Rudov, Igor I Potemkin, and Walter Richtering. Hollow and core-shell microgels at oil-water interfaces: spreading of soft particles reduces the compressibility of the monolayer. *Langmuir*, 31(48):13145–13154, 2015.
- [193] Rustam A Gumerov, Sergei A Filippov, Walter Richtering, Andrij Pich, and Igor I Potemkin. Amphiphilic microgels adsorbed at oil-water interfaces as mixers of two immiscible liquids. *Soft matter*, 15(19):3978–3986, 2019.
- [194] Rustam A Gumerov, Andrey A Rudov, Walter Richtering, Martin Moller, and Igor I Potemkin. Amphiphilic arborescent copolymers and microgels: from unimolecular micelles in a selective solvent to the stable monolayers of variable density and nanostructure at a liquid interface. *ACS applied materials & interfaces*, 9(37):31302–31316, 2017.
- [195] Johannes Harrer, Marcel Rey, Simone Ciarella, Hartmut Lowen, Liesbeth MC Janssen, and Nicolas Vogel. Stimuli-responsive behavior of pnipam microgels under interfacial confinement. *Langmuir*, 35(32):10512–10521, 2019.
- [196] Fabrizio Camerin, Nicoletta Gnan, Lorenzo Rovigatti, and Emanuela Zaccarelli. Modelling realistic microgels in an explicit solvent. *Scientific Reports*, 8:14426, 2018.
- [197] Hossein Rezaei and Hamid Modarress. Dissipative particle dynamics (dpd) study of hydrocarbon-water interfacial tension (ift). *Chemical Physics Letters*, 620:114–122, 2015.
- [198] Amitesh Maiti and Simon McGrother. Bead-bead interaction parameters in dissipative particle dynamics: Relation to bead-size, solubility parameter, and surface tension. *The Journal of Chemical Physics*, 120(3):1594–1601, 2004.
- [199] R. D. Groot and K. L. Rabone. Mesoscopic simulation of cell membrane damage, morphology change and rupture by nonionic surfactants. *Biophysics Journal*, 81(2):725–736, 2001.

- [200] Susana Zeppieri, Jhosgre Rodríguez, and AL López de Ramos. Interfacial tension of alkane+ water systems. *Journal of Chemical & Engineering Data*, 46(5):1086–1088, 2001.
- [201] Siddarth A Vasudevan, Astrid Rauh, Martin Kröger, Matthias Karg, and Lucio Isa. Dynamics and wetting behavior of core-shell soft particles at a fluid-fluid interface. *Langmuir*, 34(50):15370–15382, 2018.
- [202] Anders Aufderhorst-Roberts, Daniel Baker, Richard J Foster, Olivier Cayre, Johan Mattsson, and Simon D Connell. Nanoscale mechanics of microgel particles. *Nanoscale*, 10(34):16050–16061, 2018.
- [203] Ahmed Mourran, Yaodong Wu, Rustam A Gumerov, Andrey A Rudov, Igor I Potemkin, Andrij Pich, and Martin Möller. When colloidal particles become polymer coils. *Langmuir*, 32(3):723–730, 2016.
- [204] Karen Geisel, Walter Richtering, and Lucio Isa. Highly ordered 2d microgel arrays: compression versus self-assembly. *Soft Matter*, 10(40):7968–7976, 2014.
- [205] Andrea Ninarello, Jérôme J Crassous, Divya Paloli, Fabrizio Camerin, Nicoletta Gnan, Lorenzo Rovigatti, Peter Schurtenberger, and Emanuela Zaccarelli. Advanced modelling of microgel structure across the volume phase transition. *arXiv preprint arXiv:1901.11495*, 2019.
- [206] Cécile Monteux, Claire Marliere, Pauline Paris, Nadege Pantoustier, Nicolas Sanson, and Patrick Perrin. Poly (n-isopropylacrylamide) microgels at the oil- water interface: Interfacial properties as a function of temperature. *Langmuir*, 26(17):13839–13846, 2010.
- [207] Yongqing Xia, Ying Tang, Han Wu, Jing Zhang, Zongyi Li, Fang Pan, Shengjie Wang, Xiaojuan Wang, Hai Xu, and Jian Ren Lu. Fabrication of patterned thermoresponsive microgel strips on cell-adherent background and their application for cell sheet recovery. *ACS Applied Materials & Interfaces*, 9(2):1255–1262, 2017.
- [208] Jo Sing Julia Tang, Romina Sigrid Bader, Eric SA Goerlitzer, Jan Fedja Wendisch, Gilles Remi Bourret, Marcel Rey, and Nicolas Vogel. Surface patterning with sio2@ pnipam core-shell particles. *ACS Omega*, 3(9):12089–12098, 2018.
- [209] Katja Uhlig, Thomas Wegener, Yvonne Hertle, Johannes Bookhold, Magnus Jaeger, Thomas Hellweg, Andreas Fery, and Claus Duschl. Thermoresponsive microgel coatings as versatile functional compounds for novel cell manipulation tools. *Polymers*, 10(6):656, 2018.
- [210] F Bresme and M Oettel. Nanoparticles at fluid interfaces. *Journal of Physics: Condensed Matter*, 19(41):413101, 2007.
- [211] Lorenzo Rovigatti, Nicoletta Gnan, Andrea Ninarello, and Emanuela Zaccarelli. Connecting elasticity and effective interactions of neutral microgels: The validity of the hertzian model. *Macromolecules*, 52:4895, 2019.

- [212] Nicoletta Gnan and Emanuela Zaccarelli. The microscopic role of deformation in the dynamics of soft colloids. *Nature Physics*, 15:683–688, 2019.
- [213] Ludovic Berthier, Angel J Moreno, and Grzegorz Szamel. Increasing the density melts ultrasoft colloidal glasses. *Physical Review E*, 82(6):060501, 2010.
- [214] Ronald Blaak, Barbara Capone, Christos N Likos, and Lorenzo Rovigatti. Accurate coarse-grained potentials for soft matter systems. *Computational Trends in Solvation and Transport in Liquids-Lecture Notes*, 2015.
- [215] Nicoletta Gnan, Emanuela Zaccarelli, and Francesco Sciortino. Casimir-like forces at the percolation transition. *Nature communications*, 5:3267, 2014.
- [216] Franz Gerl and Annette Zippelius. Coefficient of restitution for elastic disks. *Physical Review E*, 59(2):2361, 1999.
- [217] Hisao Hayakawa and Hiroto Kuninaka. Simulation and theory of the impact of two-dimensional elastic disks. *Chemical Engineering Science*, 57(2):239–252, 2002.
- [218] Federica Lo Verso, Leonid Yelash, Sergei A Egorov, and Kurt Binder. Interactions between polymer brush-coated spherical nanoparticles: The good solvent case. *The Journal of chemical physics*, 135(21):214902, 2011.
- [219] Juan J Cerda, Tomas Sintes, and Raul Toral. Pair interaction between end-grafted polymers onto spherical surfaces: A monte carlo study. *Macromolecules*, 36(4):1407–1413, 2003.
- [220] Marcel Rey, Xunan Hou, Jo Sing Julia Tang, and Nicolas Vogel. Interfacial arrangement and phase transitions of pnipam microgels with different crosslinking densities. *Soft Matter*, 13(46):8717–8727, 2017.
- [221] AS El-Tawargy, D Stock, M Gallei, WA Ramadan, MA Shams El-Din, G Reiter, and R Reiter. Multiple structural transitions in langmuir monolayers of charged soft-shell nanoparticles. *Langmuir*, 34(13):3909–3917, 2018.
- [222] Ankush Aggarwal, Eric R May, Charles L Brooks III, and William S Klug. Nonuniform elastic properties of macromolecules and effect of prestrain on their continuum nature. *Physical Review E*, 93(1):012417, 2016.
- [223] Issam Doghri. *Mechanics of deformable solids: linear, nonlinear, analytical and computational aspects*. Springer Science & Business Media, 2013.
- [224] Leslie RG Treloar. The mechanics of rubber elasticity. *Proceedings of the Royal Society of London. A. Mathematical and Physical Sciences*, 351(1666):301–330, 1976.
- [225] Sylvain Meille and Edward J Garboczi. Linear elastic properties of 2d and 3d models of porous materials made from elongated objects. *Modelling and Simulation in Materials Science and Engineering*, 9(5):371, 2001.

- [226] Marc André Meyers and Krishan Kumar Chawla. *Mechanical behavior of materials*. Cambridge university press, 2008.
- [227] Martin H Sadd. *Elasticity: theory, applications, and numerics*. Academic Press, 2009.
- [228] L Athanasopoulou and P Zihlerl. Phase diagram of elastic spheres. *Soft matter*, 13(7):1463–1471, 2017.
- [229] Jonas Riest, Labrini Athanasopoulou, Sergei A Egorov, Christos N Likos, and Primož Zihlerl. Elasticity of polymeric nanocolloidal particles. *Scientific reports*, 5:15854, 2015.
- [230] Salvatore Torquato. *Random Heterogeneous Materials Microstructure and Macroscopic Properties*. Springer, 2002.
- [231] Tzyy-Shyang Lin, Rui Wang, Jeremiah A Johnson, and Bradley D Olsen. Revisiting the elasticity theory for real gaussian phantom networks. *Macromolecules*, 52(4):1685–1694, 2019.
- [232] A Kloczkowski, Burak Erman, and JE Mark. Effect of non-gaussian chains on fluctuations of junctions in bimodal networks. *Polymer*, 43(8):2569–2574, 2002.
- [233] Stefan Wellert, Yvonne Hertle, Marcel Richter, Martin Medebach, David Magerl, Weinan Wang, Bruno Deme, Aurel Radulescu, Peter Muller-Buschbaum, and Thomas Hellweg. Inner structure of adsorbed ionic microgel particles. *Langmuir*, 30(24):7168–7176, 2014.
- [234] Tetyana Kyrey, Judith Witte, Vitaliy Pipich, Artem Feoktystov, Alexandros Koutsoubas, Egor Vezhlev, Henrich Frielinghaus, Regine von Klitzing, Stefan Wellert, and Olaf Holderer. Influence of the cross-linker content on adsorbed functionalised microgel coatings. *Polymer*, 169:29–35, 2019.
- [235] Miguel Ángel Fernández-Rodríguez, Roey Elnathan, Ran Ditcovski, Fabio Grillo, Gaurasundar Marc Conley, Flavia Timpu, Astrid Rauh, Karen Geisel, Tal Ellenbogen, and Rachel Grange. Tunable 2d binary colloidal alloys for soft nanotemplating. *Nanoscale*, 10(47):22189–22195, 2018.
- [236] Josep C Pàmies, Angelo Cacciuto, and Daan Frenkel. Phase diagram of hertzian spheres. *The Journal of chemical physics*, 131(4):044514, 2009.
- [237] William L Miller and Angelo Cacciuto. Two-dimensional packing of soft particles and the soft generalized thomson problem. *Soft Matter*, 7(16):7552–7559, 2011.
- [238] Yu D Fomin, EA Gaiduk, EN Tsiok, and VN Ryzhov. The phase diagram and melting scenarios of two-dimensional hertzian spheres. *Molecular Physics*, 116(21-22):3258–3270, 2018.
- [239] Matthew Urich and Alan R Denton. Swelling, structure, and phase stability of compressible microgels. *Soft matter*, 12(44):9086–9094, 2016.

- [240] Emanuela Zaccarelli, Giuseppe Foffi, Kenneth A Dawson, SV Buldyrev, Francesco Sciortino, and Piero Tartaglia. Confirmation of anomalous dynamical arrest in attractive colloids: a molecular dynamics study. *Physical Review E*, 66(4):041402, 2002.
- [241] G Foffi, F Sciortino, P Tartaglia, E Zaccarelli, F Lo Verso, L Reatto, KA Dawson, and CN Likos. Structural arrest in dense star-polymer solutions. *Physical review letters*, 90(23):238301, 2003.
- [242] Nicoletta Gnan, Gayatri Das, Matthias Sperl, Francesco Sciortino, and Emanuela Zaccarelli. Multiple glass singularities and isodynamics in a core-softened model for glass-forming systems. *Physical review letters*, 113(25):258302, 2014.
- [243] Federica Lo Verso, José A Pomposo, Juan Colmenero, and Angel J Moreno. Tunable slow dynamics in a new class of soft colloids. *Soft matter*, 12(44):9039–9046, 2016.
- [244] William P Krekelberg, Tanuj Kumar, Jeetain Mittal, Jeffrey R Errington, and Thomas M Truskett. Anomalous structure and dynamics of the gaussian-core fluid. *Physical Review E*, 79(3):031203, 2009.
- [245] Sudipta Gupta, Jörg Stellbrink, Emanuela Zaccarelli, Christos N Likos, Manuel Camargo, Peter Holmqvist, Jürgen Allgaier, Lutz Willner, and Dieter Richter. Validity of the stokes-einstein relation in soft colloids up to the glass transition. *Physical review letters*, 115(12):128302, 2015.
- [246] Andrea Scotti, Monia Brugnoli, Carlos G Lopez, Steffen Bochenek, Jérôme J Crassous, and Walter Richtering. Flow properties reveal the particle-to-polymer transition of ultra-low crosslinked microgels. *Soft Matter*, 16:668–678, 2020.
- [247] Sara M Hashmi and Eric R Dufresne. Mechanical properties of individual microgel particles through the deswelling transition. *Soft Matter*, 5(19):3682–3688, 2009.
- [248] Panayiotis Voudouris, Daniel Florea, Paul van der Schoot, and Hans M Wyss. Micromechanics of temperature sensitive microgels: dip in the poisson ratio near the lcst. *Soft Matter*, 9(29):7158–7166, 2013.
- [249] Fany Di Lorenzo, Johannes Hellwig, Regine von Klitzing, and Sebastian Seiffert. Macroscopic and microscopic elasticity of heterogeneous polymer gels. *ACS Macro Letters*, 4(7):698–703, 2015.
- [250] Alexander V Kabanov and Serguei V Vinogradov. Nanogels as pharmaceutical carriers: finite networks of infinite capabilities. *Angewandte Chemie International Edition*, 48(30):5418–5429, 2009.
- [251] Martin Malmsten, Helena Bysell, and Per Hansson. Biomacromolecules in microgels—opportunities and challenges for drug delivery. *Current Opinion in Colloid & Interface Science*, 15(6):435–444, 2010.

- [252] Christine M Nolan, Leslie T Gelbaum, and L Andrew Lyon. H nmr investigation of thermally triggered insulin release from poly (n-isopropylacrylamide) microgels. *Biomacromolecules*, 7(10):2918–2922, 2006.
- [253] Satyakam Patnaik, Ashwani K Sharma, BS Garg, RP Gandhi, and KC Gupta. Photoregulation of drug release in azo-dextran nanogels. *International journal of pharmaceutics*, 342(1-2):184–193, 2007.
- [254] Walter Richtering, Igor I Potemkin, Andrey A Rudov, Gernot Sellge, and Christian Trautwein. Could multiresponsive hollow shell-shell nanocontainers offer an improved strategy for drug delivery?, 2016.
- [255] Hassan Masoud and Alexander Alexeev. Controlled release of nanoparticles and macromolecules from responsive microgel capsules. *Acs Nano*, 6(1):212–219, 2012.
- [256] OLJ Virtanen, A Mourran, PT Pinard, and W Richtering. Persulfate initiated ultra-low cross-linked poly (n-isopropylacrylamide) microgels possess an unusual inverted cross-linking structure. *Soft matter*, 12(17):3919–3928, 2016.
- [257] Thiago Colla, Priti S Mohanty, Sofi Nojd, Erik Bialik, Aaron Riede, Peter Schurtenberger, and Christos N Likos. Self-assembly of ionic microgels driven by an alternating electric field: Theory, simulations, and experiments. *ACS nano*, 12(5):4321–4337, 2018.
- [258] David Rochette, Benjamin Kent, Axel Habicht, and Sebastian Seiffert. Effect of polymer network inhomogeneity on the volume phase transitions of thermo-and ph-sensitive weakly charged microgels. *Colloid and Polymer Science*, 295(3):507–520, 2017.
- [259] Yan Levin, Alexandre Diehl, A Fernández-Nieves, and Antonio Fernández-Barbero. Thermodynamics of ionic microgels. *Physical Review E*, 65(3):036143, 2002.
- [260] Hideki Kobayashi and Roland G Winkler. Structure of microgels with debye-hückel interactions. *Polymers*, 6(5):1602–1617, 2014.
- [261] Hideki Kobayashi, Rene Halver, Godehard Sutmann, and Roland G Winkler. Polymer conformations in ionic microgels in the presence of salt: Theoretical and mesoscale simulation results. *Polymers*, 9(1):15, 2017.
- [262] Manuel Quesada-Pérez, Jose Ramos, Jacqueline Forcada, and Alberto Martín-Molina. Computer simulations of thermo-sensitive microgels: Quantitative comparison with experimental swelling data. *The Journal of chemical physics*, 136(24):244903, 2012.
- [263] Manuel Quesada-Pérez and Alberto Martín-Molina. Monte carlo simulation of thermo-responsive charged nanogels in salt-free solutions. *Soft Matter*, 9(29):7086–7094, 2013.

- [264] Prateek K Jha, Jos W Zwanikken, Francois A Detcheverry, Juan J De Pablo, and Monica Olvera De La Cruz. Study of volume phase transitions in polymeric nanogels by theoretically informed coarse-grained simulations. *Soft Matter*, 7(13):5965–5975, 2011.
- [265] Giovanni Del Monte, Fabrizio Camerin, Andrea Ninarello, Nicoletta Gnan, Lorenzo Rovigatti, and Emanuela Zaccarelli. Charge affinity and solvent effects in numerical simulations of ionic microgels. *Journal of Physics: Condensed Matter*, 2020.
- [266] Giovanni Del Monte, Andrea Ninarello, Fabrizio Camerin, Lorenzo Rovigatti, Nicoletta Gnan, and Emanuela Zaccarelli. Numerical insights on ionic microgels: structure and swelling behaviour. *Soft matter*, 15(40):8113–8128, 2019.

